Electrical Interfaces for Organic Nanodevices

Henrichsen, Henrik Hartmann

Publication date:
2010

Document Version
Publisher's PDF, also known as Version of record

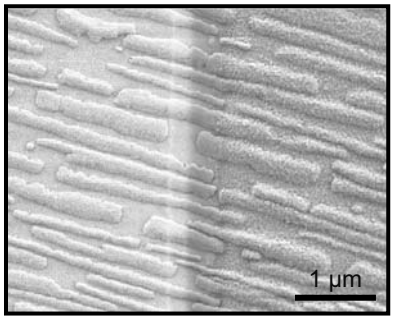

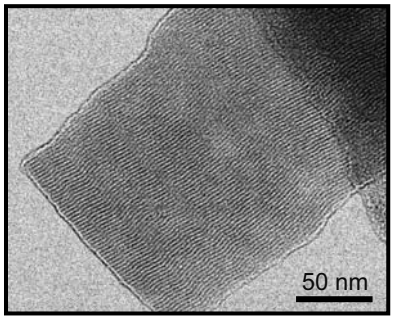

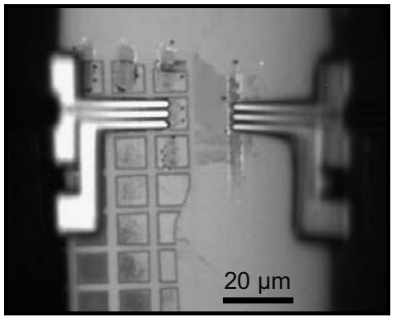

Electrical Interfaces for Organic Nanodevices

Ph.D Thesis

by Henrik Hartmann Henrichsen
May 3rd 2010

Supervisors
Assoc. prof. Peter Bøggild
Prof. Horst-Günter Rubahn

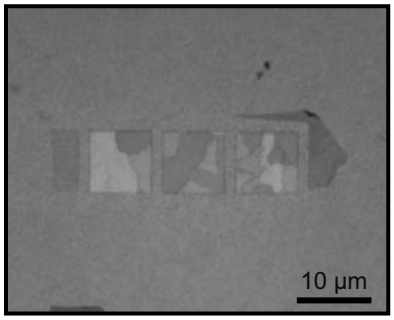

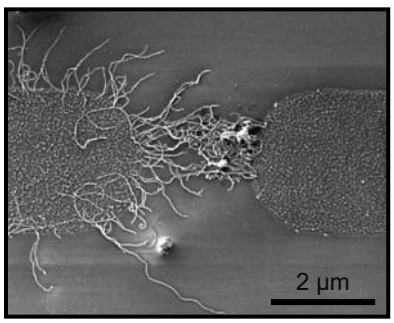

DTU Nanotech
Department of Micro- and Nanotechnology

University of Southern Denmark
NanoSYD

Front cover image captions:

First image: 1 keV SE2 scanning electron microscope image of *para*-hexaphenylene organic nanofibers contacted by gold (left) and samarium (right) metal electrodes. The gap between the electrodes is approximately 0.36 μm.

Second image: 80 keV transmission electron microscope image of a *para*-hexaphenylene organic nanofiber partly free hanging from its support. The periodic lines are a result of the crystalline structure (acquired with help from Timothy John Booth).

Third image: Optical microscope image of measurement probes engaged on a thin graphite electrode (left) and a bi-layer graphene electrode (right). The sample is an array of organic field effect transistors.

Fourth image: Optical microscope image of a multilayer graphene flake patterned by electron-beam lithography after which a 78 nm thin film of *para*-hexaphenylene was deposited. Crystalline domains have formed on the graphene flakes and the inherent polarization of the microscope differentiates the observed color of individual domains.

Fifth image: Thin graphite electrodes, patterned by electron-beam lithography, upon which multi-walled carbon nanotubes have been assembled by dielectrophoresis.

Preface

This thesis has been submitted to partially fulfill the requirements of obtaining the Ph.D. degree from the Technical University of Denmark (DTU). The work has been funded by the Danish Council for Independent Research within Technology and Production Sciences (FTP) through a grant given to my supervisor assoc. prof. Ph.D. Peter Bøggild. The work has mainly been conducted at the Department of Micro- and Nanotechnology, Nanotech, at DTU in Kgs. Lyngby. Part of the work was carried out in the group of co-supervisor prof. Dr. habil. Horst-Günter Rubahn at the Mads Clausen Institute (MCI) University of Southern Denmark (SDU) in Sønderborg. In addition to this thesis, a number of publications have been made during the project, these are listed in app. A.

Before this project was started I had the opportunity to work under the supervision of (now prof.) Dr. rer. nat. Heinz Sturm at the Federal Institute for Materials Research and Testing (BAM) in Berlin. From that employment I gained valuable experience which was used in the experimental work of this project. For that I acknowledge both Heinz Sturm and Horst-Günter Rubahn for making my stay at BAM possible.

During my project I have collaborated with several people in order to acquire expert knowledge and expertise to aid me in my work. First and foremost I acknowledge my supervisor Peter Bøggild for making the Nanointegration group a pleasant working environment for me and my colleagues. His enthusiasm and admirable skills in science and communication have truly been a beacon I strived to follow and will continue to be so. I am grateful for guidance through tough decisions and onto important sidetracks, which has ensured a sensible course through my research.

I acknowledge the supervision given by Horst-Günter Rubahn who has always resolved issues fast and in a very satisfactory manner.

The most important scientific collaborator through my project has undoubtedly been asst. prof. Ph.D. Jakob Kjelstrup-Hansen from the group of Horst-Günter Rubahn. Our friendship and professional collaboration precede this project and we have had invaluable discussions over key subjects. I am also grateful for the opportunity to stay at his home in Sønderborg during my work at SDU.

From DTU Nanotech I greatly acknowledge Ph.D. Timothy John Booth who brought the expertise of graphene technology to the Nanointegration group. He taught me the tricks to graphene fabrication and thereby made it possible for me to explore the novel applications this new material could offer within the topic of my project.

Special thanks go to assoc. prof. Ole Hansen with whom I had the pleasure to collaborate on the analysis of experimental data. His wit in mathematical

modeling of electrical devices has truly been invaluable.

From Horst-Günter Rubahn's group I also greatly acknowledge assoc. prof. Dr. habil. Frank Balzer who has been a great collaborator in the analysis of *p*6P growth on graphitic samples.

From DTU Nanotech I acknowledge asst. prof. Ph.D. Maria Dimaki for her collaboration and for teaching me the practices of dielectrophoresis.

Furthermore the following persons are acknowledged for aiding my work: Ph.D. Torben Mikael Hansen (former DTU Nanotech), M.Eng Xuhai Liu (MCI, SDU), assoc. prof. Ph.D. Kristian Mølhave (DTU Nanotech), Ph.D. Morten Madsen (former MCI, SDU), M.Eng Kasper Thilsing-Hansen (MCI, SDU), docent Ph.D. Jørn Bindslev Hansen (DTU Physics), prof. Ph.D. Andy Horsewell (DTU Mechanical Engineering), the DTU Danchip staff, prof. Dr. rer. nat. Norbert Koch (HU, Berlin) for advices on how to make a working sandwich OLED, prior students M.Eng Tufan Tamer, M.Eng Wojciech Bobrowski and M.Eng Frederik B. Hansen.

For using other peoples equipment I am also grateful to: prof. Ph.D. Anders Kristensen, assoc. prof. Ph.D. Anders Wolff, asst. prof. Ph.D. Detlef Snakenborg and assoc. prof. Ph.D. Bo Wegge Lauersen (University of Copenhagen).

Finally I am grateful to my family for a caring supply of food, cheer and love.

Henrik Hartmann Henrichsen
May 2010
DTU Nanotech
Kgs. Lyngby, Denmark

Abstract

Optoelectronic applications of organic semiconductor materials is a research field, which recently came to the large scale consumer market in display technologies. Organic semiconductors are mainly applied in amorphous form offering fabrication control on a large scale. Crystalline organic semiconductors, where the molecular packing is more crucial, have not yet had a major impact in commercial products. This thesis describes development of new ways to electrically contact organic semiconductors. In particular, crystalline organic *para*-hexaphenylene (*p*6P) nanofibers have been used as a representative component for the organic nanofiber class.

Organic light emitting devices based on nanofibers cannot readily be fabricated by conventional methods developed for thin film devices. A novel design of layered top contacts, separated by an insulating layer, was fabricated using three different approaches. Creating the separator by partly oxidizing an Al cathode anodically is considered the most promising implementation, however further development would be necessary.

During the project a group of collaborators managed to obtain electrically stimulated light emission in organic *p*6P nanofibers, by using an AC-gated organic field-effect transistor (OFET) implementation.

The electrical properties of arrays of *p*6P nanofibers were investigated as-grown and modeled theoretically. The developed model, assuming hopping-like transport of charge carriers, was used to estimate the distance between hopping sites. A distance of 23 ± 5 nm was extracted and found to be in good agreement with transmission electron microscopy (TEM) studies.

Graphene, a one atom thin 2D crystal of carbon, has several properties relevant for electrodes: it is atomically flat, optically transparent, does not oxidize, and has high electrical and thermal conductivity. In this project the use of graphene as an electrode material for organic electronics was investigated. For this purpose a fabrication process compatible with contamination sensitive cleanroom equipment was developed. First the process was applied to fabricate arrays of OFET templates and *p*6P applied as the organic semiconductor. The tested devices exhibited large injection barriers and significant hysteresis of the electrical characteristics. Therefore the device design was found unsuitable to elucidate the possible advantages of graphene electrodes in OFETs.

Secondly the electrode fabrication method was applied to realize electrodes for dielectrophoresis experiments. Robust electrodes with multi-layer graphene contact pads and few-layer graphene electrode edges were made. Carbon nanotubes were assembled with dielectrophoresis between electrodes. Optimization of the dispersion prevented the graphitic electrodes from being washed off, and the same samples could be reused for several experiments.

During the experiments it was discovered that thin films of *p*6P on graphitic substrates can form crystalline domains. Molecular orientations on the samples were probed by fluorescence and white light polarization experiments. It was found that blue reflected light has the same polarization as fluorescence from the samples. This can be used to probe molecular orientations in these samples and completely avoid the bleaching effect of UV-excitation. An investigation of the morphological and molecular orientations within the domains, in relation to the graphitic lattice, showed growth of two different crystalline phases. One of the phases was found comparable to the β-phase typically observed on mica substrates. The morphology of the other phase had formed nanofiber-like aggregates on the substrates with typical dimensions up to 500×20 nm^2. A possible application was demonstrated by growing nano-aggregates of *p*6P on a suspended graphene membrane, which could be used for TEM studies of the as-grown crystalline properties of *p*6P.

Resumé

Opto-elektroniske anvendelser af organiske halvledermaterialer er et forskningsfelt som netop har bevæget sig ind på forbrugermarkedet i form af skærmteknologier. Organiske halvledere anvendes primært i amorf form, som kan kontrolleres i stor-skala produktion. Krystallinske organiske halvledere, hvor det er sværere at styre den molekylære struktur, har endnu ikke haft væsentlig indflydelse på forbrugerprodukter. Denne afhandling beskriver udviklingen af nye metoder til at skabe elektrisk kontakt til organiske halvledere. Specielt er krystallinske organiske nanofibre af *para*-hexaphenylen (*p*6P) benyttet som et repræsentativt komponent for klassen af organiske nanofibre.

Organiske lys-emitterende komponenter baseret på nanofibre kan ikke umiddelbart fabrikeres med konventionelle metoder udviklet til tynd-films komponenter. Et nyt design af lagdelte top-kontakter, der tillader kort afstand mellem to forskellige kontaktmaterialer, blev afprøvet med tre forskellige metoder. Kontakterne holdes adskilt af et isolerende lag. At danne separatoren anodisk, ved delvis oxidering af en Al katode, lod til at være den mest lovende metode, som dog vil kræve en del videreudvikling for at komme til at virke.

I løbet af projektet lykkedes det for en samarbejdsgruppe at opnå elektrisk stimuleret lysudsendelse fra organiske *p*6P nanofibre, ved at benytte et vekselstrøms gate-signal i en organisk felt-effekt transistorstruktur (OFET).

De elektriske egenskaber for arrays af *p*6P nanofibre blev undersøgt på det substrat de blev groet og modelleret teoretisk. Den udviklede model, som antager hoppende ledning af ladningsbærere, blev brugt til at estimere hoppeafstanden. En afstand på 23 ± 5 nm blev udledt og fundet i god overenstemmelse med transmissions-electron mikroskopistudier af krystalstrukturen.

Grafén, et enkelt atom-lag af kulstof, har flere egenskaber som er relevante for elektroder til organiske optoelektroniske komponenter: så tyndt som muligt, gennemsigtigt, oxiderer ikke og har god varme- og elektrisk ledningsevne. I dette projekt blev anvendelsen af grafén som elektrodemateriale undersøgt. Til dette formål blev der udviklet en fabrikationsproces kompatibel med rentrumsudstyr. I første omgang blev den anvendt til at fabrikere arrays af OFET elektrodestrukturer og *p*6P blev benyttet som organisk halvleder. De afprøvede komponenter havde for store barrierer for ladnings-injektion og betydelig hysterese i de elektriske karakteristikker. På den baggrund blev komponent-designet fundet uegnet til at blive anvendt som tiltænkt.

I anden omgang blev processen anvendt til at fabrikere elektroder til brug i dielektrophorese-eksperimenter. Robuste elektroder med mange grafén-lag på kontaktområderne, og kun få grafén-lag ved elektrodekanterne, blev fabrikeret. Kulstof-nanorør blev via dielektroforese samlet mellem elektroder. Optimering af den benyttede opløsning modvirkede at elektroderne faldt af under dielek-

troforeseforsøg, og den samme prøve kunne genbruges i gentagne forsøg.

I forbindelse med forsøgene blev det opdaget at en tynd-film af *p*6P på grafitiske substrater kan danne krystallinske domæner. Molekylernes orientering på prøverne blev målt ved detektion af polariseringen af fluorescens og reflekteret hvidt lys fra prøverne. Målingerne viste at den blå farve af det reflekterede lys havde samme polarisering som fluorescencen. Dette kan benyttes til at måle molekylernes orientering helt uden den blegning som UV-belysning normalt forårsager. En undersøgelse af de morfologiske og molekylære orienteringer i domænerne, holdt op imod den grafitiske krystalstruktur, afslørede to forskellige krystal-faser. Den ene fase mindede om β-fasen, som typisk ses på mica-substrater. Den anden fase havde nanofiber-lignende strukturer på substraterne med typiske dimensioner på op til 500×20 nm^2. En mulig anvendelse af denne opdagelse blev demonstreret ved at gro nanostrukturer af *p*6P på en frithængende grafén-membran. Denne kan bruges til transmissions-elektron mikroskopistudier af *p*6Ps krystallinske egenskaber direkte på det substrat de er groet.

List of symbols

γ	Fourier component in frequency analysis of periodic signals
Γ	Geometric factor for dielectrophoresis on rod-shaped particles[1]
Δ	A small distance corresponding to the Debye length of p6P close to a Sm electrode
ϵ	Permittivity
ϵ_0	Permittivity of free space, 8.854×10^{-12} F/m
ϵ_{ins}	Permittivity of an insulator
ϵ_{m}	Real part of a mediums permittivity
ε	Energy
ε_{C}	Conduction band energy level
ε_{F}	Fermi energy level
ε_i	i'th energy state of a quantum well
ε_{V}	Valence band energy level
θ	Angle
Λ	Abstract characteristic length parameter equal to $\epsilon\nu_0 E_0/J$. Only used used to clarify the mathematical derivation in chapter 3
μ	Charge carrier mobility. This is generally not the same for holes and electrons, why the indexes "e" and "h" sometimes are used to distinguish the two
μ_0	Low electric field charge carrier mobility
ν	Frequency of charge carrier jump attempts
ν_0	Charge carrier drift velocity parameter
$\nu\,(E)$	Electric field dependent drift velocity of charge carriers
ρ_{Al}	Density of Al

Φ_0	Height of potential barrier, unit is volt
Φ_B	A potential barrier the electron must jump over to reach the next domain of a *p*6P nanofiber, unit is volt
$\Phi_\mathrm{Bn,A}$	Barrier for electrons to jump into the LUMO band of *p*6P from an Au electrode, unit is volt
ϕ_wf	Work function
ω	Angular frequency
a	The distance between energy barriers in a one-dimensional periodic potential, see pp. 22
A	Cross sectional area of a conducting channel
A_elec	Electrode area
C	Capacitance
C_ins	Parallel plate capacitance of an un-grounded DEP electrode towards the backgate
$\vec{d}$	Dipole vector
e	Elementary charge, 1.602×10^{-19} C
E	Electric field strength
E_0	Characteristic electric field strength parameter
$\vec{E}$	Electric field vector
F	Flux, defined by an amount passing through a unit area in unit time
F_{O_2}	Flux of oxygen molecules
$\vec{F}_\mathrm{DEP}$	Dielectrophoresis force vector
$\vec{F}_\mathrm{DEP,AC}$	Time averaged dielectrophoresis force vector
$\hbar$	Reduced Planck constant, $h/2\pi = 1.055 \times 10^{-34}$Js
i	Index number
I_disp	Displacement current
I_s	Source current
k_B	Boltzmanns constant, 1.381×10^{-23} J/K
K_f	Relation of complex permittivities of rod-shaped particles and its dispersing medium[1] (equivalent to the complex Clausius-Mossotti function for spheres)
l_{1-3}	Intermediate lengths used to clarify calculation

l_{apt}	Evaporation source aperture size
l_{blur}	Size of electrode edge blur due to the finite size of an evaporation source
l_{mfp}	Mean free path of a gas molecule moving freely through a gas
l_{r}	Shadow mask radius
l_{sm}	Sample to mask distance
l_{ss}	Sample to source distance
L	Device length
m_{Al}	Atomic mass of Al
m_{e}	The electron rest mass, 9.109×10^{-31} kg
m_{n}	Mass of the neutron
$m_{\mathrm{O_2}}$	Molecular mass of O_2
n	Charge carrier concentration
p	Pressure
$p_{\mathrm{O_2}}$	Partial pressure of oxygen
$\vec{p}$	Dipole moment vector
Q	Coulomb charge
$r_{\mathrm{O_2}}$	Radius of the O_2 molecule
R_{max}	Maximum deposition rate
T	Absolute temperature
u	Substituted integration variable
V_{a}	Applied voltage
V_{d}	Drain voltage (relative to the source electrode)
V_{g}	Gate voltage (relative to the source electrode)
$V_{\mathrm{gap,CNT}}$	Voltage between two electrodes connected by a CNT, in a DEP experiment
$V_{\mathrm{gap,open}}$	Voltage between two electrodes in a DEP experiment
V_{gd}	Gate voltage relative to the drain potential
V_{s}	Source voltage
W	Device channel width (conventionally perpendicular to the direction of current in the channel)

Z_{CNT}	Impedance of a CNT and its contacts to DEP electrodes during experiment
Z_{gap}	Impedance of an open gap between DEP electrodes during experiment
Z_{ins}	Impedance of an un-grounded DEP electrode's capacitive coupling to the backgate substrate during experiment

Abbreviations

AC	Alternating current
AFM	Atomic force microscope (or microscopy)
BAM	Federal Institute for Materials Research and Testing
CVD	Chemical vapor deposition
CNT	Carbon nanotube
DAQ	Data acquisition card
DC	Direct current
DEP	Dielectrophoresis
E-beam	Electron-beam
EDX	Energy dispersive X-ray spectroscopy
EMCCD	Electron-multiplying charge-coupled device. A special digital camera chip on which the charge from each pixel is multiplied on the chip before readout, thus minimizing the readout noise.
F8BT	Poly(9,9-dioctylfluorene-alt-benzothiadiazole)
FFT	Fast Fourier transform
HMDS	Hexamethyldisilazane $[(CH_3)_3Si]_2NH$ (used to improve photo resist adhesion)
HOMO	Highest occupied molecular orbital
HOPG	Highly oriented pyrolytic graphite
ITO	Tin doped Indium oxide, typically 90% In_2O_3 and 10% SnO_2. One of the most widely used transparent conductor in commercial applications
LEED	Low energy electron diffraction
LED	Light emitting diode
LUMO	Lowest unoccupied molecular orbital

MCI	Mads Clausen Institute (at SDU)
MWCNT	Multi-walled carbon nanotube
OFET	Organic field-effect transistor
OLED	Organic light emitting diode (the broader term "device" is often used instead of diode)
PCB	Printed circuit board
PMMA	Poly(methyl methacrylate), $(C_5O_2H_8)_n$. Also known as "acrylic" or commercially as PLEXIGLAS
PVD	Physical vapor deposition
RIE	Reactive ion etching
SDU	University of Southern Denmark
SE1	Secondary electrons "1" = electrons knocked out of the sample by the incoming primary electrons, mainly emitted close to the beam entry
SE2	Secondary electrons "2" = electrons knocked out of the sample by backscattered primary electrons
SEM	Scanning electron microscope (or microscopy)
STM	Scanning tunneling microscope (or microscopy)
TEM	Transmission electron microscope (or microscopy)
*p*6P	*Para*-hexaphenylene, also known as *para*-sexiphenylene. In literature also abbreviated 6P.
TMAH	Tetramethylammonium hydroxide, $(CH_3)_4NOH$
UPS	Ultraviolet photoelectron spectroscopy

Contents

Chapter 1

Introduction

Allow me to share some reflections of our society's relation to science with you. Since humans started to use tools in everyday life, technology has played a crucial role in the evolution of mankind. To begin with, development was primarily aimed at improving the chances of survival whether it being hunting or farming tools, better clothing, or weapons to defeat enemies. Civilization evolved and with that technological development started to accelerate, central rulership could allocate resources to focus on certain areas considered important by the people in power. All along there has been a curiosity among people seeking explanations to the phenomena of the nature around us. Through history religions have had great success in accommodating the need of answers. But as society evolved people started to describe nature through their own optics. Thus Galileo Galilei (1564-1642) marked a paradigm shift towards the modern science we have today. Some sciences, such as astronomy, were mainly conducted by observing and describing the universe around us, while others worked specifically to improve certain technologies. Both branches have been most fruitful to society; technological advances have improved our everyday quality of life, while astronomy improved the crucial navigation by sea and had a major impact on how we perceive the world.

By the advent of the industrial revolution in the 18^{th} century society changed again, fueled by a widespread implementation of the steam engine. Advances in science and technology significantly accelerated, only this time we turned to a track of unsustainable use of our planets resources. The consequence is that science and technology have become necessary parts of society. There is a need of producing new solutions to ultimately bring our society back on the track of sustainable development.

Society, being the main sponsor of independent research, is now more than ever questioning the use of our limited resources. At first glance allocating all resources to strategic research may seem to be the obvious choice. However, research with a very fixed focus does not necessarily lead to the best results in the long term. Therefore some research projects are granted based on desirable aims, while the researcher is given the opportunity to follow more promising routes within the topic, encountered during the work. This thesis work has been one such project.

The initial aim of the project was to develop organic light emitting diodes (OLEDs) based on a certain class of crystalline organic nanofibers. During the

project, expertise in graphene technology was introduced to the group. This opened the opportunity to investigate the novel and promising aspects of using graphene as an electrode material for organic devices as well as substrate for growing crystalline organic nanofibers.

Most often there are several viable ways of working towards the aims of a project. To get the best results I chose to work by an experimental approach because this is where I perform the best. This is reflected in the work where experimental methods have been developed to reach the goal or evaluate promising applications.

1.1 Light emitting diodes

There are many different ways to generate photons with wavelengths in the part of the electromagnetic spectrum we perceive as light, i.e. $390 \leq \lambda \leq 720$ nm[2]. Some of the first electrical light bulbs developed by Thomas Edison around 1880 relied on black body radiation from a heated filament and started a revolution of artificial lighting. Modern society has a high need of more efficient ways of producing light. Thus fluorescent lamps, generating light by phosphors excited with UV-light from a plasma, is being widely used due to its much higher efficiency and longer lifetime. Light generation by electroluminescence was first reported in 1907 by Henry J. Round[3] and in 1962 the first practical light emitting diode (LED) was invented by Nick Holonyak, Jr.[4]. The technology has since been introduced in more and more commercial products, the first applications being indicator lamps. Their high efficiency as monochromatic emitters and in particular long lifetime has been the main driver for implementation in signs such as traffic lights. In recent years white light LEDs have been developed to a state where they compete with conventional sources of general lighting[1]. Electroluminescence is a direct conversion from electrical to electromagnetic energy. When electrons conducted through a material can relax into vacant energy states, "holes", radiative recombination gives rise to the emission of photons, i.e. electroluminescence. Various implementations of this is further discussed in chap. 2.

1.1.1 Organic light emitting diodes

The first electroluminescence of an organic semiconductor was observed in a single crystal of anthracene[5] in 1962. When Tang and Van Slyke[6] reported of their thin film based OLED in 1987, research in the field started to accelerate. The main driver of the research up till today has been the great practical advantages of thin film deposition techniques first applied by Tang and Van Slyke. The scalability of this technique is one of the main advantages due to the perspectives of making cheap devices. Frontier research in the field recently demonstrated white light OLEDs with efficiencies comparable to that of fluorescent tubes[7]. One of the most promising commercial application of OLEDs are considered to be within large area general lighting, where good color rendering and energy efficiency is desired. Another application already commercialized is the use in small to medium size displays mainly due to a thin profile and vivid colors[8]. In OLED displays the light is generated in each

[1] See e.g. http://www.osram.com/osram_com/LED/index.html.

pixel contrary to LCD-technologies, where each pixel filters a white backlight to control color. From this principle more energy efficient operation should be expected from the OLED displays.

Crystalline organic semiconductors has gained scientific interest due to some of the special properties compared to the amorphous materials. A high crystallinity typically gives higher charge carrier mobility and thereby better electrical conduction, which is important to obtain high efficiency. Some of the first crystalline OLEDs reported had an efficiency of up to 8%[9], which the amorphous OLEDs later surpassed by the implementation of phosphorous light emitters[10] and doping[11]. If high current density is required, e.g. for electrically driven organic lasers, crystalline materials can be advantageous[12].

Compared to the research in amorphous organic semiconductors the field of crystalline materials is not as evolved. One of the main reasons is the significant challenge of growing well-defined crystals in a controlled way so they can be implemented on a larger scale. Therefore a lot of attention within the community is given to the growth mechanisms of molecular crystals and their physical properties. One way of obtaining molecular crystals on a large scale is to grow nanofiber structures on suitable growth substrates, as discussed in sec. 1.2. However, these are not simply sandwiched between two electrodes to establish electrical contact. This challenge is one of the topics of this thesis.

1.1.2 Organic field-effect transistors

Organic semiconductors can be used to fabricate organic field-effect transistors (OFETs), similar to the inorganic counterparts. These have gained large interest, in part due to the perspectives of printing simple electronic circuits at low cost. This may even be done on flexible substrates which can enable new types of product designs. The most common use of transistors is to build logic circuits to execute software applications. However, OFETs can also be designed as a light emitting device. This powerful feature combined with OFETs to control the device is one of the intriguing perspectives driving the research. The principles of light emitting transistors are discussed in chap. 2.

1.2 Organic *para*-hexaphenylene nanofibers

Research in inorganic nanowires have led to several device applications as well as contributing to material science[13]. Organic nanofibers are yet primarily a subject of materials research, not yet at a state of commercial focus. One of the unsolved issues in the field is an efficient way of fabricating nanofiber OLEDs, an issue this project addresses. Both amorphous[14] and crystalline[15] nanofibers have been reported. This project will focus on crystalline organic nanofibers assembled by *para*-hexaphenylene (*p*6P) molecules[15] as a model aggregate. By functionalizing the constituent molecules the nanofiber properties can be tuned for specific purposes[16]. Figure 1.1 shows optical fluorescence microscope images of *p*6P nanofibers. Dimensions largely depend on growth conditions and typical ranges are from a few tenths of μm to mm in length, up to tenths of nm in height and up to a few hundred nm in width. Crystalline domain size is very dependent on growth conditions and can change from few tenths up to hundreds of nanometers along the long nanofiber axis[18, 19].

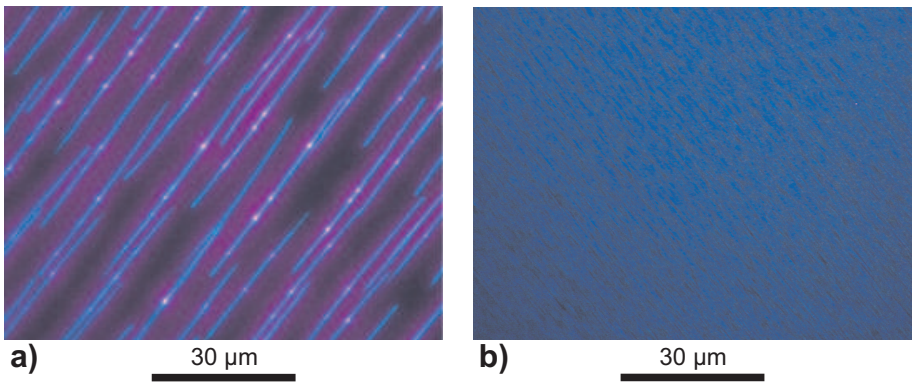

Figure 1.1: Fluorescence optical microscope images of *p*6P nanofibers grown on muscovite mica. a) Separate nanofibers grown by a nominal *p*6P thickness of 3 nm (adapted from [17]). b) Densely packed nanofibers grown by a nominal thickness of 10 nm *p*6P, similar to the samples used in this project.

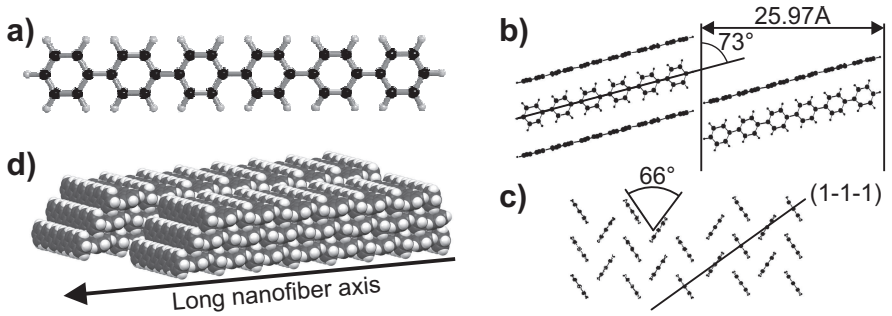

Figure 1.2: Illustrations of *p*6P. a) Ball-and-stick representation of the planar *p*6P molecule, the form obtained in a crystal structure. b)+c) The β-phase crystal of *p*6P. It is a monoclinic lattice of the space group $P2_1/a$ with the lattice constants a = 8.091 Å, b = 5.565 Å, c = 26.264 Å and $\beta = 98.17°$[22], (adapted from [22]). d) Space-filling representation of a part of a *p*6P nanofiber with the long nanofiber axis indicated. The *p*6P crystal faces the substrate with its (1-1-1) plane. The lattice in b) is the view from above the nanofiber, while c) corresponds to looking from the side at an angle.

The *p*6P molecule ($C_{36}H_{26}$) is an oligomer consisting of six phenyl groups placed in a row, as shown in fig. 1.2a. In the gaseous phase the phenyl groups twist due to prevailing hydrogen repulsion. In the crystalline solid state a planar geometry is energetically more favourable[20].

The molecules can arrange into different crystal phases[19], where substrate surface, surface preparation and temperature are among the important growth parameters. The growth of long parallel *p*6P nanofibers on muscovite mica is one of the most well documented systems[21, 17]. *Para*-hexaphenylene nanofibers grown on freshly cleaved (0001) mica surfaces arrange in a so-called herringbone structure, where all long molecular axes are parallel, see fig. 1.2. The mutual orientation of the molecules gives rise to a very pronounced po-

larization of the fluorescence[17], which is a useful feature for investigating the crystallinity of a sample.

The electrical properties of crystalline *p*6P have been investigated both experimentally[23, 24] and theoretically[25]. The conductivity is found to be highly anisotropic, with a preferred conduction perpendicular to the long molecular axes. This is attributed to the higher overlap of molecular orbitals to neighboring molecules in this direction[25].

1.3 Graphene

The introduction of graphene production brought to DTU by Timothy John Booth in 2008 made it possible to explore some of the interesting perspectives of this material as electrodes. This one-atomic-thin sheet of carbon atoms was first reported in isolated form in 2004 by Novoselov et al.[26] and launched a surge of research within the field. The first studies mainly focused on the remarkable material properties such as high electron mobility[27] (in the order of 200000 cm^2/Vs) and quantum effects at room temperature[28]. In the research of applications graphene has recently been applied as electrode material in solar cells[29], OFETs[30] and OLEDs[31].

Despite being only one atomic layer thick, graphene has an absorption of 2.3% of white light[32]. This makes it possible to observe the material in an optical microscope, which is of great advantage in the experimental work. The contrast of graphene can furthermore be increased by dispersing it on thin films, such as SiO_2 or PMMA (a common resist)[33]. Adding more layers increases absorption accordingly, however, few-layer graphene it still considered a promising transparent electrode material as a substitute of the common indium-tin-oxide (ITO) used in most flat panel displays today. The main attractive features are the good transparency, conductivity and perspectives of large scale applicability[34, 35]. Another interesting perspective of graphene electrodes is its applicability to be used on flexible substrates[35]. The sharp edges of graphene makes it suitable as a field emitter and large enhancement factors have been reported[36].

The four most common ways of producing graphene are exfoliation by micro-mechanical cleavage of natural[37] or synthetic[38] graphite, exfoliation by oxidation of graphite and subsequent reduction[34], or growth by chemical vapor deposition (CVD)[35]. Nano-ribbons of graphene have alternatively been produced by chemical derivation from carbon nanotubes (CNTs)[39]. Currently exfoliated natural graphite is considered to produce graphene of the highest crystalline quality, however, graphene produced by CVD techniques are also of high interest because cm large flakes can be grown[40].

Due to the strong sp2 chemical bonding of the graphene lattice, it is considered the strongest material ever measured[41]. Graphene flakes suspended over µm sized windows are readily made and is a very suitable test-bed for materials research[42, 43].

The chemical properties of graphene are also remarkable. Relatively high chemical inertness makes it compatible with most chemicals applied in microfabrication and it does not oxidize at ambient conditions. In electrochemical and biocatalytic processes metal electrodes are often modified by organic thin

films, to control the formation of specific radicals[44]. Graphene electrodes may be useful in such systems, as an alternative to the metal electrodes.

In this project only graphene and graphite flakes made by exfoliation of natural graphite have been used. The process is described in app. F. The process generates flakes in various thicknesses, where single-, double- and triple-layered ones are of main interest. These are commonly referred to as graphene, whereas thicker layers are referred to as thin graphite. "Graphitic" is a term used to describe both classes of flakes.

1.3.1 Dielectrophoresis

Particles suspended in a medium can be affected by electric forces in different ways. If the particle has a net charge, an electric field can exert forces on the particle, and is known as electrophoresis. If the particle is not charged, however, a dipole must be induced by polarizing the particle, before the electric field can exert forces. A homogenous electric field will not exert any net force on the particle since the forces on the positive and negative charges will cancel each other. If the polarizable particle is placed in an inhomogeneous electric field the forces will no longer cancel each other and a net force can result. This is known as dielectrophoresis (DEP)[45]. If the induced dipole vector, $\vec{d}$, is small compared to the non-uniformity of the electric field (dipole approximation), the DEP force in a DC-field, $\vec{F}_{\mathrm{DEP}}$, can be described by eq. (1.1).

$$\vec{F}_{\mathrm{DEP}} = (\vec{p}\,\nabla)\vec{E} \tag{1.1}$$

The dipole moment vector is given by $\vec{p} = Q\vec{d}$, where Q is the separated charges, and $\vec{E}$ is the electrical field vector. As evident the force becomes zero in a homogeneous electric field. If the particle is suspended in a polarizable medium the particle will move towards higher electric field only if it is more polarizable than the medium (positive DEP). Oppositely $\vec{F}_{\mathrm{DEP}}$ will be negative if the medium is the most polarizable (see [45, pp. 10]). Thus DEP forces can be used to separate particles of different polarizabilities.

If an AC-field is applied the dipole will change direction in each cycle, but so does the electric field vector, and the force will act in the same direction for both half-cycles. However, the resulting DEP force must be described with a time-averaged expression[45].

Elongated particles, such as CNTs, can also be assembled by DEP, as shown in fig. 1.3. This is described in a theoretical study by Dimaki and Bøggild[1], where the time averaged expression of AC-field DEP[45] is applied to rod-shaped aggregates:

$$\vec{F}_{\mathrm{DEP,AC}} = \Gamma\epsilon_{\mathrm{m}}\mathrm{Re}\{K_{\mathrm{f}}\}\nabla \mid \vec{E} \mid^2 \tag{1.2}$$

The Γ factor is geometry dependent and proportional to the square of the rod radius and its length. ϵ_{m} is the real part of the dispersing mediums' permittivity and K_{f} depends on the complex permittivities of the rod and the dispersing medium, which generally are frequency dependent (see [1] for details).

Aside from the special application of assembling CNTs on electrodes[46], DEP has also been used for other purposes, such as assembly of proteins[47] or cell handling[48].

The use of graphene as an electrode material for DEP has to the best of my knowledge not previously been reported. In this project a feasibility study is

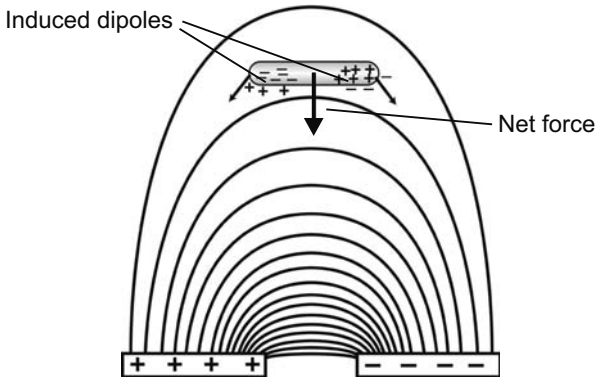

Figure 1.3: Conceptual illustration of dielectrophoretic forces acting on a rod-like particle such as a CNT. The net force is indicated for positive dielectrophoresis attracting the particle towards the electrodes at the bottom. Adapted from [1].

made, to elucidate the applicability of graphene as electrodes for DEP. Some of the anticipated advantages are the high electric field enhancement at the edges, exerting strong forces to attract and fix local particles. Electrode gaps below 10 nm can be much better defined by graphene compared to metal, thus pushing the limit of how small molecules can be investigated (not necessarily assembled by DEP). The sub-nanometer thin profile of the electrode offer virtually no perturbation of the particle assembled - even for single walled CNTs with radiuses down to few nanometers. The assembly of CNTs on graphene electrodes furthermore constitutes a metal-free system, which may be a desirable feature e.g. in electrochemical applications.

1.4 Thesis outline and aims

The general topic of this thesis is the investigation of new ways to establish electrical contact to nanodevices. In the first part, a certain class of nano components, represented by organic nanofibers, was contacted with the ultimate aim of creating nanoscopic OLEDs. This was treated by two different approaches; in chap. 3 asymmetric top electrodes were applied and in chap. 4 new ways to make layered top electrodes were investigated. While electroluminescence was not successfully achieved, the experiments elucidate the issues involved with the different fabrication methods (chap. 4). Furthermore, in chap. 3, the electrical properties of *p*6P nanofibers was investigated by theoretical modeling of measurements. This was used to probe the crystalline properties of the organic *p*6P nanofiber components.

In the second part of the project the feasibility of graphene as an electrode material was investigated and described in chap. 5. A process to shape graphene into desired electrode structures was developed with OFETs as the first test case. During these studies the growth of crystalline domains of *p*6P on graphitic substrates was observed and subsequently investigated. As a second test case the use of graphene as electrodes for DEP was described.

The key principles of electroluminescence and OFET operation applied in the project are introduced in chap. 2.

Chapter 2

Principles of organic light emitting devices

The modern designs of OLEDs share some of the principles developed for inorganic LEDs. To illustrate this, the most basic implementations of inorganic semiconductor p-n-junction LEDs are shown in fig. 2.1. The semiconductor on the left and right sides of the junctions are p- and n-doped respectively. This moves the fermi level close to the valence and conduction bands, thus making the majority charge carriers holes and electrons, respectively. When the devices are forward biased, hole charge carriers are injected from the left and electrons from the right. In the junction zones electrons can relax into the vacant hole states by the emission of electroluminescence. The majority of modern LEDs are implementations of the double heterostructure principle shown in fig. 2.1b[2]. A narrow region of a lower band-gap creates barriers to confine the zone of recombination. The higher concentration of charge carriers and the reduced risk of charges reaching the opposing electrode greatly increases device efficiency[2].

Examples of possible energy schemes in OLEDs are illustrated in fig. 2.2. In the most simple design, fig. 2.2a, the organic semiconductor is sandwiched between an anode and cathode with work functions suitable for injecting holes

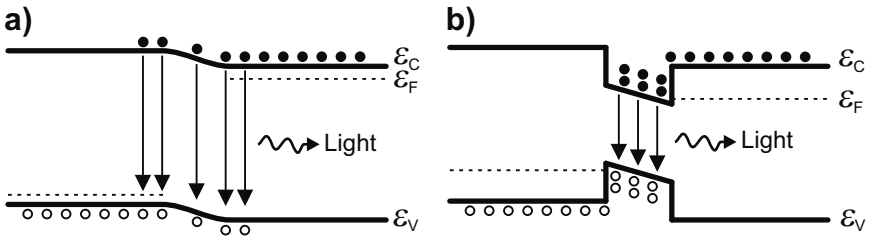

Figure 2.1: Conceptual energy schemes of standard p-n-junction light emitting diodes. ε_C, ε_F and ε_V are the conduction, Fermi and valence band energies, respectively. a) The most simple implementation where the size of the recombination zone is affected by charge carrier diffusion. b) A double hetero junction implementation where charge carriers are confined to recombine in a small region. Adapted from [2, pp. 70].

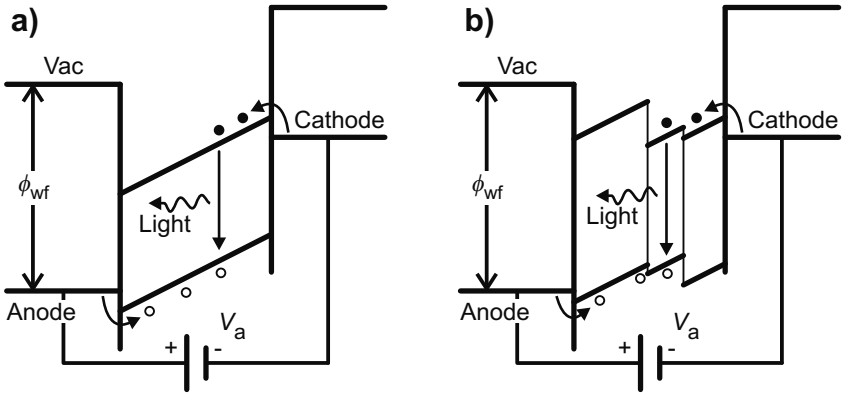

Figure 2.2: Conceptual energy schemes of OLED designs under forward biases. a) A simple single layer OLED design. b) An advanced multi-layer OLED design. Adapted from [9, pp. 921].

and electrons, respectively. The applied electric field drives holes at the energy level of the highest occupied molecular orbital (HOMO) while electrons are transported at the level of the lowest unoccupied molecular orbital (LUMO). When opposite charges meet they form an exciton which is localized on individual molecules. Due to singlet-triplet nature of the molecules' quantum states 25% of the excitons annihilate radiatively, while 75% give up their energy by heat. While this principle works, there are certain disadvantages in addition to the singlet-triplet issue. The relatively high resistance of intrinsic organic semiconductors leads to heating energy losses and the injection barriers are often significant. Both factors leads to high operating voltage which is impractical for many applications and low energy efficiency is undesirable. Moreover, if one charge carrier type is injected and/or conducted better than the other, unbalanced conduction occurs. This causes the recombination zone to be at one of the electrodes leading to non-radiatively quenching of excitons further reducing the efficiency.

More advanced principles have been developed, such as the multilayered device shown in fig. 2.2b, and comprehensively described by Pfeiffer and coworkers[11]. Additional layers have been introduced to improve the operation by different means. At the cathode is an un-doped emission layer. This is kept thin to reduce the ohmic loss. At the anode a doped low-resistance hole transport layer ensures easy injection of holes, which are transported to the electron blocking layer. Charge recombination by holes jumping in to form excitons in the emission layer gives rise to the electroluminescence. The design in fig. 2.2 obtains high efficiency by lowering the overall resistance and ensuring that charge carriers are not allowed to propagate and quench at the electrode interfaces.

The singlet-triplet issue applies to both designs, but this can be addressed by the introduction of phosphorescent dyes to the organic semiconductors. This greatly improves the internal quantum efficiency by making use of the triplet states[9]. Recently efficient doping of crystalline organic crystals have been demonstrated[12], which is a promising advancement of the crystalline class of

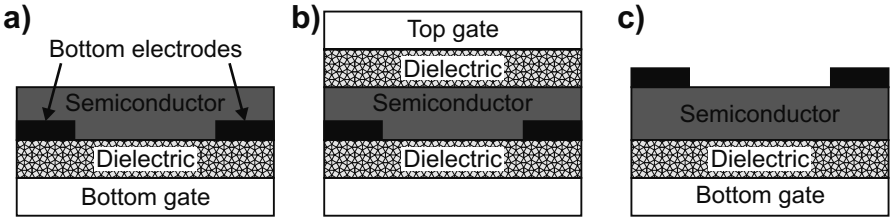

Figure 2.3: Cross-sectional illustrations of typical OFET designs. a) Bottom gate and bottom contacts. b) Top gate and bottom contacts. c) Bottom gate and top contacts. Having the semiconductor in between the electrodes and the gate significantly reduces contact resistance[49]. Adapted from [49].

organic semiconductors.

In chap. 4 approaches to fabricate nanofiber *p*6P OLEDs are discussed. They start with the simple design outlined in fig. 2.2a with the perspectives of being improved towards the design of fig. 2.2b.

2.1 Light emitting OFETs

Similar to inorganic semiconductors, organic semiconductors can be used to make field- effect transistors. There are several different classical designs of implementing FET structures, but for practical reasons the most common OFET designs are limited to planar structures, such as those illustrated in fig. 2.3. The working principle is to create a conducting channel at the semiconductor interface to the gate dielectric. This is accomplished by applying a gate voltage; when a positive potential is applied to the gate electrode, negative charges will accumulate at the interface of the semiconductor supplied by the source and drain electrodes[49][1]. Likewise a negative gate potential accumulates positive charges in the channel. In contrast to inorganic semiconductors, which are doped to either n- or p-type, organic semiconductors are typically used as intrinsic semiconductors in OFETs[49]. Therefore OFETs are said to be enhancement types, i.e. conduction is enhanced by increasing the gate potential. In the energy scheme the operation can be understood as follows: the potential of source and drain electrodes are fixed by the power supply, while the HOMO and LUMO energy levels of the semiconductor can be affected by the gate. Applying a positive gate potential "pulls" the energy level downwards and thereby makes the semiconductor energetically attractive to electrons. Oppositely a negative gate potential "pushes" the energy levels upwards, as shown in fig. 2.4. When the energy levels come close to that of the electrodes, charges starts to inject. Further increasing the gate potential only moves the energy levels very little, while more charges are injected.

OFET operation is highly influenced by the energy level lineup with the electrodes. If the contact energy levels are closer to the HOMO level of the semiconductor, p-channel operation is more readily obtained (assuming hole- and electron conductivities are comparable). If the contact barriers are not too

[1]Note that this is different from an inorganic enhancement mode FET, where the channel is formed by attracting charge carriers from the semiconductor body.

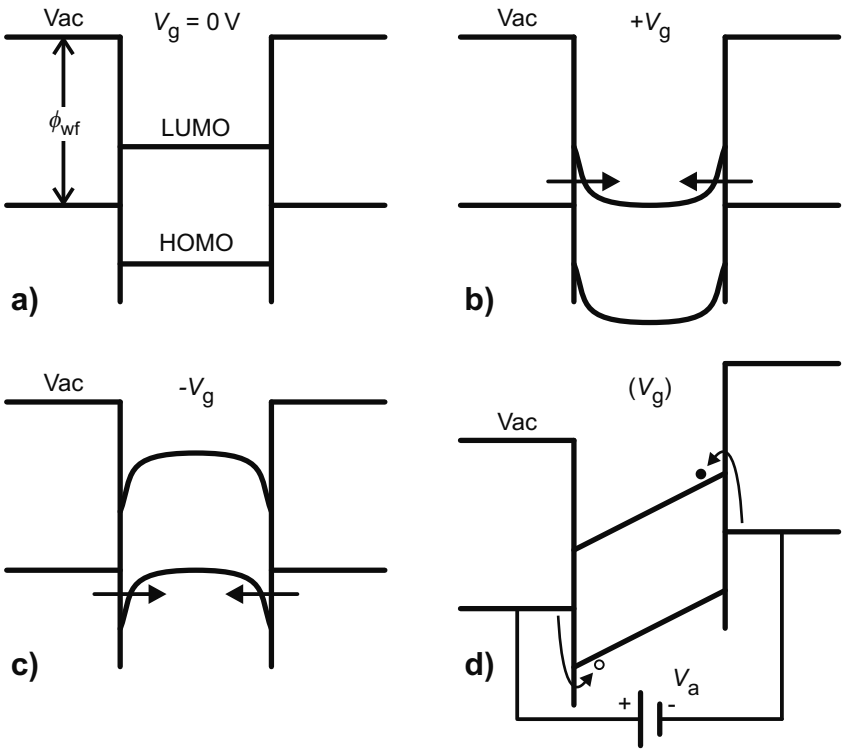

Figure 2.4: The effect of a gate potential on an ambipolar OFET. a) Unbiased device with zero gate potential, V_g. ϕ_{wf} is the work function of the electrode material. b) A positive gate potential "pulls" the energy bands down to the energy levels of the contacts, where electrons start to inject. c) A negative gate potential "pushes" the energy levels upwards until holes start to inject from the electrodes. d) A bias, V_a, is applied. The gate is tuned to equal the injection of charge carriers from the electrodes. Note that both electrodes source charge carriers and therefore the conventional "source" and "drain" labels do not apply.

high for electron and hole injection, ambipolar operation is possible as shown in fig. 2.4d. (The injection efficiency can be improved by applying different electrode materials with work functions closer to the HOMO and LUMO levels of the organic semiconductor, respectively, see e.g. [50]). In this scheme the gate can be used to tune the injection of holes and electrons. When the injection is approximately balanced, electroluminescence can be emitted[49]. Such light emitting OFETs are first of all very useful for the investigation of material properties, and how they behave in combination with their contact materials. Light emitting OFETs have been reported for different OFET configurations, see [49] for a review, and also for highly crystalline organic semiconductors as demonstrated by Bisri et al.[50].

2.1.1 First light emitting nanofiber OFET

Recently a novel operation mode of light emitting OFETs was proposed by Yamao et al.[51]. An AC voltage is applied to the gate electrode while the

semiconductor terminals ("source" and "drain") are biased symmetrically relative to the gate offset. This addresses the very important issue of contact resistance encountered in OFETs. If both injecting electrodes have significant barriers, a DC gate voltage cannot aid carrier injection at both electrodes simultaneously, see fig. 2.4d. However, when an AC gate potential is applied, the barriers to hole and electron injection are reduced in the negative and positive half-cycles of the gate signal, respectively.

This principle was first applied to *p*6P nanofiber OFETs by Kjelstrup-Hansen et al.[52], who observed electroluminescence. It should be noted that comparable thin film OFETs generally emitted electroluminescence from the electrode edges, not only in the gaps. A likely explanation is that the high gate potential caused injection of holes into trap states at both electrodes in the negative gate half-cycle, which subsequently recombined with electrons injected from both electrodes in the positive half-cycle. Although the observed light intensity was quite low, the experiment demonstrate a viable and general way of investigating the electroluminescent properties of organic nanofibers.

Chapter 3

Asymmetric top electrodes

This chapter describes the electron conducting properties of *p*6P nanofibers. The experimental method described was mainly developed during my employment at the Federal Institute for Materials Research and Testing (BAM) in Berlin, where preliminary work for this Ph.D.-project was conducted. Within this project the technique was further developed to the level applied in the following investigation.

The choice of lithographic method was quite important for the studies. Traditional UV- and E-beam lithography have the advantages of being well established and thus offer a wide range of optimized processes. However, although it may be possible to apply without severely bleach[53] or chemically alter the organic nanofibers, there are unknowns making alternatives worth to consider. For example the influence of contact with resists, their solvent, developer and remover cannot easily be said not to have an influence. The presence of moisture and liquids is a well established method of getting the organic nanofibers off their substrate[24], which could further complicate the fabrication. A simple and chemically clean lithography method is to use mechanical shadow masks to define electrode layouts. This does not perturb the devices with any liquid or solvent and thus removes these unknowns from the experiment. As will be evident from the following, a mechanical shadow mask furthermore protects the uncoated parts of the organic nanofibers from electromagnetic and particle radiation from the evaporation sources. Only the areas where contact materials are applied are exposed to the deposition process stresses, which is still considered to be relatively gentle to the organic material when low deposition rates are used[54, 55].

Initially the main reason for developing this prototyping method, was to screen various combinations of different electrode materials for OLEDs. While this was not successful the experiments yield useful results, which are described in this chapter. The following experiment demonstrates that devices conducting only one type of charge carrier can be used to investigate the conduction properties of the LUMO band. To do this a sample with Sm cathode and Au anode was fabricated. From the analysis the crystal domain size in the organic nanofibers can be extracted, which is an important physical parameter of the nanostructures due to the significant influence on the electrical conduction.

3.1 Fabrication technique

Asymmetric top electrodes[1] on organic nanofibers can be realized in several ways. The technique applied in this project has been developed with the aim of being able to apply and test different electrode materials on the organic nanofibers in a process with short turnaround time. The fast fabrication and testing was necessary because the main purpose of the method originally was to test various electrode material combinations. The second development criteria was a high yield and a need of producing many devices in parallel to ensure a sound statistical basis for interpretation of measurements. This is particularly important when investigating this type of organic nanofibers where large deviations between devices have been observed in previous investigations on individual nanofibers[24, 56].

One of the pillars in this fabrication is that devices are realized directly on the mica substrate where the nanofibers are grown. This is possible because mica happens to be a very good electrical insulator, thus being a suitable substrate for high-impedance devices. For prototyping there are obvious advantages to this approach:

- The nanofibers are not perturbed by any chemical or mechanical stress any transfer process may induce.
- No liquids are used making it easier to keep the sample clean and nanofiber detachment is avoided.
- All nanofibers are parallel over cm^2 areas so large arrays of devices can be made with nanofibers of the same orientation.
- Because mica is transparent both conventional and inverted optical microscopy can be applied for device testing.
- Sample preparation is relatively fast and reproducible.

The sample preparation starts by cutting a small flake off the mica substrate with nanofibers, since only a few square mm is actually needed for the devices. Typically the mica substrate is diced into flakes of $\sim 5 \times 10$ mm^2, which are easy to handle and still ensures that many samples can be made from the same mica substrate measuring 25×75 mm^2. The mica flake is glued onto a microscope glass slide for easy handling, while ensuring that the nanofibers are aligned perpendicular to the long microscope glass slide axis.

A mechanical shadow mask has to be placed on the sample to define the electrode gaps. To obtain small gaps a thin wire must be used. This is a tradeoff between having a wire sufficiently narrow, but still rugged enough to handle with macroscopic tools like tweezers. In these experiments the thinnest commercially available carbon fibre was used. This is considered to be very close to the optimum candidate for the job, since they can be down to ~ 5 μm wide, many centimeters long and still not break during handling. They are also just visible by the naked eye which eases the handling. Candidates for even thinner wires could be glass fibers or carbon nanotubes[57] (CNTs), which

[1] Here "asymmetric" refers to the application of different cathode and anode materials on the same device.

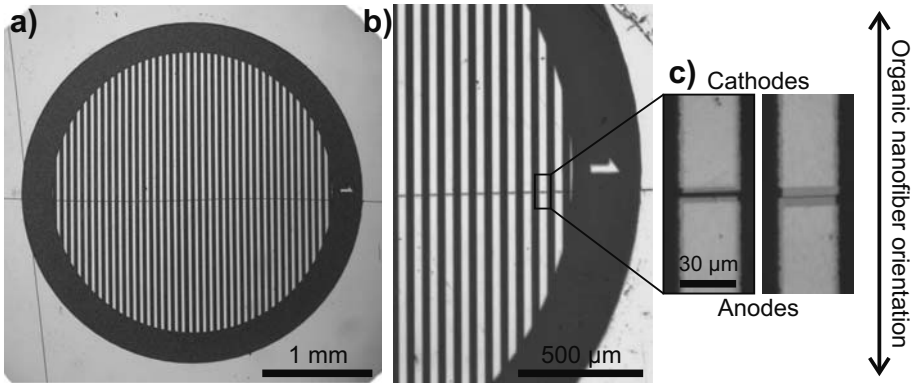

Figure 3.1: Optical microscope images of double shadow masking and the resulting electrodes. a) A Ni TEM-grid with two carbon fibers on a test substrate. The horizontal fiber intersects all windows through the center. The vertical fiber to the left elevates that side of the shadow masks to give the horizontal fiber a slope towards the surface. b) After angled deposition of two electrode materials, the shadow masks removed. c) Two devices; one with a several micron long gap due to small elevation of the shadowing fiber, the other with sub-micron gap due to significant elevation of the shadowing fiber at that device.

are worth to consider in order to push the lower gap size limit. Glass fibers are easy to make by heating a glass rod and pull, and can produce wires of submicron width. Compared to carbon fibres they are however quite brittle. Carbon nanotubes can be made in macroscopic sizes[58, 59] and should be strong enough to handle without breaking. Such CNT's could potentially make the smallest obtainable gap size of this shadow masking technique.

A roughly 2 cm section of carbon fiber was placed perpendicular across the organic nanofibers for shadow masking, using a pair of tweezers. On top of the carbon fiber a Ni TEM-grid[60] with 40 long windows was placed, so the fiber intersects the windows as shown in fig. 3.1. Thereby each window defines a device with a gap created by the shadow of the carbon fiber. 3.1. The slits are placed so the carbon fiber intersects all of them in the middle. As the electrode material is deposited, the mask will create up to 40 devices comprised of two electrode pads with a gap in between defined by the carbon fiber. Grids with a pitch of 62 µm was chosen to give a reasonable number of devices while still creating electrode pads wide enough to contact electrically with a simple probe. If the grid is fixed by mechanical clamping uneven mask-sample distance is difficult to avoid but important to control. Therefore a Ni grid is used for its ferromagnetic properties; a magnet on the backside of the sample can then be used to gently clamp the TEM-grid (and thereby also the carbon fiber) to the sample. Fixed masks are necessary when the sample is turned upside down in the contact material deposition chamber. The bars in the Ni grid tend to align with the magnetic field lines, so the magnet (or magnets) must be placed carefully to ensure correct fixture of the grid. The magnetic field lines must be parallel with the sample surface and the bars in the TEM-grid, see fig. 3.2. The sample is now ready to be inserted into the evaporation chamber to

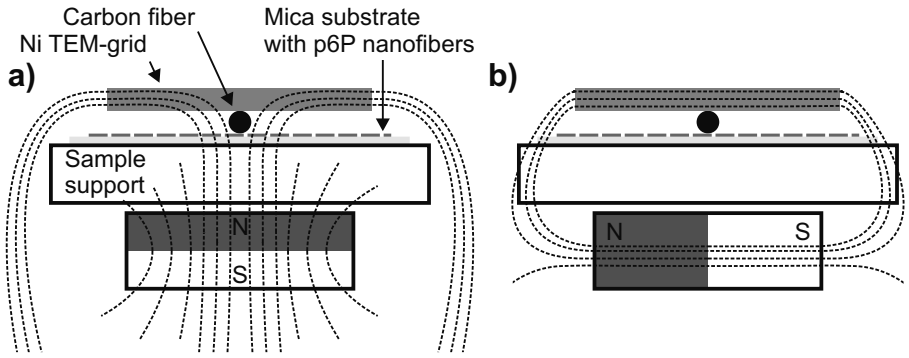

Figure 3.2: Two different ways of fixing a Ni TEM-grid to a sample by a magnetic field. Cross sectional view through a sample along a bar of the TEM-grid, represented by the gray beam. a) Using a small coin-shaped magnet. b) Using a rod-shaped magnet.

deposit electrode materials. In this project a custom-built thermal evaporation chamber was used. The chamber was constructed by me in a previous project, with the purpose of being able to deposit electrode materials from different crucibles at arbitrary angles without breaking the vacuum. These features were also used in this project.

3.1.1 Angled deposition

In the example used for this chapter the carbon fiber shadow mask was approximately 5.6 µm thick. If the electrode materials are deposited directly onto the sample with such a mask, the resulting electrode gap length would be similar to the shadow mask width. Device gaps several micrometers long necessitates impractical high testing voltages when using *p*6P nanofibers. To decrease the gap length the electrode materials were deposited at different angles. The advantage of angled deposition is twofold: the electrode gap can be designed down to sub-micron length and different electrode materials can be used for the cathode and anode to create asymmetric devices, see fig. 3.3. As described in detail in app. D, the angle of deposition can be calculated from the designed gap length when the z-position of the carbon fiber is measured. The carbon fiber elevation is measured using an optical microscope with precise digital readout on the stage. The shallow depth of field in a 50× 0.70 NA objective was used to determine the position of the sample surface and the top of the carbon fiber with sub-micron precision. The precise carbon fiber diameter was also determined with the optical microscope.

40 devices with approximately the same gap length can be useful to measure the statistical deviation with a fixed fabrication parameter set. However, more can be learned when an ensemble of devices with slightly different length is characterized electrically. To induce a length variation across the sample the shadow mask technique was extended by slightly elevating the carbon fiber at one end of the TEM-grid. This was done by placing another piece of carbon fiber on the sample before the two shadow masks, as shown in fig. 3.1. In this case the highest elevation of the shadow masking carbon fiber is used

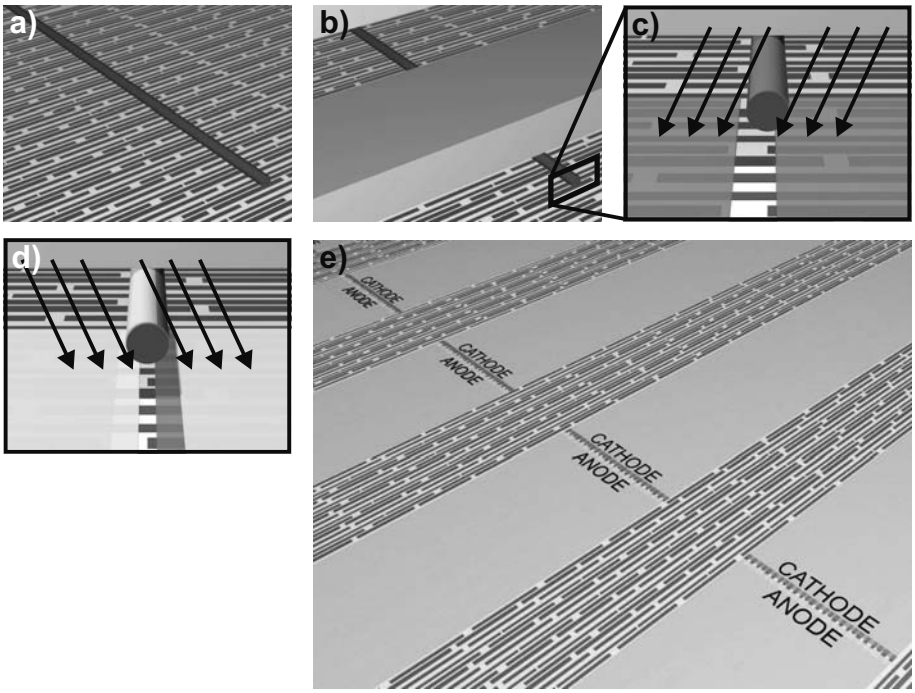

Figure 3.3: Physical vapor deposition of cathode and anode materials through a double shadow mask at different angles. Here the carbon fiber is elevated from the sample surface to illustrate how this decrease the device gap length. a) The carbon fiber is placed perpendicular to the *p*6P nanofibers. b) The Ni TEM-grid is placed. c) Cathode material is deposited. d) Anode material is deposited. e) The finished devices.

to determine the deposition angles. Typically one would aim at making the smallest gaps of zero length or less. This ensures that some of the devices on the sample are short circuited while the first device not short circuited will have the minimum length the given shadow mask geometry allows. The sample analyzed in this chapter is the example used in app. D to demonstrate how to determine the deposition angle and edge blur.

Lithography method evaluation

It is important to evaluate the precision of the chosen lithographic technique. First of all to determine if the result is close enough to the design and secondly if the devices are sufficiently well defined in terms of gap length. The primary tool for this evaluation is using SEM images. These were all acquired after the electrical measurements, in order to avoid carbon deposition from the microscope to influence the devices[61]. Scanning electron microscopy was chosen due to its high lateral resolution, good material contrast and also superior speed compared to e.g. AFM. Part of a device of the analyzed ensemble in this chapter is shown in fig. 3.4. From this the device length and electrode edge blur can be determined. The length uncertainty has also been estimated

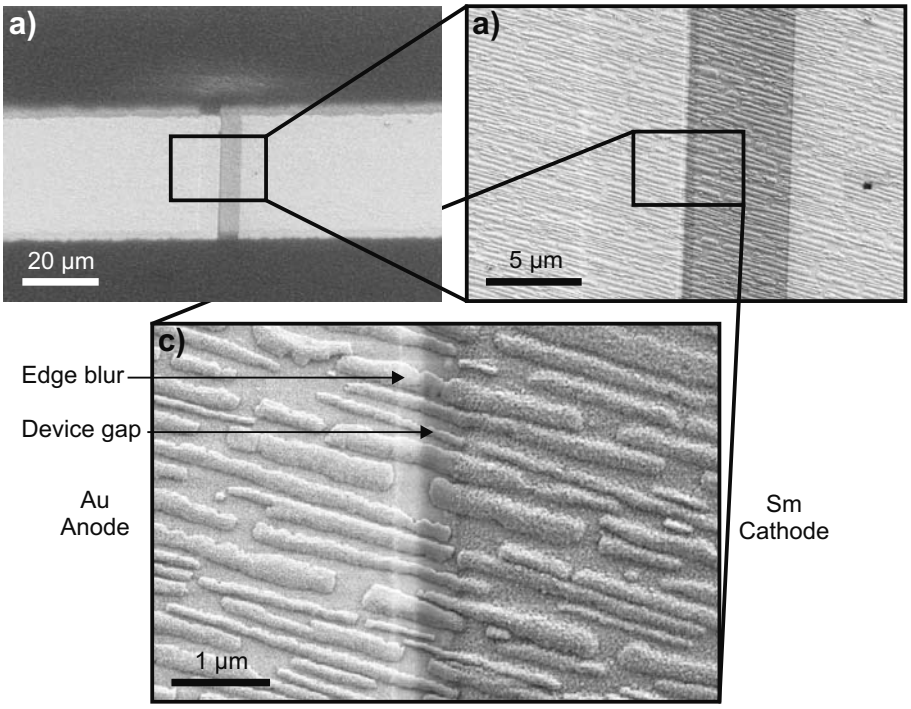

Figure 3.4: 1 kV SE2 SEM images of a *p*6P organic nanofiber device with estimated gap length of approximately 0.36µm. The Au layer is 30 nm and the Sm layer is 100 nm.

from SEM images. The minimum length is measured between the outermost metal clusters of the electrodes and the maximum is measured where the metal is definitely continuous. In fig. 3.4 the mean device length is determined to 0.36 µm. Knowing the deposition angle of 18° the equations in app. D can be used to calculate that the carbon fiber must have been elevated approximately 5.7 µm at this device. Again using the appendix the expected edge blur can be calculated to 0.25 µm, which corresponds well with the apparent Au edge blur of 0.26 $\pm$0.01 µm in fig. 3.4. It should be emphasized that the blur is *not* defining the maximum and minimum device length boundaries in the length uncertainty estimate; SEM images reveal that the metal film is continuous at less than the full film thickness.

On the particular sample analyzed in this chapter, 31 of the devices were working properly. The device length ranged from 0.36 to 3.9 µm. Uncertainty on the length ranged from approximately 0.20 µm on the shortest devices to 0.15 µm on the longest, which is natural since the carbon fiber is closer to the sample in the latter.

3.2 Electrical characterization of nanofiber devices

The electrical transport analysis explained in this section is the result of a close collaboration with Ole Hansen who has adapted the model from[62, pp. 36-37].

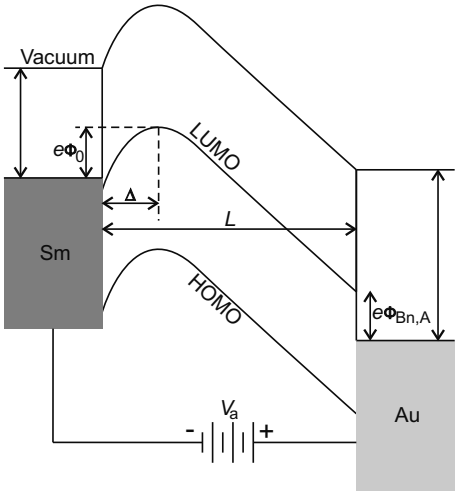

Figure 3.5: Energy diagram of a biased device according to the model picture[67]. Here the electron injection barrier from Sm is assumed negative.

A thorough explanation of the mathematical steps in this chapter can be found in app. E.

The electrical characterization was carried out by connecting all cathodes to a single wire with electrically conducting silver paste. The individual devices were then tested by contacting the anode with a moveable probe on a micromanipulation stage under a microscope, as described in app. C.2. Because Sm is oxidizing relatively fast in ambient air the cathode was made 100 nm thick and the electrical measurements were conducted immediately after the sample was retrieved from the evaporation chamber. Care was taken to make identical measurement history on every device throughout the measurement series, thus ensuring the best possible basis of comparison. The voltage increase was kept at a relatively medium rate of 1.2 V/s in order to keep the capacitive current offset low and constant for all devices. Thereby the offset could be consistently compensated for in the analysis. The measurements were conducted with the LabVIEW program described in app. C.2.1.

The Sm and Au electrodes were used as cathode and anode respectively. Because the charge carrier injection barriers are very different for the two metals with respect to *p*6P, it can be assumed that only electrons are conducted through the devices. Electrons have a ±0.1 eV barrier to the *p*6P LUMO level[63]. The hole barrier from Au has been reported to be 1.8 eV when *p*6P is deposited on Au[64], however, this may not apply in this case where Au is deposited onto the *p*6P nanofibers. But even if the barrier is only the difference between the Au work function of 5.1 eV[65] and the *p*6P HOMO level at 6.0 eV[63](see [66]) it would still be much larger than the electron injection barrier. Electrons injected from the Sm cathode and the built-in potentials may form an energy barrier, $e\Phi_0$, a small distance Δ from the Sm contact when a bias, V_a, is applied to the device. The energies of the device is illustrated in fig. 3.5. The entire device current is assumed to be electrons emitted over this barrier and transported by the electric field to the anode by a drift mechanism.

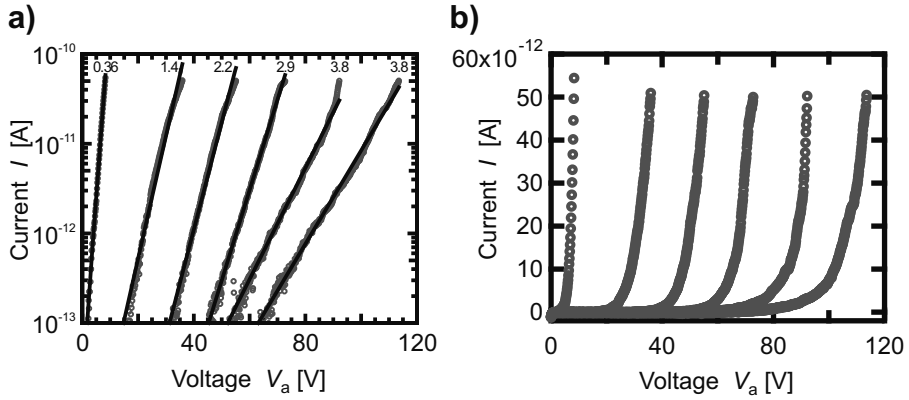

Figure 3.6: $I(V)$ characteristics of six different p6P nanofiber devices with Sm cathode and Au anode. a) semi-log plot with model fits. Device length is noted at each graph in µm. Courtesy of Ole Hansen. b) The same data on a linear plot.

And because p6P has a 3.1 eV band gap[63], it is assumed that the injected electrons are the only contributions to the space charge in the anode region of the device[2]. To describe the conduction the general expression of current density is used:

$$J = en\nu\left(E\right) \tag{3.1}$$

where e is the electron charge, n the carrier density and $\nu\left(E\right)$ the electric field dependent drift velocity. From this the space charge density in the anode region is given by $\rho = -en = -J/\nu\left(E\right)$.

The measured $I(V)$ characteristics all have similar shape like the six different devices in fig. 3.6. As evident from the almost linear shape in the semi-log plot the current must increase approximately exponentially when some threshold voltage is reached. Such nonlinear relation between electric field and drift velocity is often seen in organic semiconductors and has been modeled in different ways e.g. using the Mott-Gurney law[68]. Another popular example is to assume Poole-Frenkel-like hopping transport with a relation given by $\nu\left(E\right) = \mu_0 E \exp\sqrt{E/E_0}$ [69, 70], where μ_0 and E_0 are low field charge carrier mobility and electric field parameters, respectively. In this analysis, however, we have discovered that a hopping transport model consistent with Boltzmann-like particles jumping across one dimensional periodic energy barriers fits the data more consistently. The basic principle of the model is illustrated in fig. 3.7. Here the mean charge carrier velocity is given by:

$$\nu\left(E\right) = \nu_0 \sinh\left(\frac{E}{E_0}\right) \tag{3.2}$$

where ν_0 is a velocity parameter (see app. E for further details). In this model the electric field parameter is:

$$E_0 = \frac{2k_{\mathrm{B}}T}{ea} \tag{3.3}$$

[2]According to the Fermi-Dirac distribution only one state out of $\sim 10^{28}$ will be excited for a 3.1 eV band gap semiconductor at room temperature

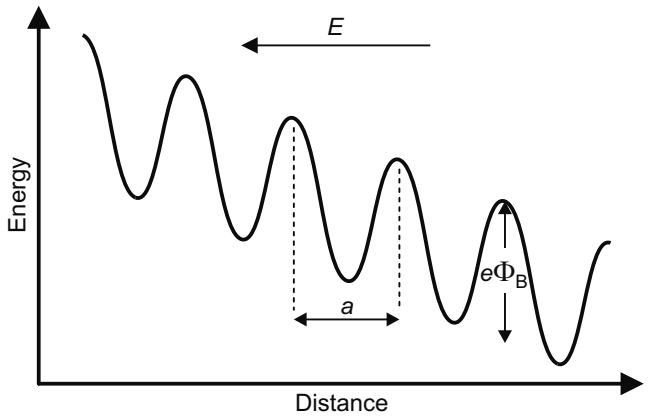

Figure 3.7: Conduction scheme of particles governed by Boltzmann statistics. $e\Phi_{\mathrm{B}}$ is the zero-field barrier and a the distance between barriers. Adapted from [62].

where k_{B} is Boltzmanns constant, T the absolute temperature and a the distance between the energy barriers shown in fig. 3.7. The drift velocity constant ν_0 depends on the distance between barriers, their height and the jump frequency. It is now possible to describe the potential drop from the barrier at $x = \Delta$ to the anode at $x = L$ by a one-dimensional Poisson equation:

$$\frac{d^2\Phi}{dx^2} = -\frac{dE}{dx} = -\frac{\rho}{\epsilon} = \frac{J}{\epsilon\nu_0 \sinh\left(\frac{E}{E_0}\right)} \tag{3.4}$$

where ϵ is the permittivity of the organic nanofibers. By integrating eq. (3.4) once the normalized electric field in the anode region is found:

$$\frac{E}{E_0} = \operatorname{arccosh} \frac{x - \Delta + \Lambda}{\Lambda} \tag{3.5}$$

where the characteristic length parameter $\Lambda = \epsilon\nu_0 E_0/J$ has been introduced for mathematical clarity. When the Poisson equation is integrated a second time, the potential drop across the anode region can be expressed by

$$\frac{\Phi}{E_0\Lambda} = \frac{L - \Delta + \Lambda}{\Lambda} \operatorname{arccosh} \frac{L - \Delta + \Lambda}{\Lambda} - \sqrt{\left(\frac{L - \Delta + \Lambda}{\Lambda}\right)^2 - 1} \tag{3.6}$$

At this point it is possible to evaluate how well the model fits the experimental data. The left hand side of eq. (3.6) is proportional to ΦJ since $1/\Lambda \propto J$. The length Δ can be assumed to be small, (as discussed in the following section), and the right hand side then depends on device length multiplied by current density, LJ. Therefore the model predicts ΦJ to be a unique function of LJ. When the applied voltage becomes significantly higher than the built-in barriers the potential drop $\Phi = V_{\mathrm{a}} + \Phi_0 - \Phi_{\mathrm{Bn,A}}$, (where $\Phi_{\mathrm{Bn,A}}$ is the LUMO to Au electron barrier - see fig. 3.5), is approximately the applied voltage, i.e. $\Phi \simeq V_{\mathrm{a}}$. Within these assumptions the measured data should fit the unique curve of the model, which they do, as shown in fig. 3.8. Compared to the Poole-Frenkel

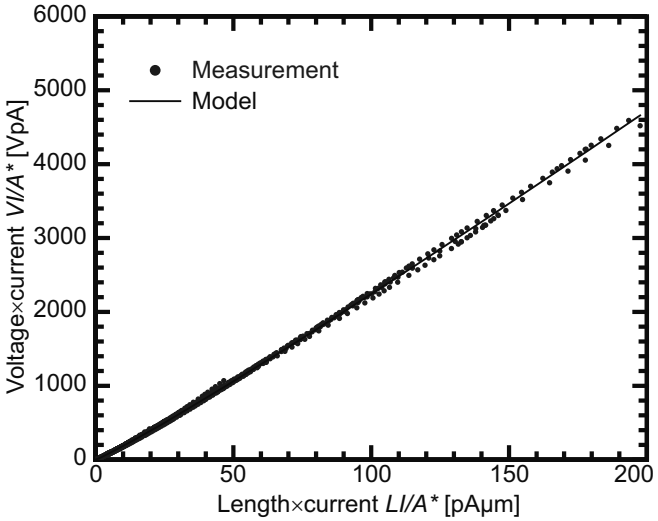

Figure 3.8: Conduction model compared to fits on measurements on seven different devices in the length range 0.36 μm to 3.9 μm. The data are corrected for the estimated relative cross-sectional area, A^*, which is in the order of 1 for all devices. The full line is the model from eq. (3.6). Courtesy of Ole Hansen.

theory the Boltzmann model was found to fit data slightly better.

If both $L \gg \Delta$ and $L \gg \Lambda$ is assumed eq. (3.6) simplifies to:

$$\frac{\Phi}{E_0 L} \cong \operatorname{arccosh}\left(1 + \frac{L}{\Lambda}\right) - 1 \tag{3.7}$$

This is solveable for $1/\Lambda$ and hence the current density. By introducing the device cross section parameter, A, the current can be expressed by:

$$I = A\frac{\epsilon\nu_0 E_0}{\Lambda} = A\frac{\epsilon\nu_0 E_0}{L}\left[\cosh\left(1 + \frac{\Phi}{E_0 L}\right) - 1\right] \tag{3.8}$$

The denominator $E_0 L = V_\mathrm{C}$ is a characteristic voltage parameter of the device. Note that from the definition of E_0 the characteristic voltage parameter is proportional to the number of barriers in the device, since $eV_\mathrm{C}/(2k_\mathrm{B}T) = L/a$. At this stage the model has been sufficiently simplified to readily be used to fit the experimental data (still assuming $\Phi \simeq V_\mathrm{a}$). $I(V)$ curves from all the 31 working devices have been fitted with eq. (3.8) and like the examples in fig. 3.6 show the fit is rather good. The characteristic voltages have been extracted from all the data fits and plotted against measured device length in fig. 3.9 The length uncertainty is estimated from SEM images as previously explained. The error on V_C is also on the plot but so small the black dot covers it. The $I(V)$ characteristic of each device has been measured at least twice; first up to 5 pA and then up to 50 pA. Figure 3.9 shows that the extracted V_C differs significantly between measurements, revealing that they are not completely stable. The blue triangles represent the average of measurements on each device and it is noticed that they within reasonable error follow the red line linear fit. The electric field parameter $E_0 = V_\mathrm{C}/L$ has been extracted from all

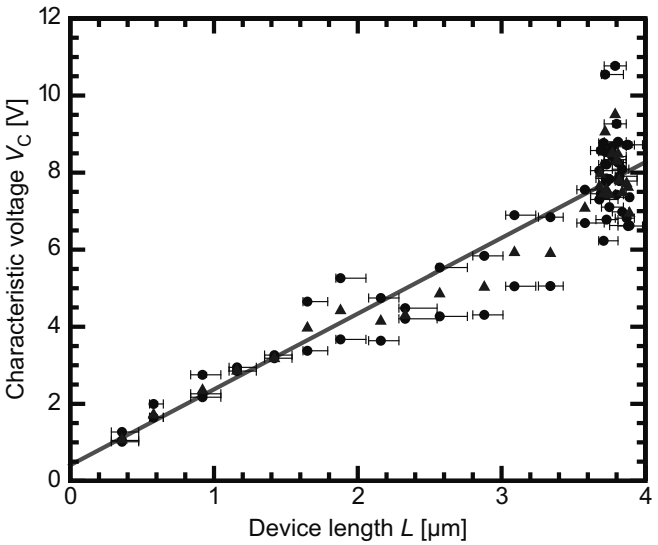

Figure 3.9: Characteristic voltage vs. length. The black dots are extracted values from $I(V)$ characteristics with length uncertainty indicated. The voltage uncertainty from the model fit is so low the black dots cover the vertical error bars. The blue triangles is the mean of measurements on single devices and the red line is a linear fit to the data. Courtesy of Ole Hansen.

the measurements using minimum, maximum and mean length values to give the result:

$$E_0 = 2.20 \pm 0.45 \text{ MV/m} \tag{3.9}$$

From eq. (3.3) it is possible to estimate the inter-barrier distance, a, assuming the devices to be at ambient temperature during the measurements:

$$a = 23 \pm 5 \text{ nm} \tag{3.10}$$

This result is in good agreement with a TEM study of *p*6P nanofibers grown on mica by Plank and co-workers[18] who find domain sizes of ∼20 nm. A similar TEM study performed on the *p*6P nanofibers used in this project indicated comparable domain sizes[3]. These results strongly suggest that the electrical conduction through these *p*6P nanofibers is limited by the presence of inter-domain boundaries in the nanofibers rather than contact resistances or resistance within the crystal domains (see fig. 3.7). For a study on the role of grain boundaries in *p*6P thin films, see [71].

In principle it should also be possible to extract ν_0 from eq. (3.8) if the effective cross section of the organic nanofibers, A, could be estimated[4]. This is however not the case; the variation of the fitting parameter $I_s = A\frac{\epsilon\nu_0 E_0}{L}$ is too large. We believe this is due to the variation of effective nanofiber cross section through the device ensemble. Statistically longer devices have less nanofibers that span the whole device gap and therefore also smaller cross section.

[3]TEM studies carried out in collaboration with Timothy John Booth.

[4]The relative permittivity along the long nanofiber axis has been estimated to 1.9 in[72].

3.2.1 Assumptions and Sources of error

This section describes the major sources of error to the experiment and the data treatment. The main assumptions used to simplify the conduction model are also validated. The simplest sources of error are listed below:

- The nanofibers span the gap at an angle of 16° which has not been taken into account. In a first approximation the device length could be divided by $\cos(16°) = 0.96$.
- The measurements were conducted in ambient air and the presence of water and oxygen could influence the measurement results. However, the effect of blowing dry nitrogen at the sample has previously been observed to be low. Elimination of such errors require either device encapsulation or measurements in high vacuum or inert atmosphere, which would significantly complicate data acquisition.
- The model does not include quantum mechanical tunneling effects.

As evident from the measurements in fig. 3.6 the devices are highly resistive. As a consequence the electrical measurements become sensitive to the voltage sweep speed through some capacitive effect of the system. This introduces a current offset in the $I(V)$ measurements, which is dependent on the voltage increase rate. A small preliminary study on the influence of the acquisition rate[5] has shown that the current has a small latency, meaning that $\frac{\mathrm{d}V}{\mathrm{d}t}$ must be small to approach a true DC $I(V)$ characteristic. Sweeping very slowly, however, (e.g. 0.1 V/s) will cause especially long devices to be subjected to a high voltage for several minutes. This tend to increase the risk of device failure; slow measurements typically show more dips and spikes in the current compared to faster measurements. So the choice of measurement speed is a tradeoff. It is an inherent problem when ensembles with different device lengths are investigated, since measurements on short devices will take shorter time than those on the long devices. Further measurements could clarify whether constant voltage ramp or electric field ramp gives better results. The current latency caused by the finite measurement speed causes the $I(V)$ characteristic to be less steep than it would be in a slower measurement. This means our model will overestimate the critical field parameter, E_0.

In the simplification of eq. (3.6) down to eq. (3.7), $\Delta \gg L$ and $\Lambda \gg L$ are assumed. Δ is the distance from the cathode edge to the position where the small potential barrier is maximum, see fig. 3.5. It corresponds to the Debye length along the *p*6P nanofiber, in other words the screening length. Unfortunately the Debye length depends on the carrier concentration, which is unknown on the left side of the potential barrier in fig. 3.5. However an ultraviolet photoelectron spectroscopy (UPS) study of *p*6P on Sm[63] reveals how well *p*6P screen the Sm potential. A layer of less than 10 nm *p*6P on a Sm surface completely screens the Sm electrons. Thus we can conclude that $\Delta \gg L$ indeed is true.

To evaluate if the assumption $\Lambda \gg L$ we consider the parameters involved:

$$L \gg \Lambda = \frac{\epsilon \nu_0 E_0}{J} = 2a\nu \exp\left(-\frac{e\Phi_\mathrm{B}}{k_\mathrm{B}T}\right) \frac{2k_\mathrm{B}T}{ea} \frac{A}{I} \tag{3.11}$$

[5]This experiment was conducted at BAM before this project was started.

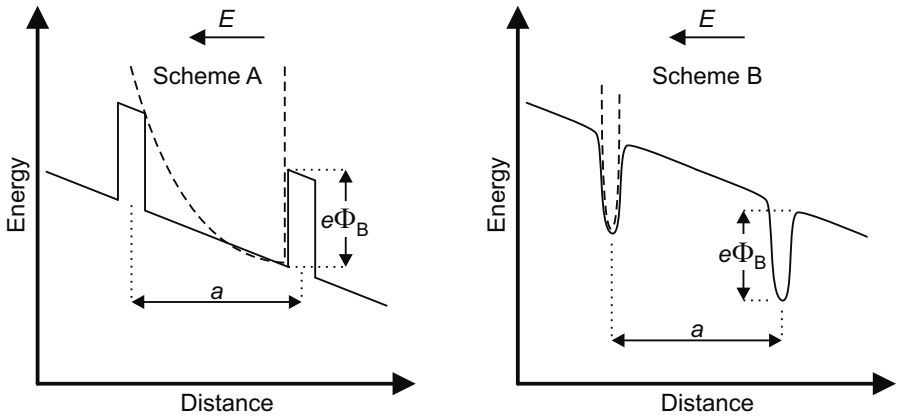

Figure 3.10: Two different potential schemes at the domains in the devices. Scheme A has a triangular well with energies approximated by an infinite "half" harmonic oscillator potential indicated with dashed lines. Scheme B has deep narrow wells at the domain boundaries approximated by an infinite harmonic oscillator potential indicated with a dashed line.

where Φ_B is the potential barrier between domains. This assumption should be valid for the shortest device, which is 0.36 µm, so it is reasonable to set the maximum allowable value of Λ to 10% of that. The largest cross sectional area can be estimated from the fact that the devices are 30 µm wide while the density of nanofibers makes the effective width approximately 15 µm. The average nanofiber thickness is approximately 20 nm. The maximum current is 50 pA. The relative permittivity has previously been estimated to 1.9[72]. The jump frequency, ν can be estimated by taking a closer look at the potential through the domains of the device. To do this two physically different schemes are illustrated in fig. 3.10. Although they are physically different, both fit the model described in this chapter. The electric field must be approximately constant throughout the device, due to the assumption that only electrons in transit contribute to the space charge. In scheme A the domains are represented by square quantum wells separated by thin positive inter-domain barriers. The well bottoms are sloped due to the high field strength of up to 30 MV/m. In this scheme the electron would reside close to the right hand side barriers and approximately behave as if it were in an infinite triangular potential well. The ground state energy, ε_0, of such a system is in the WKB approximation given by[73, pp. 130]:

$$\varepsilon_0 = \left(\frac{3\pi}{2}\left(1-\frac{1}{4}\right)\right)^{2/3}\left(\frac{e^2E^2\hbar^2}{2m_e}\right)^{1/3} \tag{3.12}$$

where m_e is the electron rest mass. Inserting the maximum electric field strength yields a ground state energy of 75 meV. The oscillation frequency of this state is approximated with that of a "half" harmonic oscillator's ground state (as shown in fig. 3.10)[74, pp. 290]. This happens to be the first excited state of a full harmonic oscillator[6], so the estimated jump frequency in this

[6]The infinite harmonic oscillator energies are governed by $\varepsilon_i = \left(i+\frac{1}{2}\right)\hbar\omega \quad , i = 0, 1, 2...$.

scheme becomes:

$$\varepsilon_1 = \frac{3}{2}\hbar\omega_{\mathrm{A}} \Leftrightarrow \nu_{\mathrm{A}} = \frac{2}{3}\frac{\varepsilon_1}{h} \tag{3.13}$$

This gives a frequency of 12 THz. Equation (3.11) can now be solved with all the estimated parameters, (setting $k_{\mathrm{B}}T = 75$ meV), and gives a barrier height of 1.0 eV. This is a relatively high barrier but the electric field strength is also quite large. Before the size of the barrier is considered any further, scheme B is evaluated.

In scheme B defects at the domain boundaries are represented by finite harmonic oscillator wells that trap the electrons for a period of time during the conduction. The model assumes the electron to be the only one in the trap and therefore reside in the ground state. If we in this scheme assume the electron only has the ambient thermal energy of 26 meV, the ground state frequency would be 13 THz. Solving eq. (3.11) with these parameters yields a barrier height of 0.35 eV. Scheme B implies that the electron is localized within approximately 4 nm (width of an infinite square well with 26 meV ground state). Such a well would however be 120 meV higher in one side relative to the the other, meaning the electron would mainly reside in one side of the well. This significantly perturbs scheme B towards that of scheme A when the applied electric field is as high as these devices demand.

Grain boundary barriers close to 1.0 V are relatively high, but not unreasonable [75]. This confirms that the assumption $L \gg \Lambda$ is fulfilled and thus it is reasonable to describe the physical system with the chosen model.

To evaluate if the applied electric field strength is reasonable, a comparison to a similar system is useful. The best single layer *p*6P OLED exhibiting a very low onset voltage was presented by Koch et al.[54]. It consists of an ITO anode, Al cathode and 200 nm *p*6P in between and by optimized sample preparation the electroluminescence onset is reduced to 3.5 V and the device is driven to 10 V. Although the driving voltages are low, the electric field strength range from 18 to 50 MV/m. Thus the 30 MV/m applied to the devices investigated in this chapter is considered reasonable.

3.3 Chapter summary

The prototyping method successfully produce devices from sub-micron to few microns length. The process is considered to have minimal effect on the fragile organic nanostructures compared to conventional micro-fabrication techniques and thereby comprise a good basis for intrinsic properties. A model based on simple classical principles has been developed to analyze the $I(V)$ measurements. From this the critical electric field parameter and structural domain size has been extracted. The model is general and can be used to compare different wide band gap nanodevices. It can also be used to evaluate device optimization by simple electrical testing. The assumptions made to simplify the model are evaluated and found to be reasonable, thus justifying their application. Compared to previous device fabrication methods investigating electrical properties of individual nanofibers[24, 56] this study clearly demonstrate the strength of fabricating many devices in parallel and using multiple nanofibers. Fabrication speed and device comparability have been very significantly improved. However, the main limitation of the described method is still considered to be in

the stability of the electrical testing. Reducing the influence of voltage ramping speed in the electrical testing should be the primary focus, if the method is to be developed further.

Repeating the experiment with longer nanofibers, which can be made[76], may give a more constant effective cross section of the conducting nanofiber channels throughout the device ensemble. This would enable the extraction of ν_0 and thus lead to a more detailed knowledge on the electrical properties of p6P nanofibers and potentially other nanofiber species as well.

To bring the research and development of organic nanofiber devices closer to a regime of broad technological relevance, low driving voltage is an important issue. This invariably means shorter electrode spacing or higher conductance. I believe the lower limit of the mechanical shadow masking technique can be pushed significantly further down by applying thinner wires which are already commercially available. However, alternative approaches may be more appropriate.

Chapter 4

Top electrodes on nanofibers

Several studies using *p*6P as electroluminescent material have been reported using different designs[23, 54, 77, 78, 79, 80, 81]. In particular the work of Yanagi and Okamoto[23] is interesting due to their application of crystalline *p*6P thin films epitaxially grown on KCl substrates. They find significantly higher electroluminescent performance of thin films with the *p*6P molecules oriented perpendicular to the applied field, compared to films with molecules oriented parallel to the field. This was attributed to the anisotropic conductance of the *p*6P crystal, where the orbital overlap is higher in the direction perpendicular to the molecular axis. For the crystalline *p*6P nanofibers investigated in this project, the long nanofiber axis is therefore anticipated to have good conductance. Investigation of the electroluminescent properties of *p*6P nanofibers could shed light on its use as an electrically driven nanoscopic light source, or generally on the use of crystalline OLEDs.

This chapter describes efforts aimed at making a nanofiber OLED by an approach using established practices. The idea was to engineer a method of contacting *p*6P nanofibers with the well known and working standard electrode combination of ITO and Al[54]. As discussed in chap. 2 this is not the most efficient design, however, simplicity is an important factor for initial development of a new fabrication method. If the basic concept proves successful, further transport layers can be added to the design.

Electrodes of ITO and Al are easy to apply in a traditional sandwich structure with sequential deposition of thin films, see fig. 4.1. The challenge lies in the difference between a continuous thin film and discrete nanofibers. While a thin film by simple means can be sandwiched between the contact materials of choice, nanofibers cannot, since the areas between nanofibers would short circuit the sandwich. The use of ITO complicates the process because it should be deposited in an oxygen background to avoid loss of oxygen[82]. At DTU Danchip a sputter system with the capability of ITO deposition in an oxygen background was available and therefore it was chosen to use this system. Previous reports show that ITO can be sputtered onto OLEDs without significant damage to the organic material[55]. However, this implied that the angled deposition technique described in chapter 3.1 could not readily be used since sputtering causes significant blur of electrode edges defined by mechanical shadow masks. Therefore I made a new device design, realizable with accessible techniques.

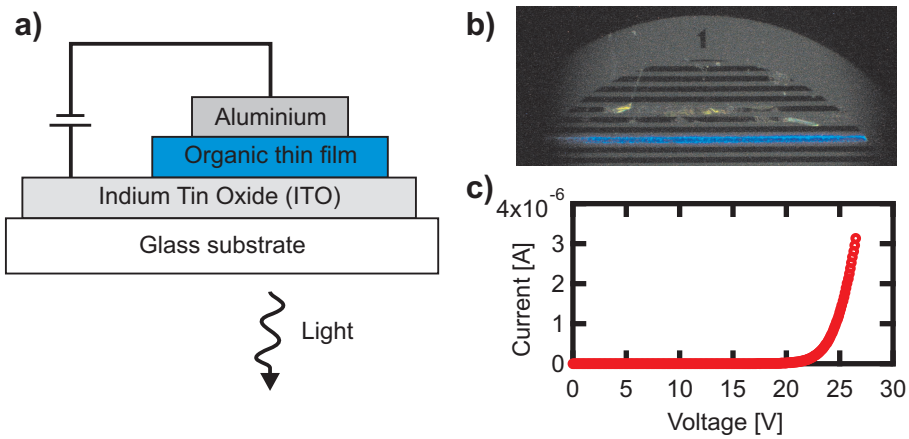

Figure 4.1: Standard sandwich OLED using *p*6P as active material. a) Conceptual sketch of design. b) Optical microscope image of several OLED devices defined by Al deposited through a TEM-grid shadow mask. Blue electroluminescence is visible from the biased device. Integration time 8 s, active device area 1950×30 µm^2. c) $I(V)$ characteristic of the OLED during the measurement in b). The *p*6P layer is approximately 200 nm thick.

To make a reference for further development and gain experience with the performance of sandwich *p*6P OLEDs a few sandwich OLED samples were fabricated, each with multiple devices, see fig. 4.1. First a commercial glass slide covered with ITO was cleaned in oxygen plasma and transported to a *p*6P deposition chamber. After depositing a 200 nm *p*6P thin film a shadow mask was placed on the sample and through that Al cathodes were deposited in a third chamber. Despite the non-optimized fabrication process where samples were transported through ambient air between depositions, almost all tested devices emitted light visible through the optical microscope. And even after 13 months of storage at ambient conditions the devices were still working. Although the electroluminescence efficiency was low, a measurable light emission is enough to enable testing of other electrode configurations. Subsequently device operation can be optimized e.g. by introduction of transport layers, see chap. 2.

The following sections describe three different ways to apply separated Al and ITO electrodes to *p*6P nanofibers. They share the basic design illustrated in fig. 4.2 where an insulating layer separates the Al electrode from the top ITO film. The separator coverage at the organic nanofiber defines the device length. One of the ideas behind this design is that devices can be formed directly on the *p*6P nanofibers as grown on the mica surface, making the prototyping less time consuming. An additional advantage of the design is encapsulation of the active parts of the organic nanofiber, thereby protecting it against influences from the ambient air.

4.1 Anodic oxidized separator

The method described in this section is based on forming the insulating separator in an anodic oxidation process where part of the Al electrode is converted

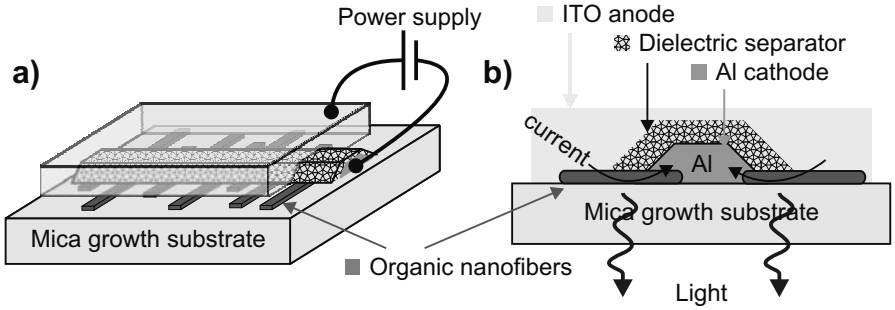

Figure 4.2: Working principle of top contacted nanofiber OLED. a) 3D view, b) cross sectional view. Organic nanofibers are dispersed on an insulating surface, e.g. as grown on the muscovite mica substrate. An Al electrode is deposited so that some nanofibers are only partly covered. A dielectric is either deposited on or grown on the Al, until a breakdown voltage higher than the operational voltage is obtained. Subsequently ITO is sputter deposited on the entire sample except for a small part of the Al electrode which is kept free. Power is supplied to the ITO and to the Al (the latter by punching a probe through the dielectric).

into aluminium oxide, Al_2O_3. The principle is to submerge the Al electrodes into an aqueous electrolyte solution through which an electric current is passed. When a positive voltage is applied to the Al, relative to an inert counter electrode, an oxide layer will be formed through the following reactions[83]:

$$\begin{aligned} \text{Al/oxide interface:} \quad & 2\,\mathrm{Al} + 3\,\mathrm{O}^{2-} \longrightarrow \mathrm{Al_2O_3} + 6\,\mathrm{e}^- \\ \text{oxide/electrolyte interface:} \quad & 2\,\mathrm{Al}^{3+} + 3\,\mathrm{H_2O} \longrightarrow \mathrm{Al_2O_3} + 6\,\mathrm{H}^+ \end{aligned}$$

The electric field drives the diffusion of O^{2-} and Al^{3+} ions through the oxide layer. Electrons will be drained by the Al anode and fed in at the cathode where hydrogen gas is formed by the reaction $6\,\mathrm{H}^+ + 6\,\mathrm{e}^- \longrightarrow 3\,\mathrm{H_2}$. Based on a literature survey and consultation of people at DTU Nanotech and DTU Danchip with experience in anodic oxidation of Al, a suitable electrolyte was chosen. Details of the buffered tartaric acid electrolyte mixture and the experimental procedures are described in app. C.3.

Formation of the electrode separator by partly anodic oxidation of the Al electrode should give a good control of oxide thickness and there are only few constraints on electrode layout. The thickness is controlled through the oxidation process; for a good quality Al_2O_3 layer the field driving the oxidation process would stop at about 0.83 V/nm[83] at room temperature, which approximately corresponds to the breakdown voltage of the oxide. Thus by setting the compliance voltage to 100 V the oxide layer would ideally become approximately 120 nm. The shape of the electrodes on the nanofiber sample does not influence the oxidation process, so any geometry such as branched and high density patterns with small features can be supported; devices will form on all nanofibers protruding out under the Al electrode. For prototyping Al electrode arrays were formed by e-beam physical vapor deposition (PVD) through a TEM-grid shadow mask with 40 long slits oriented as shown in fig. 4.3.

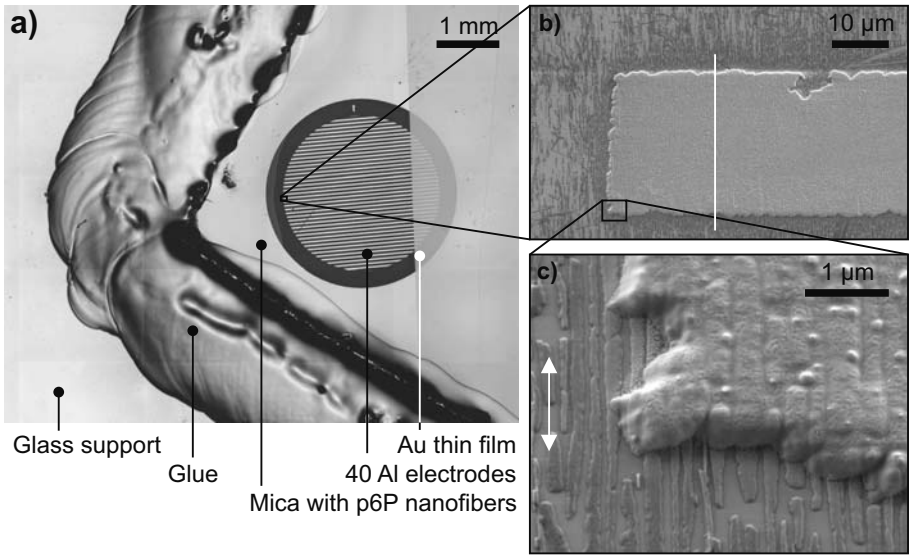

Figure 4.3: Al electrode pattern on *p*6P nanofibers on mica. a) Optical microscope image of a glass support upon which a flake of mica with *p*6P nanofibers has been glued. A Ni TEM-grid (see fig. 3.1a pp. 17) has been used as shadow mask during Al deposition. The Ni TEM-grid was attached to the sample with a magnet (as shown in fig. 3.2 pp. 18, but without the carbon fiber). Subsequently an Au film was deposited to cover part of the Al electrodes for common electrical connection during anodic oxidation. b) 1 kV SE2 SEM image of part of an Al electrode after anodic oxidation. It is noticed that some of the *p*6P nanofibers have been washed off. (The white line indicate where the profile shown in fig. 4.5a is measured). c) 1 kV SE2 SEM zoom of the tip edge of the Al electrode in b), the sample is tilted 25° for better view of the lower edge. The white double arrow indicate the *p*6P nanofiber orientation. At the lower edge the nanofibers are partly covered by the Al electrode and partly exposed. (a) is a different but similar sample to that presented in b) and c)).

4.1.1 Test results using anodic oxidized separator

Several experiments were conducted to test the method. Oxidation tests of Al films on glass showed the expected initial linear increase in voltage up to the compliance, and while maintaining the compliance voltage, the current rapidly dropped on a smooth power law curve, see fig. 4.4a. However, the oxidation characteristics of a sample with Al electrodes on *p*6P nanofibers reveal unexpected behavior; the rise in voltage is not completely linear and there are sudden increases in current during constant voltage supply, see fig. 4.4b. After the oxidation process the edge morphology of the electrodes were investigated. Optical microscopy immediately revealed that the electrolyte had intruded under the edges, primarily along the *p*6P nanofibers. At the end of the electrode, where nanofibers are parallel to the edge, intrusion is far less pronounced. Figure 4.5 shows images of a part of an electrode that has been torn off the sample with a manipulation probe. The electrode profile in fig. 4.5a shows the increased thickness at the edges which partly stems from the enhanced electric field due

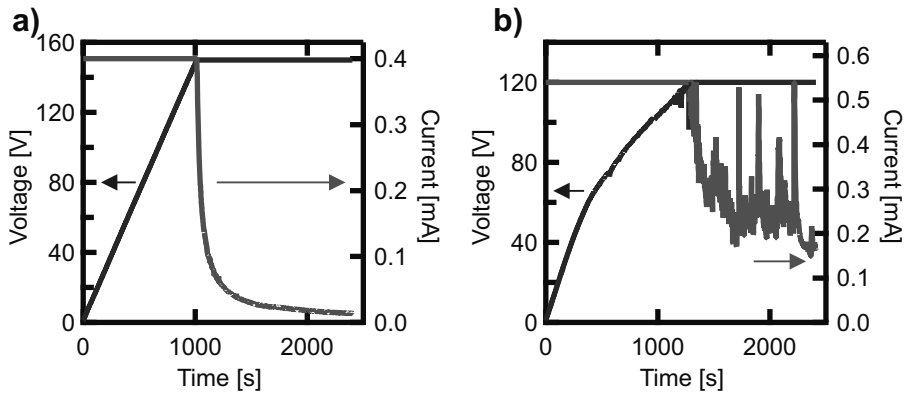

Figure 4.4: Typical electrical characteristics of two different anodic oxidation experiments. a) Oxidation of a reference sample; approximately 1 cm^2 Al electrode on a bare glass substrate. b) Oxidation process of Al on the sample shown in fig. 4.3b+c. Submerged electrode area is approximately 1.35 cm^2. In both experiments the current density is approximately 0.4 mA/cm^2.

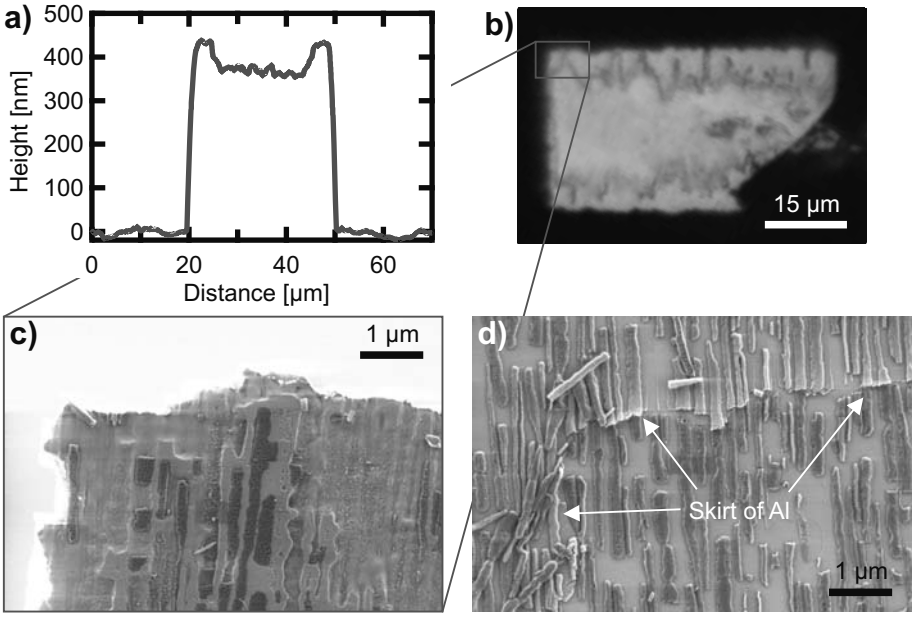

Figure 4.5: Investigation of electrode edges after anodic oxidation. a) Height profile of the oxidized Al electrode along the white line in fig. 4.3b measured with a stylus profilometer. b) Optical microscope image of the underside of the electrode tip shown in fig. 4.3b after it was torn off the surface. c) 1 kV SE2 SEM image of the backside of the oxidized Al electrode tip shown in fig. 4.3c. d) 1 kV SE2 SEM image of the *p*6P nanofibers on the mica substrate after the oxidized Al electrode was torn off. This is at the upper left corner of the electrode shown in fig. 4.3b. A thin skirt of oxidized Al remains on the nanofibers not previously covered by the electrode.

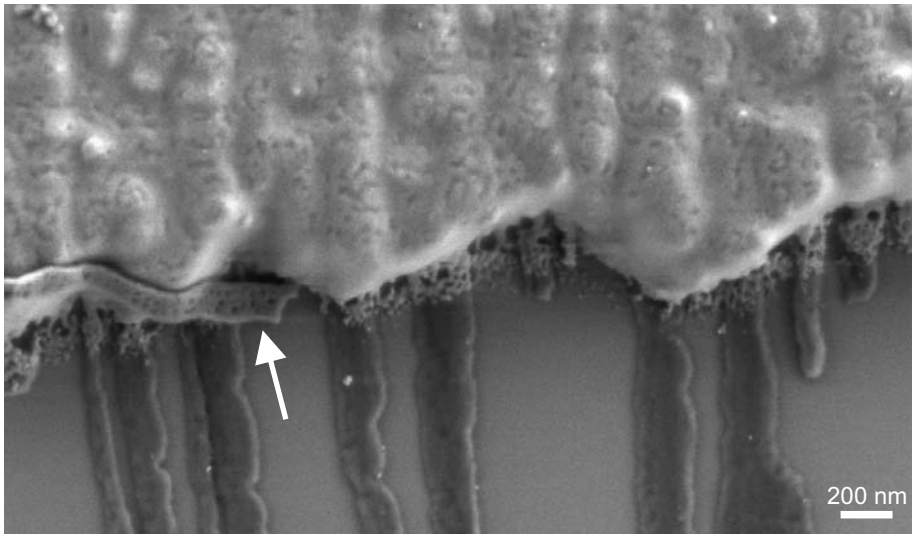

Figure 4.6: 1 kV SE2 SEM image of the oxidized Al electrode edge after removing the electrode skirt in NaOH solution. Only minor residues of the skirt remains while the rest of the exposed nanofiber has been cleaned. The majority of *p*6P nanofibers are washed off by the cleaning treatment except those partly pinned by the electrode. A loosened nanofiber has stuck to the electrode edge in the left part of the image (indicated by arrow).

to the sharp edge, but also because of the oxidation at the Al/nanofiber interface. Another problem, which would inhibit the ITO top layer from getting proper contact with the *p*6P nanofibers close to the electrode edge, is the thin skirt visible in fig. 4.5c.

High and low deposition rates of the Al electrodes were tested, to investigate if a stress in the electrodes caused the delamination, with no improvement. Since the Al or an alternative cathode material should be in direct contact with the *p*6P nanofibers possible candidates for an adhesion layer are few.

The thin skirt around the Al electrode edge was assumed also to be Al from the deposition process. To remove this, the sample was submerged in a diluted NaOH solution which successfully removed the skirt in one experiment, see fig. 4.6 but in other cases made the electrodes detach (see details in app. C.3).

In some areas on the sample the edge detachment appeared less pronounced, and to evaluate if just a few nanofibers were contacted properly when an ITO layer was sputtered on, a few samples were finished and tested electrically. The quality of the anodic oxide layer was tested by measuring breakdown voltages of small capacitor structures formed on the oxidation test samples. Dielectric breakdown at typically half of the compliance voltages used in the oxidation process was observed, which should be sufficient for these prototyping experiments. Electrical testing of samples with *p*6P nanofibers was conducted while recording live video of the sample with a cooled electron multiplying CCD (EMCCD) camera mounted on an inverted optical microscope, see app. C.2. Devices were tested until dielectric breakdown destroyed them. None of the

tested samples emitted visible light that could be from electroluminescing *p*6P nanofibers. Measurements typically ended in a flash where subsequent SEM imaging revealed that a point on the electrodes had melted.

4.1.2 Evaluation of anodic oxidized separator

The strength of the process lies in the easily controlled conformal oxide formation ensuring that the Al electrode is properly insulated. The process independency on electrode layout is also a useful feature. The challenge is that oxidation intrudes under the electrodes along the nanofibers during oxidation and thereby destroys the Al/nanofiber interface. An adhesion layer under the Al with similar electrical contact properties may be a viable path to stop the electrolyte from intruding under the electrodes. Possible candidates could be Cr ($\phi_{\mathrm{wf}} = 4.5$ eV) or Ti ($\phi_{\mathrm{wf}} = 4.3$ eV) which are both common adhesion layers with work functions comparable to that of Al ($\phi_{\mathrm{wf}} = 4.3$ eV)[65]. To assess if they will work as cathodes to *p*6P, they could initially be tested in the normal sandwich structure shown in fig. 4.1. Other possibilities could be to change electrolyte or speed of oxidation.

It may be that the problems could be solved, but no obvious solution was at hand. Since the remaining development time of the method at this point was impossible to estimate these experiments were stopped. Instead time was spent on other methods that were more likely to realize the device design.

4.2 Reactively deposited Al_2O_3 separator

A dielectric separator can be formed on the Al electrodes by subsequent deposition of Al_2O_3 through the same mechanical shadow mask. When using a slightly elevated shadow mask, coverage of the electrode edges can be controlled either by slightly tilting the sample or, if possible, broaden the aperture of the deposition source. The Al_2O_3 can be vapor deposited in several ways. Sputtering is often used to deposit oxides but is not a viable method here due to the lack of well defined electrode edges when using elevated mechanical shadow masks. Thermal deposition of Al_2O_3 is possible but must be done in an oxygen ambient to avoid oxygen deficiency in the deposited film[84]. At the time of the experiments the only system readily available where an oxygen ambient could be allowed was the thermal deposition system described in app. C.1. Thus a series of experiments were performed on this system to investigate the possibilities of forming a sufficiently insulating Al_2O_3 separator on top of the Al electrodes. Due to the limited heating power of the system Al_2O_3 could not be evaporated. Instead reactive deposition of Al was used. In this approach Al is deposited while a background pressure of oxygen is maintained in the chamber. If all Al should react with oxygen into Al_2O_3 the flux of Al must be kept below 4/3 the flux of O_2, assuming all oxygen is chemisorbed. From this condition the maximum allowable deposition rate at a given oxygen pressure can be determined. The flux of gas molecules onto a surface, F, is described by (see [85]):

$$F_{\mathrm{O}_2} = \frac{p_{\mathrm{O}_2}}{\sqrt{2\pi m_{\mathrm{O}_2} k_{\mathrm{B}} T}} \tag{4.1}$$

where p_{O_2} is the partial pressure of oxygen and m_{O_2} the molecular mass of O_2. Due to the safety issues related to using pure oxygen gas, the experiments were performed with ambient air either dried through a cryo trap or deliberately humidified[1]. The highest allowable pressure during evaporation while still maintaining a line-of-sight deposition can be calculated by demanding a mean free path of particles much larger than the source to sample distance. The mean free path is given by[87, pp. 526]:

$$l_{\mathrm{mfp}} = \frac{k_{\mathrm{B}}T}{\sqrt{2}p\pi(2r_{O_2})^2} \tag{4.2}$$

where the radius of the oxygen molecules $r_{O_2} \approx 0.1$ nm is assumed to represent the average of the present gas. At ambient temperature and a pressure of 10^{-5} mbar the mean free path will be in the order of 20 m, which is considered sufficient to maintain a directed deposition of metal. Assuming an O_2:N_2 ratio of 1:4 an ambient air background pressure of 10^{-5} mbar will result in a F_{O_2} of $5 \times 10^{18} \frac{1}{\mathrm{m^2 s}}$. It is now possible to determine the maximum deposition rate of Al:

$$\frac{\frac{4}{3}F_{O_2}m_{\mathrm{Al}}}{\rho_{\mathrm{Al}}} = R_{max} \tag{4.3}$$

where $m_{\mathrm{Al}} = 26.98 \times m_{\mathrm{n}}$ is the mass of an Al atom and $\rho_{\mathrm{Al}} = 2698 \frac{\mathrm{kg}}{\mathrm{m^3}}$ the density of bulk Al. This gives a maximum rate of 0.12 nm/s, which is high enough to obtain a reasonable process time, even if a deposition in the order of 100 nm is required for appropriate separator thickness. Thus a series of experiments were carried out to investigate if it was possible to deposit insulating Al_2O_3.

4.2.1 Test results of reactive Al_2O_3 deposition

In total six samples were made with different deposition conditions. In the experiment with the highest pressure the background pressure was increased by 7.5×10^{-5} mbar (with humid air) and the Al deposition rate was kept at 0.03 nm/s.[2] The samples were evaluated by measuring the oxide breakdown voltage. This was accomplished by depositing an array of small electrode pads to create capacitor structures. All the samples showed breakdown voltages below 20 V or an ohmic resistance less than 100 kΩ.

To investigate possible reasons for the very poor insulating performance of the Al_2O_3 an energy dispersive X-ray spectroscopy (EDX) analysis was carried out. The before-mentioned sample fabricated with the highest background pressure and lowest Al deposition rate had the EDX spectrum shown in fig. 4.7b. The spectrum was recorded at normal incidence with a 5 keV electron beam. At this energy both Al and O atoms are probed, while keeping the sampling volume close to the surface. Monte carlo simulations were used to determine the penetration depth of approximately 180 nm, which was also the measured thickness of the deposited Al_2O_3 layer. The simulated spectrum of stoichiometric Al_2O_3 in fig. 4.7a reveals that the oxygen content is actually higher in the deposited film. In a study by Jeurgens et at. [85] this was

[1] Humid atmospheres are used in other studies to promote Al oxidation, see e.g. [86].

[2] The subsequent EDX study revealed that the layer was almost stoichiometric Al2O3. Assuming it has Al2O3 density, the measured film thickness and the duration of the deposition was used to calculate the actual Al deposition speed.

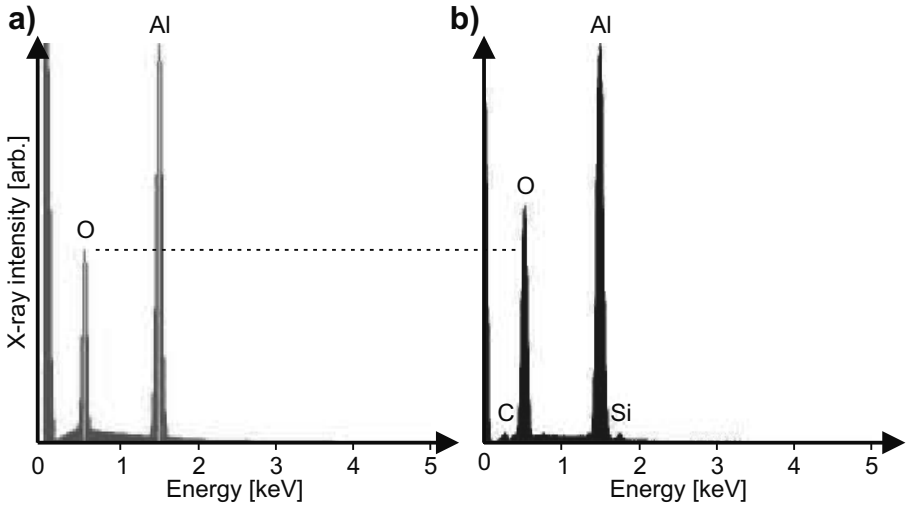

Figure 4.7: EDX spectra of Al_2O_3. a) Simulated spectrum (courtesy of Andy Horsewell). b) Measured spectrum. The spectra have been scaled to the same magnitude of the Al signal in order to compare the concentrations of oxygen.

typical for oxide films grown at temperatures lower than 573 K, however in a process where oxidation was done after Al deposition. The fact that the deposited film contains enough oxygen strongly indicates the formation of Al_2O_3 is not limited by the presence of O_2 as was initially anticipated. In later communications Jørn Bindslev Hansen from DTU Physics disclosed experimental details clearly indicating that stoichiometric Al_2O_3 can be obtained by very slow Al deposition with a pure O_2 background pressure[88]. Further details of the experiments of J. B. Hansen and coworkers cannot be disclosed here due to unpublished results.

4.2.2 Evaluation of reactive Al_2O_3 deposition

Although experiments show that stoichiometric Al_2O_3 can be formed by deposition of Al in an O_2 background at room temperature, they also reveal it is non-trivial to do so and obtain good electrical insulating properties. The main error is believed to be the assumption of 100% O_2 chemisorption on Al; Jeurgens et al.[85] quote a sticking probability of only 10^{-3} to 10^{-2} on bare Al. After solving the issues of forming stoichiometric Al_2O_3, the question still remains if the electrically insulating properties will be good enough and the coverage of the separator layer controllable. The anticipated development time needed to fully evaluate this method could not be fitted within the time frames of this project, and the method was abandoned.

4.3 Vapor deposited SiO_x separator

Simple deposition of a separator layer was tested using SiO_x as an alternative to the previously described reactive deposition of Al_2O_3. Vapour deposited SiO_x is a relatively poor electrical insulator, hence a relatively thick layer should

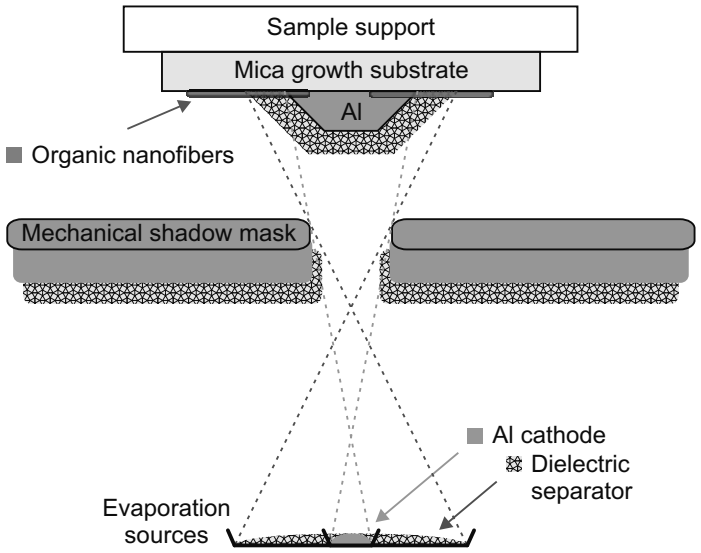

Figure 4.8: Principle of deposition of Al electrode and separator dielectric through the same mechanical shadow mask by controlling the source aperture size.

be required. These experiments were conducted in collaboration with Jakob Kjelstrup-Hansen who assisted in fabrication.

The device was fabricated by depositing Al followed by a separator layer of SiO_x through a mechanical shadow mask. To control separator coverage of the Al electrode different source apertures were used as illustrated in fig. 4.8. An E-beam PVD system was used to deposit first Al electrodes through a mechanical shadow mask. By focusing the E-beam to a small spot the effective source aperture was only few mm. Without moving the sample the source material was changed to SiO_x by rotating the hearth[3], thus maintaining the exact same source position relative to the sample. The SiO_x separator layer was deposited by sweeping the E-beam over a larger area, thus effectively creating a larger source aperture. Using the calculations of electrode edge blur and relevant experimental parameters given in app. D, pp. 94, the Al electrode edge blur was in the final tests designed to be $\sim$0.4 µm and the SiO_x blur $\sim$1.4 µm. Finally the ITO anode was sputtered on and the devices were ready for testing. Two types of devices were fabricated in this way. The most robust experiment was made by using nanofibers as grown on mica. In another experiment we used nanofibers transferred to a flexible transparent foil, to evaluate if the process could be made on this versatile substrate.

4.3.1 Test results using SiO_x separator

Scanning electron microscopy of parts of the samples before applying the ITO electrode revealed a thin skirt of SiO_x next to the electrode. This was similar to

[3]The E-beam PVD system has a stationary E-beam gun and a hearth designed as a carousel with a number of slots for source materials. To deposit a different material the carousel is rotated to bring the selected source into the target area of the gun.

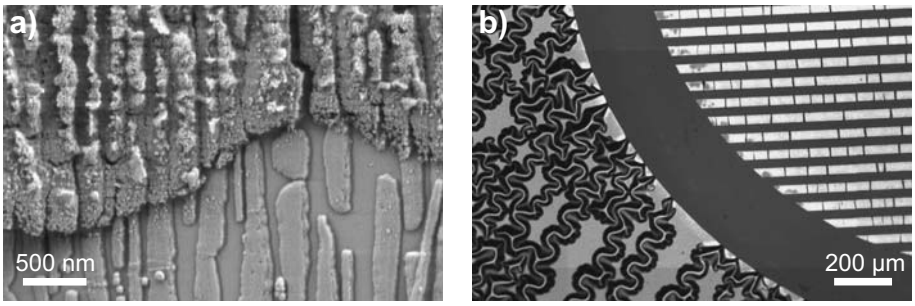

Figure 4.9: SiO_x covered electrodes after attempted removal of the edge skirt by HF vapor etching. a) 1 kV SE2 SEM image of an electrode edge which has partly detached from the sample. b) Optical microscope image of the same sample. The thin film has buckled severely outside the masked area (left part), while the long electrodes of the devices have not buckled as much.

what was observed at the electrode edges after anodic oxidation (see fig. 4.5d). The most gentle way to remove this unwanted SiO_x is to use HF vapor etching in the following overall reaction[89]:

$$SiO_2 + 4\,HF(g) \longrightarrow SiF_4(g) + 2\,H_2O \tag{4.4}$$

The primary etching happens when HF dissolve in a thin layer of condensed H_2O on the sample. There are intermediate chemical steps of the reaction but the overall result is the removal of SiO_2 through the gas phase. Subsequent inspection by SEM is shown in fig. 4.9a. The etching was too excessive but the most important result of the experiment is that the skirt indeed has been removed without any apparent damage to the *p*6P nanofibers. This is a promising result if the method is to be further developed. The image also shows another important issue regarding the use of SiO_x: the electrode has detached from the substrate. The optical microscope image in fig. 4.9b shows how the SiO_x covered part of the sample is buckled. The buckling was observed to progress during the course of days where samples were stored in ambient air. To evaluate if the fabrication principle was working, the device fabrication and electrical testing was conducted before the electrodes detached from the sample.

Electrical testing was performed on an inverted microscope with a sensitive EMCCD camera, see setup description in app. C.2 and C.2.1. Image stacks were recorded synchronous with $I(V)$ characterization by the LabVIEW program. In several experiments light emission at the electrode edges was observed both on the foil and mica substrate samples. Figure 4.10 shows an example of one such measurement (on a sample where the SiO_x skirt has not been removed by HF vapor etching). The image sequence acquired with the EMCCD camera show that light is emitted from the edge of the device only, as would be expected if it was electroluminescence from the organic nanofibers. The course of the voltage sweep conceptually follows that of the light intensity and there are no spikes in the $I(V)$ plot that could indicate breakdown events. However, comparing the electrical measurement with that of the sandwich OLED shown in fig. 4.1 indicate significant differences. The nanofiber device length

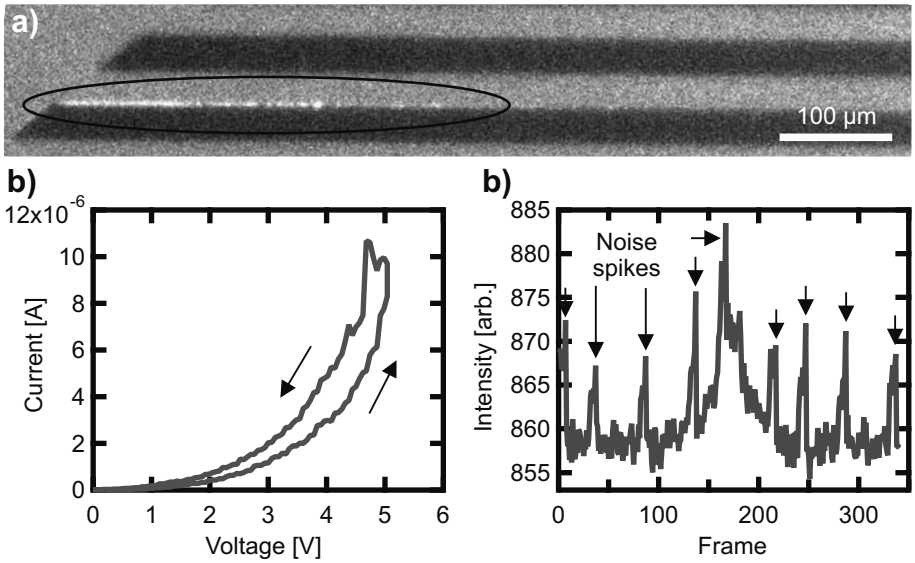

Figure 4.10: Observed light emission from sample edge during electrical characterization. a) Optical microscope image acquired with EMCCD camera (average of the frames 150-200). Light emitting spots at the electrode edge are encircled. b) $I(V)$ characteristic of the measurement showing higher current when the voltage is swept back to zero. c) Image intensity of the of the frames recorded synchronous with the electrical measurement (at 10 fps). The spikes in the intensity marked with small arrows are noise fluctuations in the average image intensity and not from the spots that emit light. The change in average intensity of the image seems to follow the course of the electrical measurement.

was designed to be ∼1 µm compared to 200 nm in the sandwich OLED. Longer devices typically demands higher working voltage, thus detectable light emission below 5 V appears to be "too good". Post inspection of the sample by SEM did not reveal any surface damage, however optical microscope images revealed visible changes in the device, see fig. 4.11. Judging from the black spots at the electrode where the light emission was detected and from the $I(V)$ characteristic, I find it most likely that the detected light is not electroluminescence from the organic nanofibers. An SEM image of the samples made on foil substrates after electrical testing, where light emission was observed, clearly shows molten spots at the electrode edge, see fig. 4.11d.

4.3.2 Evaluation of SiO_x separator

The results show that the SiO_x insulator was too thin at the critical electrode edges to support voltages high enough for charge injection into the organic nanofibers. This may be attributed to the poor insulating properties of PVD SiO_x and insufficient control of the edge coverage. The stress causing the SiO_x film to buckle is another problem of the process, which exact origin and solution has not been looked into. If further developments of the method is desired, the most important aspect is considered to gain much better control

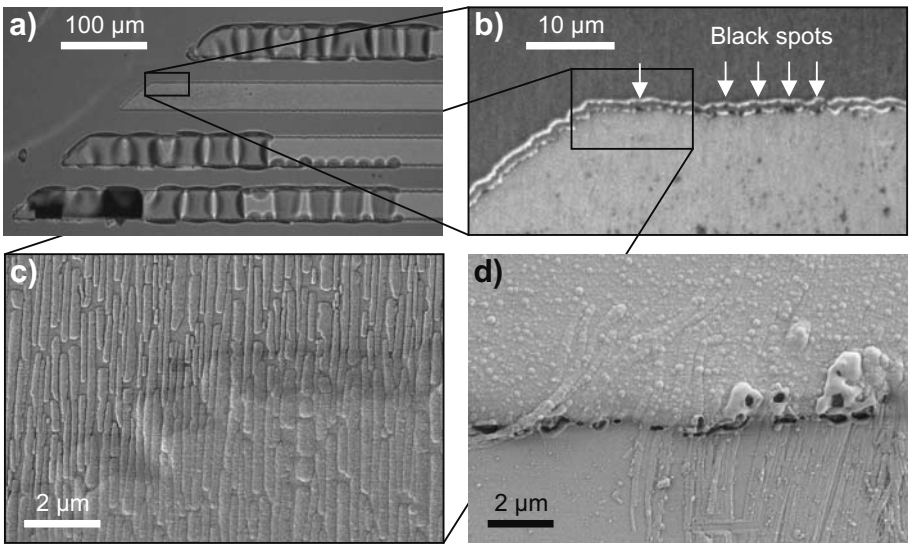

Figure 4.11: Investigation of damages at the electrode edges. a) Optical microscope image of the device in fig. 4.10 several months after the measurements. Notice the severe buckling of the neighbor devices. b) A zoom in on the edge where light emission was observed. Black spots are visible at the edge only where light was emitted. c) 1 kV SE2 SEM image of the electrode edge in b). The damage is not visible on the surface of the 500 nm thick SiO_x layer. d) 1 kV SE2 SEM image of the electrode edge of a similar device realized on a foil substrate where *p*6P nanofibers have been transferred to. The SiO_x layer is 300 nm thick and the electrical testing has caused dielectric breakdown at the edge.

of the electrode edge coverage. This involves a method to confidently asses the buried edge coverage; focussed ion-beam assisted tomography in an SEM could be a viable method to probe the sample anatomy.

The prospect of a successful development of this method was considered beyond the time frame of this project and therefore the experiments on this method was ended.

4.4 Chapter summary

Three different approaches to realize the basic design of a top contacted OLED were attempted. Each method has different issues making them either unsuitable for the task or simply too time consuming to develop sufficiently within this project. The most important fabrication parameter is control of the oxide coverage at the electrode edges. Partial oxidation of a well defined electrode seems to offer the best control, however using wet processes tend to detach Al from mica so better electrode adhesion is necessary. Applying a separator layer on top of the Al electrode by PVD can be a way to avoid damage to the Al electrode but fabrication is more difficult to control.

There are many ways to solve the issues and also different alternatives on how to realize the desired structure of fig. 4.2. Thick Al_2O_3 can be formed in

other ways than anodic oxidation[90, 91], and the prospect of reactive Al_2O_3 deposition is worth to consider.

Chapter 5

Graphene electrodes

In this chapter initial investigations of the possibilities of using graphene as an electrode material are described. Two test cases were selected; as source- and drain electrodes in OFETs and as electrodes for dielectrophoresis. Both studies used the same lithography process. As an unexpected side-effect hetero-epitaxial growth of organic molecular crystals on graphene and graphitic substrates was discovered, see sec. 5.2.

5.1 Bottom contacted OFET

This section describes my work on using thin graphite and graphene flakes as electrode material in OFETs. There are primarily four different properties that make graphene interesting as an electrode material for electronic devices:

- Being only a single layer of atoms graphene is *the* thinnest electrode material possible to make that is stable at ambient conditions. An electrode edge only one atomic step high will induce virtually no perturbation of the interfaced material.
- This also makes it the sharpest possible 2D edge of any electrode material and thus it should have the highest field enhancement factor possible, to lower the charge carrier injection barrier (previously demonstrated with CNT electrodes for OFETs[92], CNT-FETs[93] and field emission devices[94]).
- The work function of graphene is 0.3 eV lower than graphite, i.e. approximately $4.3 - 4.6$ eV[1][96]. This is comparable to that of Ti and Al, 4.3 eV[65]. This could make it a suitable electron injector in high electron affinity organic semiconductors.
- A single layer of graphene absorbs 2.3% of white light[32] which makes it interesting for use as a transparent electrode e.g. in display technologies.
- Graphitic electrodes are chemically and mechanically very stable. They do not readily form an oxide layer and the material is immobile; it does

[1] Different sources do not agree on the work function of graphite. Takahashi et al. measure ∼4.6 eV[95], while Michaelson find 5.0 eV[65].

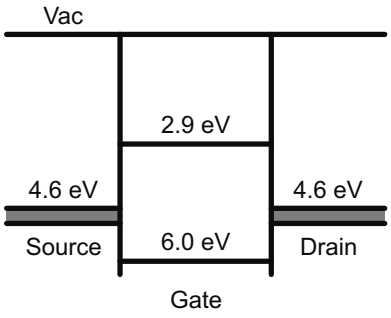

Figure 5.1: Simplified Mott-Schottky energy scheme of an unbiased graphite electrode OFET with *p*6P semiconductor. The presumed band bending of the *p*6P HOMO and LUMO levels due to offset between contact work function and *p*6P chemical potential around 4.5 eV is neglected for simplicity. The range of reported graphite work functions (4.6 eV[95] and 5.0 eV[65]) is illustrated here, but omitted in later illustrations for simplicity. *p*6P energy levels are from[63].

not spread out by diffusion as some materials tend to e.g. during PVD[97] or during operation[98].

In this study I seek to investigate if the field enhancement and lower work function of a few-layer graphene electrode enable electron injection in a *p*6P based OFET. Graphite has a work function of ∼4.6 eV[95] to 5.0 eV[65] and thin graphite electrodes are used for comparison to have as comparable a reference as possible. The OFETs can conveniently be made with a bottom contact design due to the chemical inertness of the graphitic electrodes. Metal electrodes of e.g. Al would readily form an oxide layer if transported at ambient conditions before the semiconductor deposition.

In a first approximation the simple Mott-Schottky model is used for the energy scheme of the device as shown in fig. 5.1. From this simple energy scheme ambipolar operation seems possible but depending on the graphite work function the p-channel may be favored.

The most practical way to realize the device was in a bottom gate, bottom contact layout, as shown in fig. 2.3a pp. 11. A 90 nm SiO_2 gate insulator was chosen to maximize graphene visibility[33]. It was grown in a dry thermal process to obtain the best oxide quality. Heavily n-doped Si substrates were used as convenient backgate electrode. To ensure that the gate potential is controlling charge concentration in the channel, the device length is designed much larger than the gate oxide thickness[49]. A channel length of 1 µm is chosen which is convenient for optical microscopy inspection of the templates while still short enough to ensure reasonably low operational voltages.

Firstly, a fabrication technique compatible with the equipment available at DTU was developed, secondly devices were tested.

Electrical testing and results thereof were thoroughly discussed with Jakob Kjelstrup-Hansen.

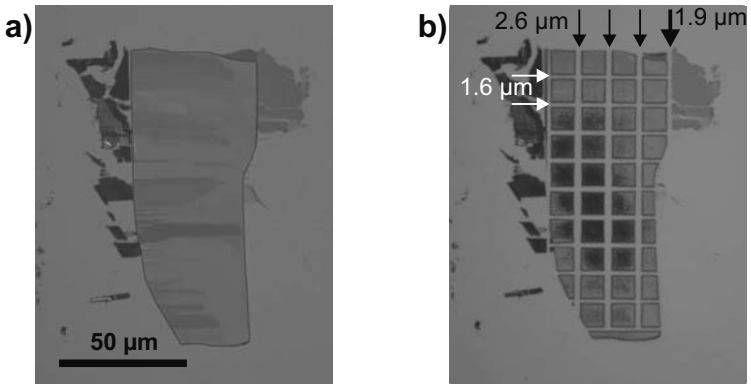

Figure 5.2: Optical microscope images of a thin graphite flake with a bi-layer graphene part before (a) and after (b) patterning by E-beam lithography. The SiO_2 thickness is 90 nm. The vertical design pitch was 11 µm (10+1 µm) and the horizontal 12 µm (10+2 µm). Due to E-beam overexposure the final gap sizes are bigger than designed as indicated in image b (designed 1.0 µm gaps became 1.6 and 1.9 µm, designed 2.0 µm gaps became 2.6 µm). Notice the excellent alignment of the lithography mask to create a gap between the thin graphite electrodes to the bi-layer graphene part (indicated with bold arrow).

5.1.1 Fabrication

This subsection discusses key parts of the fabrication process; the final developed process recipe is described in detail in app. F.

The graphene fabrication technique is based on the micro-mechanical cleavage of natural graphite flakes[37] as introduced at DTU by Timothy John Booth. This produce scattered graphite flakes of different size and thickness, some of which can be single or few layers of graphene. The typical size of graphene flakes range up to tenths of microns across, but is very dependent on preparation. The aim was to maximize the number of fabricated devices to get optimum basis for statistical interpretation. Furthermore the amount of processing should be minimized to increase yield. The latter was accomplished by using mobile electrical multi-point probes developed at DTU to contact the graphitic[2] electrodes instead of lithographically defined metal connections (see details of the measurement setup in app. C.2 and section 5.1.2). To fabricate as many devices as possible from each graphitic flake an array of squares was chosen[3], see fig. 5.2. The gap between each square electrode constitutes a device channel. In a first approximation it is assumed that semiconductor material in the neighboring gaps only contribute negligibly to the conduction.

Electron-beam lithography was chosen over photolithography for two reasons: the pattern can precisely be adapted to and placed on each graphitic flake. Secondly future designs with nanometer-scale features would be possible. However, using the E-beam lithography system at DTU Danchip demanded en-

[2]Both graphene and graphite flakes were tested as electrode material. These are commonly referred to as graphitic.

[3]Device density could be improved by using an array of equilateral triangles, however, that would complicate placement of the measurement probes.

capsulation of all graphite dust particles inevitably produced on the sample in the graphene production process. The graphite exfoliation technique produces both flakes that stick flat on the surface, but also flakes partly sticking out. The latter ones are prone to detach thus being a risk for sensitive equipment, such as the precise mechanical stage in DTU Danchips E-beam lithography system. A special technique was developed for this which included covering the wafer in 10 µm thick photo resist to embed all particles. The E-beam would be scattered substantially through this layer so white light from an optical microscope was used to expose the photo resist at the graphitic flakes to be lithographically patterned. Thus the protecting photo resist could be selectively removed in areas of interest before E-beam exposure - see further details in app. F.

The pattern defined in ZEP resist was transferred to the graphitic flakes by oxygen reactive ion etching (RIE). After lithographic processing the OFETs were finished by depositing a thin film of *p*6P on the substrates.

5.1.2 Electrical characterization

Two batches of samples were made. In the first a 78 nm thick layer of *p*6P was deposited, which turned out to be difficult to penetrate with the measurement probes. Thus only 10 nm was deposited on the second batch. However, optical microscope inspection of the first batch revealed that the *p*6P layer formed ordered domains only on the graphitic flakes, not on the SiO_2 substrate. This discovery led to an extensive study of the phenomenon and is the topic of section 5.2.

In this section electrical testing and measurement results from the second batch samples are presented and discussed.

To perform electrical characterization of the OFET samples the systems described in app. C.2 and C.2.1 were used. To establish proper electrical contact to the graphitic electrode pads it was necessary to scratch through the layer of *p*6P. This was accomplished by using another microprobe (fig. 5.3a) and it was easy to remove the *p*6P layer without destroying even the few-layer graphene electrodes, due to the low spring constant of the cantilever probe. To ensure the measurement probes had proper contact, at least two pins were engaged on each graphitic pad; a resistance below 10 kΩ between the two pins was used to check that pins had proper contact. Probes engaged in a typical measurement situation is shown in fig. 5.3b.

Standard OFET characterization was carried out on multiple devices by following the 2008 IEEE 1620 standard[99] as closely as feasible[4]. It is recommended to initially test gate leakage in order to ensure integrity of the measured source-drain currents. Leakage tests were conducted on graphene electrode templates without a *p*6P layer. No gate leakage was found in the range of $V_g \pm 25$ V and no source-drain current could be measured in the range $V_d \pm 25$ V. However, gate-source leakage tests on a *p*6P OFET made on the same wafer substrate showed leakage at V_g beyond -20 V, (but for unknown reason no leakage at V_g +25 V). Electrical breakdown of the 90 nm SiO_2 should ideally be close to 55 V[62]. The reason for the poor gate oxide behavior, and

[4]Voltage sweeps are performed by typically stepping 100 mV at a rate of 10 steps/s, but no delay was inserted to remove the minor influence from step transients. At large voltage steps e.g. of the gate potential a pause of several seconds was used to relax the device into a steady state before starting the voltage sweep.

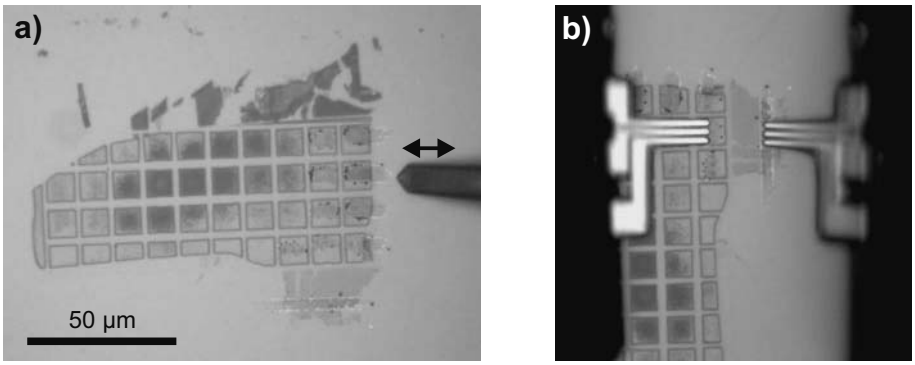

Figure 5.3: Preparation (a) and measurement (b) situation for an array of *p*6P OFETs with graphitic electrodes. To ensure good electrical contact of the measurement probes engaged in b), the *p*6P layer must be removed. This is done by scraping the electrode pads with a flexible cantilever shown in a).

why it differed on the two samples, was not investigated[5]. However a general study by Viswanathan[100] on plasma induced damage of oxide layers suggests that the plasma processing steps in the template fabrication could be the cause. To avoid the gate leakage to influence OFET characterization, measurements were typically conducted with gate biasing up to 15 V only.

Two types of OFET measurements were conducted; output characteristics, I_s vs. V_d at different gate voltages, and transfer characteristics, I_s vs. V_g at different drain voltages. In order to avoid charging effects from only sweeping the voltage in one direction, sweeps were generally made symmetric around zero volt[99, 101]. To avoid transients from large voltage steps, measurements were starting and ending at zero voltage e.g. with the sequence: $0\text{ V} \rightarrow -V_d \rightarrow +V_d \rightarrow 0\text{ V}$. Figure 5.4 show representative measurements on an OFET with graphite source and bi-layer graphene drain electrode. In a normal n-channel FET the characteristic shown in fig. 5.4a would at low positive voltages be linearly increasing (the linear regime) and at higher voltage enter the saturation regime where current is constant for small contact resistances, and sloped for significant contact resistance (see fig. 5.4c). The observed characteristic, where initially no measurable current is flowing followed by a super-linear current increase, is typical in devices with a high contact resistance[49].

Although the energy scheme shown in the inset of fig. 5.4c is comparable to that of the graphitic electrode devices, see fig. 5.5a, the characteristics are evidently quite different. As discussed in the following two subsections there are mainly two factors that differentiate the devices[49]: The OFET of fig. 5.4c+e first of all has much lower contact resistance because the source and drain electrodes are on the opposite side of the semiconductor with respect to the gate electrode. Secondly the gate dielectric is PMMA, which has much fewer charge carrier traps compared to SiO_2, and thus causes much smaller hysteresis.

[5]Open circuit testing of the measurement setup where measurement probes are not engaged on the sample show no leakage even at V_g and V_d potentials of 100 V.

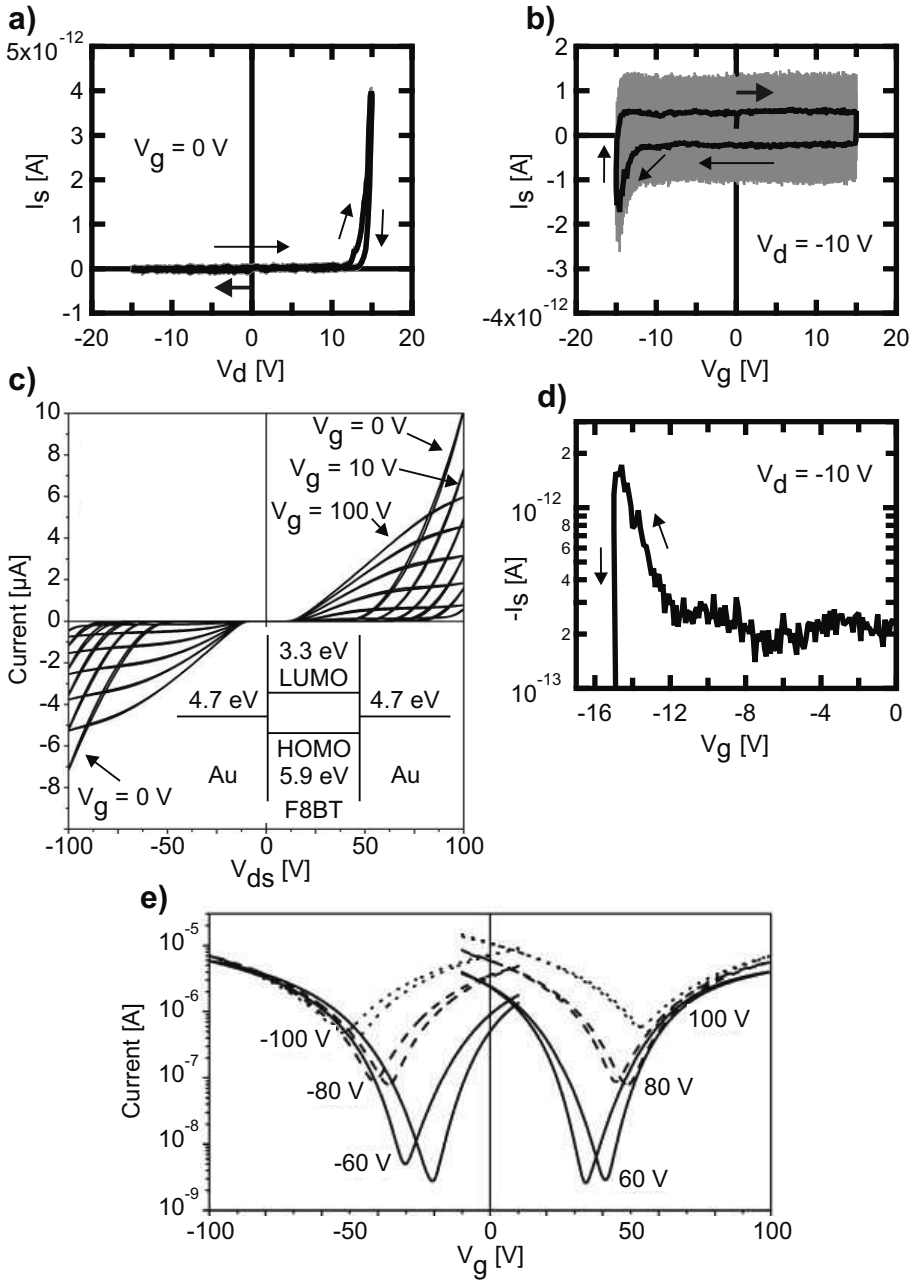

Figure 5.4: Measured OFET characteristics of the device with probes engaged in fig. 5.3b (source electrode is graphite while drain is bi-layer graphene). Normal ambipolar OFET characteristics are included for comparison. a) I_s vs. V_d at $V_g = 0$ V. Bold arrow indicate start of measurement loop. b) I_s vs. V_g at V_d = -10 V. Gray lines indicate standard deviation of samples in each measurement point in a) and b). (The much larger standard deviation amplitude in b) is due to a lower sensitivity range of the current amplifier). d) 3rd quadrant part of the current response i b) in a conventional logarithmic plot. c) and e) current vs. V_{ds} and current vs. V_g, respectively, of a top-gated ambipolar OFET based on F8BT semiconductor and PMMA dielectric ($L = 10$ µm, $W = 5$ mm). c) and e) are adapted from [49]. Measurements in a), b) and d) are conducted under a flow of dry nitrogen and without microscope light exposure ($L = 1.9$ µm, $W = 10$ µm).

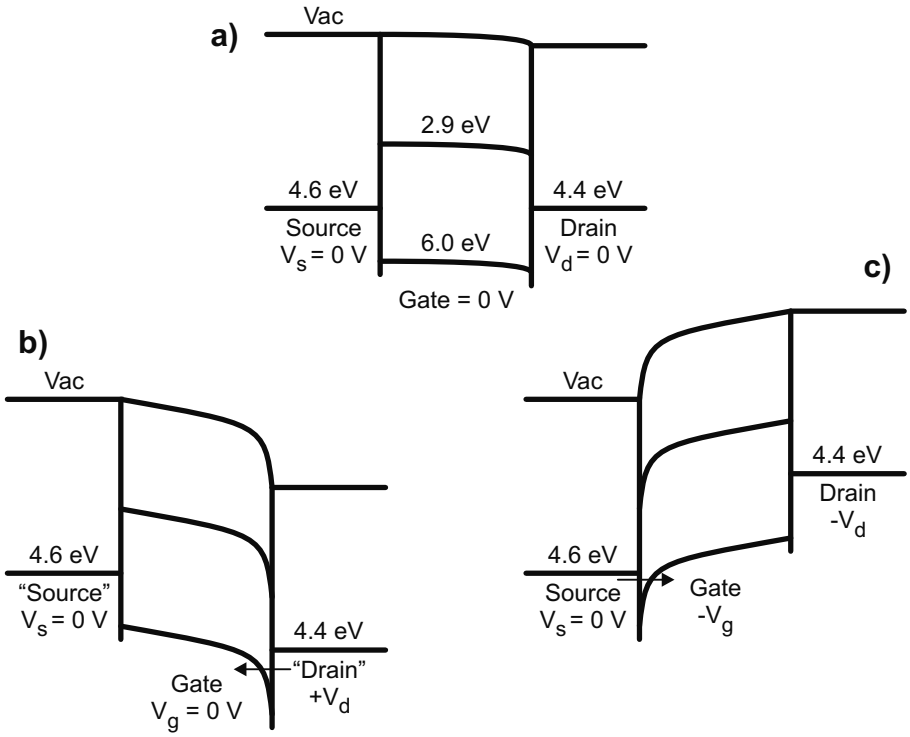

Figure 5.5: Simplified Mott-Schottky energy schemes at different biases. Left hand side electrode is graphite, while right hand side is few-layer graphene. a) Zero bias scheme. b) $V_s = V_g = 0$ V and $+V_d$; the left electrode does not experience any gating, while the *p*6P energy bands bend significantly at the right electrode due to the V_{gd} voltage. Holes are thereby injected from the right—source and drain electrodes are effectively switched. c) The $-V_d$ $-V_g$ bias situation is the conventional p-channel conduction scheme. Drain and gate potentials are comparable, whereas the V_g voltage (referenced to the source) causes significant band bending at the source electrode thus thinning the barrier for hole injection.

Injection limited conduction

The gate sweep in fig. 5.4b shows evidence of p-channel behavior but no n-channel conduction. This makes the current response at $+V_d$ in fig. 5.4a somewhat counter intuitive if the source is unable to inject electrons. The observations can however be understood by an energy scheme where significant interface barriers govern device characteristics. Consider the simplified[6] energy diagrams of fig. 5.5. In scheme b, when the right electrode is positively biased a current can only flow if electrons are injected from the left or holes are injected from the right. Because the left potential equals that of the

[6]The assumptions made to this representation is a simple Mott-Schottky model, where the barrier height is given by the difference in energy levels. Thereby interface dipoles are not considered. For simplicity the gate offset due to the difference in work function of source and drain electrodes relative to the gate electrode is considered insignificant.

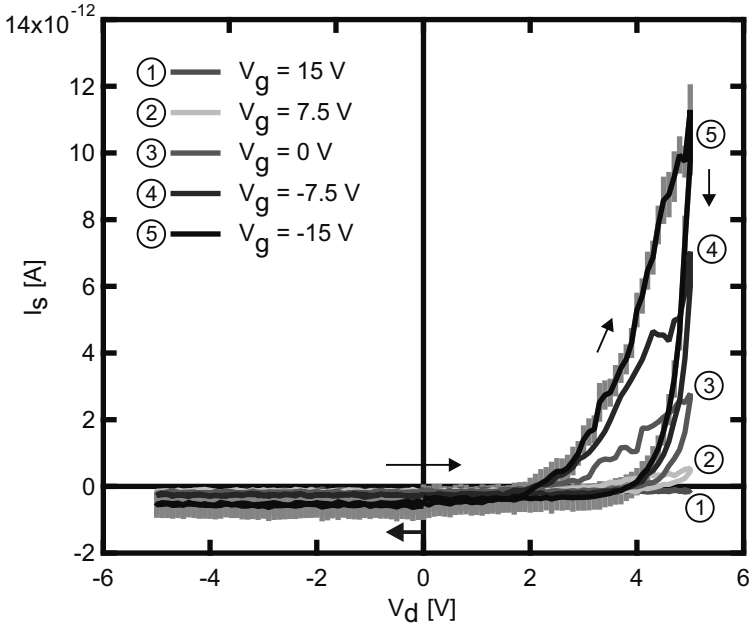

Figure 5.6: I_s vs. V_d characteristics at different gate potentials of a thin graphite electrode OFET ($L = 1.4$ µm $W = 10$ µm). Measurements are conducted under a flow of dry nitrogen and with the microscope light on. The course of the measurement loops starts at the bold arrow.

gate, no gate induced band bending occurs at the left electrode and the electron injection barrier remains high. However, the right electrode is positively biased relative to the gate causing the bands to bend at the right electrode. This results in a lowering of the hole injection barrier and consequently the conventional "drain" electrode becomes a source of hole charge carriers injecting into the device. The current increases in a super-linear form which can be attributed to the exponential characteristics of typical barrier crossing phenomena, such as field enhanced thermionic emission and Fowler-Nordheim field emission. Plotted on a semi-logarithmic scale, fig. 5.4d, the linear characteristic further supports this. Similar schemes of contact limited conduction have been reported for FETs with a CNT as the semiconducting element[102]. The hypothesis of injection limited conduction is further supported by measurements of I_s vs. V_d at different gate potentials; at higher positive gate potentials conductance is retarded, while it is enhanced at increasing negative gate potentials. Compare fig. 5.6 with fig. 5.4c. Within this picture, had the left electrode in fig. 5.5b been the source (of electrons), the response would have been that of a typical transistor, and conductance increased with positive gate potential. Indeed a shift from injection limited to the normal channel limited regime is observed in characteristics of fig. 5.4c upon increasing gate voltages.

When V_d is biased negatively and V_g is swept negatively the device is in a conventional p-channel regime. In fig. 5.4b a weak response is observed. This correspond to the scheme shown in fig. 5.5c; the source-drain field only allows holes injected from the left or electrons injected from the right electrode to

pass through the device. When the gate bias is highly negative the potential difference is largest at the left electrode and here the energy bands bend the most. Thus the barrier to hole injection from the source electrode is lowered and beyond a threshold bias a measurable current flows. This is the conventional biasing region of p-channel device characterization, whether it being injection or channel limited conduction (similarly $+V_{\mathrm{d}}$ and $+V_{\mathrm{g}}$ is the conventional n-channel biasing region). It is worth to compare the schemes in fig. 5.5b and c for a thorough understanding of the observed device characteristics. Scheme b is conceptually a mirror image of scheme c and as described above the only difference is which electrode is injecting holes. In other words the current response observed in the characteristics in fig. 5.4a and b stems from the same injection mechanism but on opposite electrodes and probed in slightly different ways.

High contact resistance renders the device of little use. It cannot be used as a normal transistor since it does not exhibit characteristic operation governed by a conducting channel formed at the dielectric/semiconductor interface. For the same reason the equations commonly used to describe the different FET operating regimes are not applicable and OFET parameters such as on/off ratio and charge carrier mobility cannot be extracted by the conventional methods[49].

Measurement hysteresis

The measured characteristics in fig. 5.4a and b show a clear difference in the forward and reverse sweep i.e. hysteresis behavior. In both cases a lower current is observed when sweeping back from the maximum voltage towards 0 V.

As comprehensively described by Egginger et al.[101], hysteresis phenomena observed in normal operating OFETs (i.e. limited by channel resistance) can be attributed to either trapping of charges, so they cannot contribute to the current, or to passivation of the gate potential by charges in the gate dielectric. Compensation of all these effects are included in the concept of threshold gate voltage. Thus the effective gate potential is the applied voltage minus V_{t}. In normal (O)FETs V_{t} is constant throughout the operational range. If the characteristics show hysteresis it can be attributed to a change in V_{t} which hinders rigid transistor characterization[49].

Different effects result in higher or lower back sweep current of the hysteresis loop and a thorough analysis of the different schemes can exclude many of the effects described by Egginger[101] for the system in consideration. Although the effects are generally thought to be spread throughout the channel of the OFET, I propose that the same phenomena conceptually can be used to describe device operation when characteristics are governed by contact effects. Based on the following arguments the simplest scheme to explain the observed characteristics is considered to be filling of hole traps during measurements. Consider for example the scheme in fig. 5.5c: when positive charge carriers are injected into the semiconductor and some of them are trapped close to the interface, it will cause the bands to bend downwards and thereby increase the injection barrier. When the voltage is swept back towards zero the temporarily higher barrier is clearly expressed by a lower conduction. A similar behavior is observed by Santato et al.[103] who describe it as a linear increase of V_{t}.

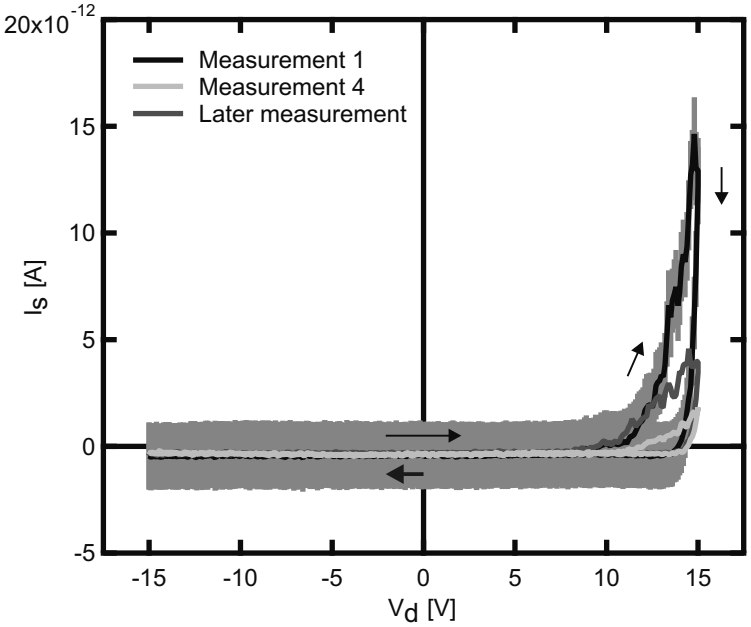

Figure 5.7: I_s vs. V_d characteristics from a series of measurements on a thin graphite electrode OFET. From the first measurement conductance significantly reduces to the relatively steady state response of measurement 4. The characteristic measured after the device had been idle for a few minutes shows it had regained to a state of higher conductance than measurement 4. The course of the measurement loops are indicated starting at the bold arrow. The gray bars indicate the standard deviation of measurement 1. Measurements are conducted under a flow of dry nitrogen and no illumination from the microscope.

The hypothesis is supported by the following observations: when I_s vs. V_d characteristics are measured repeatedly, following sweeps typically show poorer conduction. Moreover, a pause in measurements caused the device to regain conductivity as illustrated in fig. 5.7. The same behavior of repeated measurements showing a lower conductance until a saturation was reached, is reported by Chua et al.[104] in n-channel devices.

The general conception in literature is that SiO_2 has a large amount of electron traps at the semiconductor interface mainly due to absorbed water that has split into OH groups[104]. In principle the measured characteristics could also be explained by a large amount of trapped electrons which changes a little during measurements; "hole trapping" would then correspond to a small decrease in the amount of trapped electrons. To solve the issues that limit proper device operation one must of course keep this possibility in mind. However, even if the behavior is due to large electron trapping, the picture of moderate hole trapping still *conceptually* describes the device behavior[7]. And even if we cannot determine the polarity of the traps, the conclusion is still

[7]And one may argue that it is reasonable to use the simplest explanation until new observations can be used to refine the description (Occam's razor).

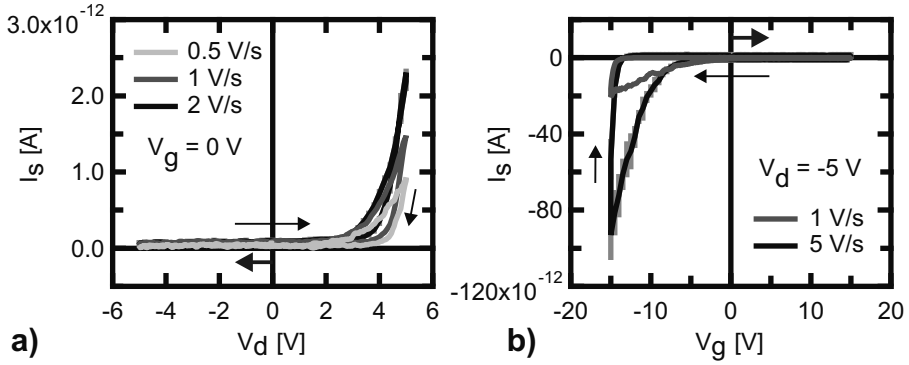

Figure 5.8: I_s vs. V_d and I_s vs. V_g characteristics of a thin graphite electrode OFET. Measurements are conducted under a flow of dry nitrogen and with the microscope light on (the latter causing a somewhat higher current response). $L = 1.4$ µm $W = 10$ µm. Gray bars have been added in one measurement on each graph to indicate the standard deviation. The direction of hysteresis loops are indicated starting with the bold arrows.

that the system must be improved to avoid any kind of charge trapping or gate neutralizing effects from the dielectric, and thereby avoid the hysteresis.

Hysteresis is a key element in memory devices, where a pronounced and stable hysteresis is needed. Alternatively the system could be optimized for such purposes, however, that is a very different topic from the OFET functionality in focus here.

The effect of measurement speed

The effect of voltage sweeping speed is shown in fig. 5.8. The observed conductivity increase with sweeping speed can be understood in the framework of a trapping latency. This is most easily understood by considering the measurement as a series of small voltage steps. When the voltage is increased one step it takes a short while for the population of trapped carriers to increase and stabilize in accordance with the changed potential scheme. When the sampling time of each small voltage step is comparable to the settling time of the steady state barrier, a higher measurement speed will effectively correspond to a lower injection barrier.

Notice that a displacement current due to capacitive loads in the system would behave in a similar manner, since the displacement current is $I_{\text{disp}} = C\frac{\mathrm{d}V}{\mathrm{d}t}$. However, assuming that permittivity and capacitance are constant, the displacement current would have the same magnitude throughout the sweep and different sign in the two sweep directions. The low or insignificant influence from this effect can be seen directly in the measurements: in the I_s vs. V_d sweeps an offset difference between up and down sweeps is not discernable from the noise. In the I_s vs. V_g sweeps the offset is in the order of 0.5 pA at normal measurement speed (1 V/s) and thus not critically influencing the measurements.

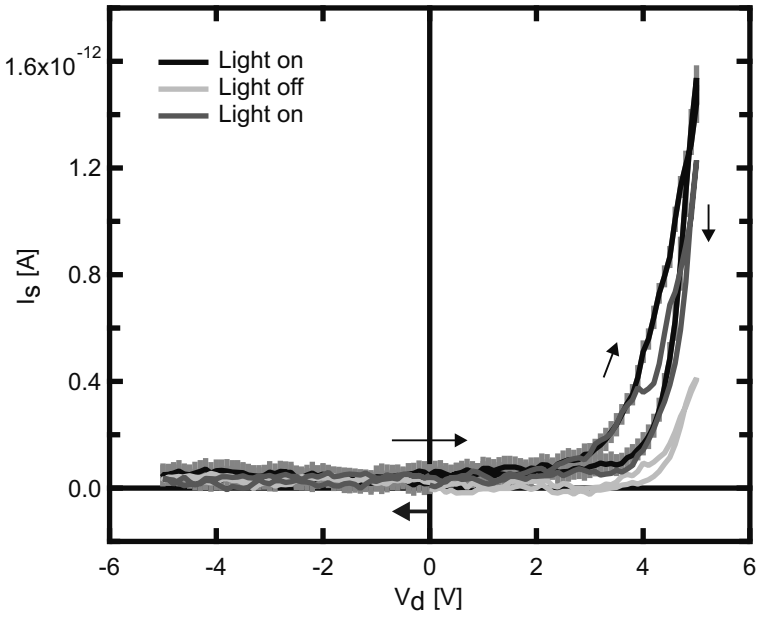

Figure 5.9: I_s vs. V_d characteristics of a thin graphite electrode OFET when sample illumination is first on, then switched off and back on again. Measurements are conducted under a flow of dry nitrogen and with the microscope light on. $L = 1.4$ µm $W = 10$ µm. Gray bars have been added to indicate the standard deviation for the first measurement. The course of the measurement loops are indicated starting with the bold arrow.

The influence of light

The influence of sample illumination by the microscope light during measurement was found to be very significant, as seen in fig. 5.9. (The lower conductance of the third measurement may in part be due to the memory effect illustrated in fig. 5.7). The high response to optical stimulation is an indication that conduction is limited by barriers, either distributed in the device or concentrated at the injection barrier. When device characteristics show signs of photoconductance like this, measurements must be conducted without illumination, to have a common reference with other studies[99].

The influence of atmosphere

Most of the measurements were conducted with a weak flow of dry nitrogen blowing at the sample to keep humidity from the air away. The influence of ambient and humid conditions was investigated by a series of I_s vs. V_d measurements. First a reference measurement was made, the nitrogen was turned off and measurements in ambient were made. Immediately after turning the nitrogen off the conductivity had slightly degraded and only minor change was observed after 5 min without a nitrogen flow (ambient conditions were 19% relative humidity and 24°C). The sample was humidified by breathing which improved the conduction. After reapplying the dry nitrogen flow the onset

voltage vent from ∼16 V down to ∼10 V.

The experiments show that high humidity can shift the characteristics of the device but not readily change the shape. It is not known if the ambient transport of the templates and months of storage of the finished devices before testing have had significant influence on the OFET behavior.

Additional investigations

A few additional experiments were conducted on the *p*6P OFETs which are worth mentioning.

The effect of annealing the sample at 110°C for 1 hour in a nitrogen atmosphere was investigated. The effect was a clear degradation of the device conductivity.

To probe the polarity of charge traps I conducted step response measurements. The transient response of I_s to a large step of V_g can reveal at which gate polarity traps are being charged as described by Gu et al.[105]. However the system was not designed for this purpose; the small device dimensions give a poor signal to noise ratio because the capacitances of the measurement system add to the measured signal.

Electroluminescence from OFETs driven by an AC gate potential has been reported by Yamao et al.[51], and later in *p*6P based OFETs by Kjelstrup-Hansen et al.[52], see sec. 2.1.1 pp. 12. It was investigated if graphitic electrode *p*6P OFETs also could show electroluminescence by application of a symmetric V_s and V_d and a large high frequency AC gate bias. Under similar light detection conditions as used in the successful experiments described in [52] it was however not possible to observe any electroluminescence from the devices in the attempts made.

5.1.3 Evaluation of graphene electrode OFETs

The presence of hysteresis makes rigid transistor characterization virtually impossible due to the non-constant V_t, unless a pulsed measurement principle is used as suggested by Petit et al.[106]. The high and non-linear contact resistance renders the equations governing normal transistor operation unusable. I consider these issues the most important to address if proper evaluation of a graphene electrode OFET is to be made. Several possible ways to improve the system are described in literature:

- Use another gate dielectric to avoid charge traps and hysteresis[104].
- Put gate and source-drain on opposite sides of the semiconductor to lower contact resistance. This requires another device design e.g. using a top gate[49, 107].
- Use a different organic semiconductor to lower injection barriers. Either with a smaller band gap for an ambipolar design or lower LUMO level for an n-channel device.

The effect of samples being exposed to ambient conditions has not been thoroughly investigated. However, the effect of water inevitably being absorbed in the SiO_2 prior to depositing the *p*6P thin film is considered to have

a major impact. A complete fabrication process and testing under inert conditions would make device fabrication much more cumbersome and encapsulation should be considered as an alternative.

Solving the dominating issues of hysteresis and high contact resistance would enable investigation of the really interesting features of the system; does the use of inert electrodes lead to better device stability? And can graphene improve charge injection over graphite electrodes? The research described in this chapter is only the first start. The major issues have been elucidated and solutions proposed.

It should be noted that two other publications[108, 30] on the use of graphene as electrode material in OFETs became available at the same time this work was published. To the best of my knowledge no prior studies have been reported on this specific application and thus its research can be considered to be in its infancy.

5.2 Graphene as nanofiber growth substrate

During the graphitic electrode OFET experiments described in section 5.1 a peculiar discovery was made. In the batch of samples where 78 nm of *p*6P had been deposited, the molecules formed crystalline domains on the graphene and graphite flakes. On the SiO_2 substrate no such ordered texture could be seen in the optical microscope. Growth of crystalline thin films and aggregates of *p*6P is thoroughly described on other substrates so it was very appropriate to investigate the phenomenon further. This section describes the result of various characterization methods applied, from which several conclusions can be drawn.

The following two subsections first describe the analytical methods used, and then put the results together to elucidate the observed correspondence between molecular orientations, morphology and substrate lattice.

5.2.1 Analytical methods

To characterize molecular crystals of *p*6P two properties are of major interest: molecular orientation and morphology. These are probed with optical and AFM or SEM techniques respectively.

Probing the molecular orientation rest upon the transition dipole moment of the HOMO-LUMO being oriented along the long axis of the *p*6P molecule[17, 25]. Thus it is possible to probe the molecular orientation by detecting the polarization of fluorescent light.

*p*6P molecules ordered in a molecular crystal typically arrange in a herringbone structure (β-phase) where all molecular axes are parallel[22]. This is very useful for the characterization of such crystals due to the simple polarization of the fluorescence. When a polarization filter is placed in front of the camera the intensity of polarized fluorescence from the crystalline domains are described by Malus' law: $I = I_0 \cos^2 \theta$. Here θ is the polarization of the light relative to the filter. Thus molecular orientations within different domains on a sample can be characterized by using a fluorescence microscope in the following way. The sample is placed on a rotational stage and fluorescence images are recorded

for 360° sample rotation[8]. The images are then rotated and aligned to each other in a stack and analyzed with image processing software. In this case ImageJ[9] was used. Because the fluorescence intensity is sinusoidal a Fourier transformation can be utilized to filter noise components not having two periods in the 360° rotation. This is implemented in an ImageJ plug-in by Frank Balzer comprising the following routine: An FFT is used to analyze the intensity variation of each pixel through the image stack virtually representing 360° rotation of the polarization filter. From this the power of the second Fourier component, $\gamma = 2$, and its phase is extracted[10]. The power (i.e. intensity of the emitted fluorescence) is plotted in a separate image, and the phase of the signals as well. The latter is a direct measurement of the molecular orientation. Several samples have been analyzed this way, an example of which is shown in fig. 5.10. As evident from the histogram of the phase image, fig. 5.10e, there are six pronounced orientations of molecules on the sample. Notice the absence of fluorescence from the areas of the SiO_2 substrate surrounding the flake in fig. 5.10b. This strongly suggests that *p*6P molecules are standing upright on the SiO_2 in contrast to a horizontal orientation on the graphite flake. *p*6P molecules standing upright on SiO_2 was also observed by Koch et al.[63].

The sample also show a strong polarization of the reflected white light. To investigate how this relates to the molecular orientations white light was used instead of fluorescence. This led to the discovery that reflected blue light carry the exact same polarization as the fluorescence, while the green and red reflectance is highly dependent on graphite flake thickness, see fig. 5.11. This is a very useful property for the characterization of these samples; UV-excitation, and thereby sample bleaching can be avoided completely.

To probe the sample morphology AFM and SEM techniques were used. These complement each other quite well due to the high Z-resolution of the former and high XY-resolution of the latter. AFM was mainly used to determine the exact thicknesses of the graphite flakes and deposited *p*6P thin films. SEM reveals minute details of the surface morphology as shown on two different samples in fig. 5.12. The domain morphology is evidently different on the two samples. In 5.12a+c the thin film is almost continuous having only long trenches that constitute the characteristic orientation of the morphology. In 5.12b the *p*6P molecules have assembled into small nanofiber-like aggregates with typical dimensions of 500×20 nm^2. Performing the optical analysis on samples like the one in fig. 5.12b reveals a pronounced alignment of the molecules, however not as strong as on samples like that of fig. 5.12a (from the first batch). As noted in the figure caption, several experimental parameters were different. A mapping of the full parameter space would be necessary to properly understand what conditions lead to either type of domain formation. This is however beyond the scope of this project, which I have limited to a basic characterization of the two types of domains.

To further investigate the physics behind the polarized reflection of white light, spectral reflectance measurements were conducted. Using a spectrometer

[8]It is preferable to rotate the sample instead of the polarization filter due to the inherent weak partial polarization through the microscope optics. Rotating the sample keep errors from the microscope constant throughout the measurement.

[9]ImageJ is public domain Java-based software provided by the U.S. National Institutes of Health, see http://rsbweb.nih.gov/ij/.

[10]A similar analysis is described in detail by Bernchou et al.[109].

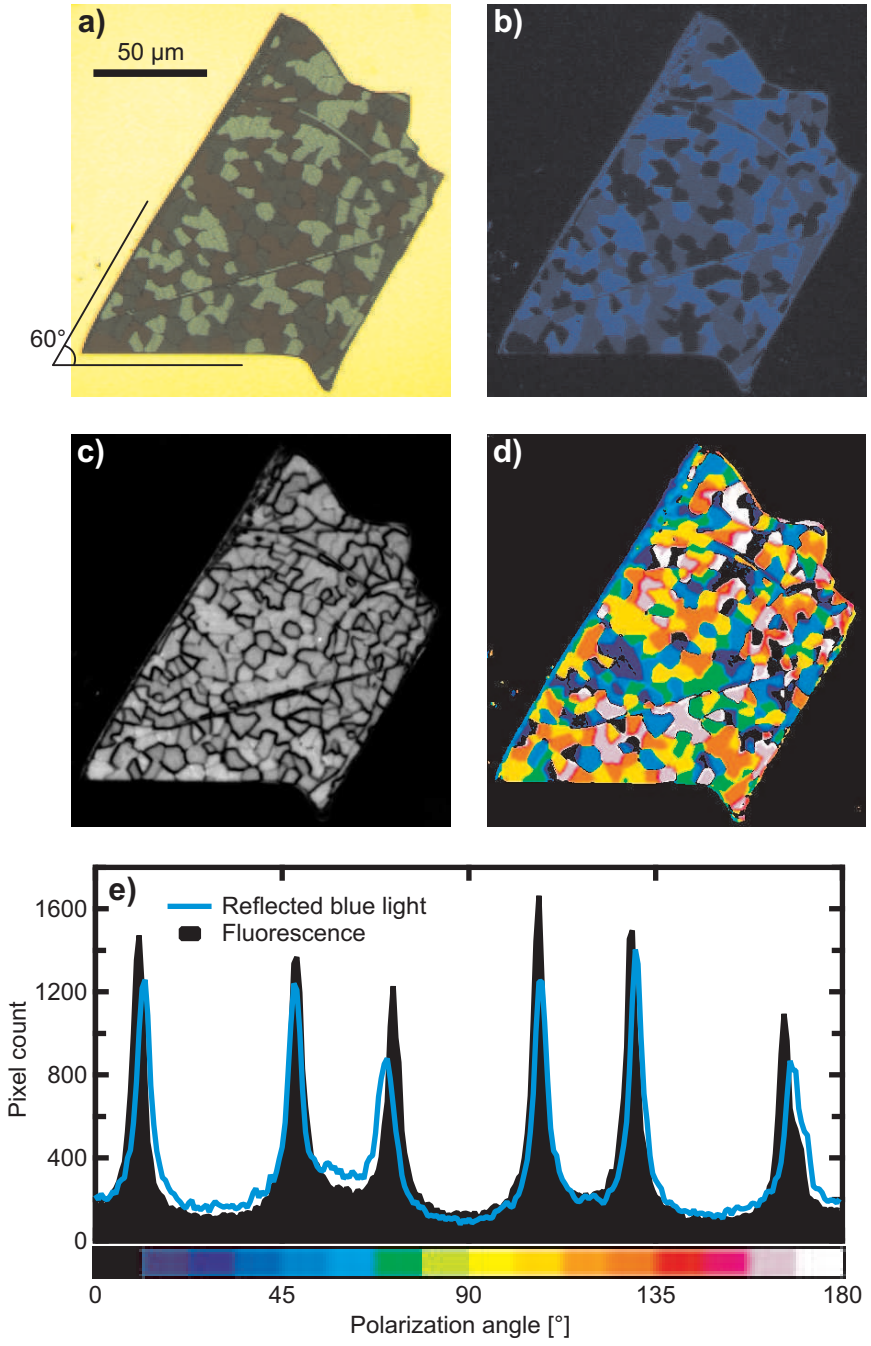

Figure 5.10: Analysis of the ordering of *p*6P molecules on a thin graphite flake. a) Optical microscope white light image (with polarization filter). The characteristic 60° angle of the graphite lattice is indicated. b) Fluorescence image (with polarization filter). c) Power of the Fourier component $\gamma = 2$ in the analysis of the fluorescence intensity vs. polarization angle. d) Angle of peak fluorescence (i.e. molecular orientation) indicated by color. e) Histogram of c) indicating the number of pixels vs. molecular orientation. The black histogram is from the analysis of polarized fluorescence, while the blue graph is the result of the same analysis using the blue part of reflected white light. Pixel size is 0.25 µm^2.

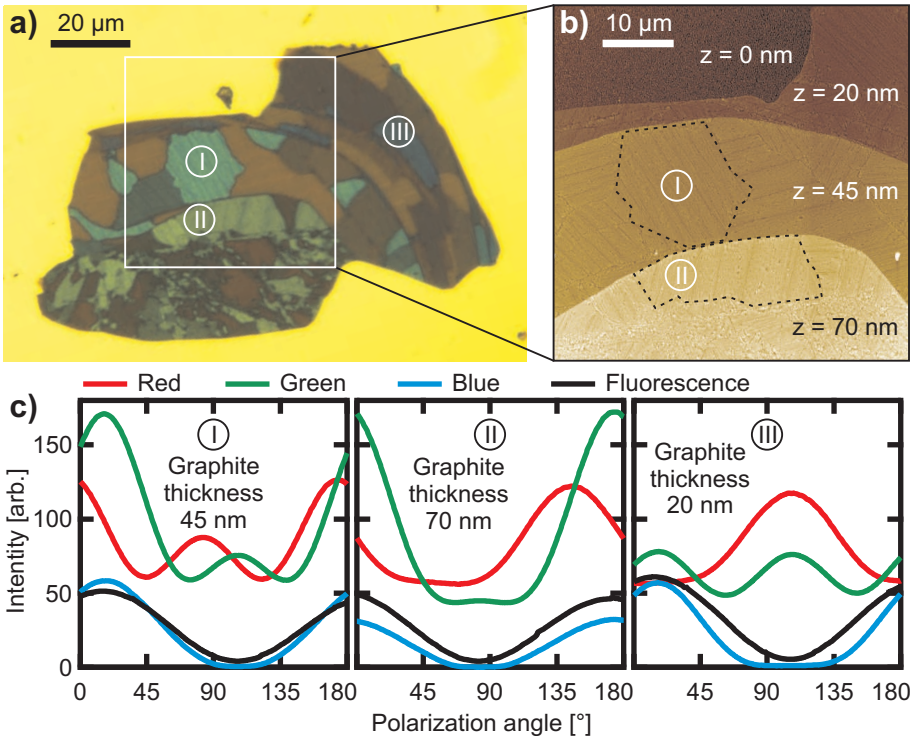

Figure 5.11: Polarization of fluorescence compared to the polarization of the red green and blue colors of white reflected light on a thin graphite flake of different thicknesses. a) Optical microscope white light image (polarized). b) AFM topography image of the area indicated in a). c) Intensity of fluorescence and reflected colors as a function of polarization angle in the three different domains. The teal and blue color of domain I and III, respectively, in a) is a result of the different thicknesses of the graphite flake terraces.

coupled to one of the microscope oculars through a thin optical fiber, a sampling area of only 5 µm in diameter was obtained (using a 50× objective). This is more than sufficient to ensure sampling of light from one domain only. White light reflection spectra were recorded at orientations with the filter parallel and perpendicular to the molecules. While the recorded spectra on a graphite flake without the *p*6P thin film can be perfectly described by using classical optics, the high anisotropy in the formed domains is non-trivial to describe. Modeling of the spectra is undertaken by collaborator Frank Balzer and was a work in progress when this thesis was finalized.

5.2.2 Analysis

Before moving on to analyzing the observed domains, it is important to point out why all domains on a flake with multiple steps in the stack of graphene layers are comparable. The key is that step edges do not change the lattice orientation of natural graphite; the common stacking of graphene layers is of AB type[110], meaning that armchair and zigzag orientations are unchanged

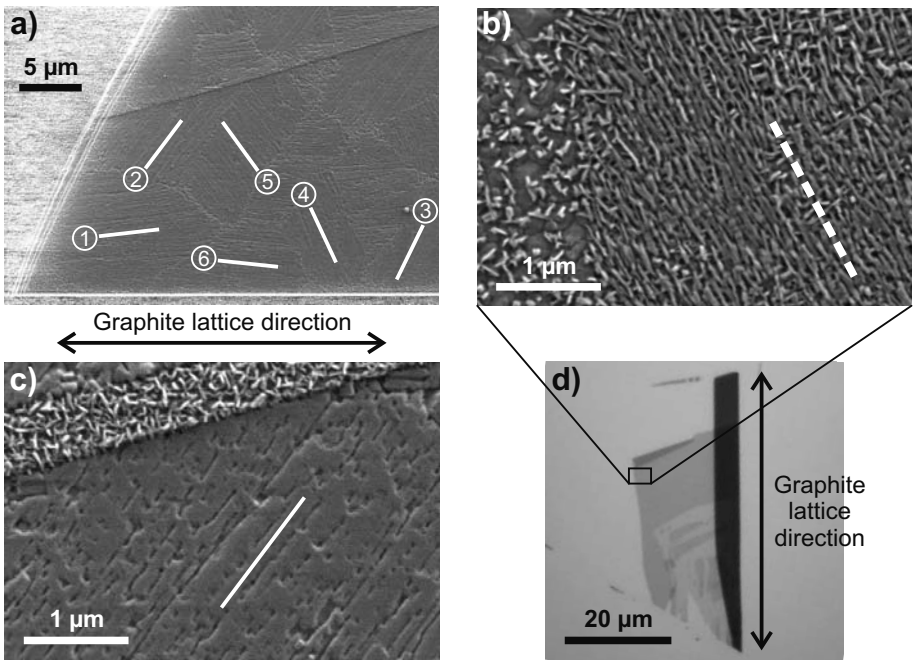

Figure 5.12: Surface structure of crystalline *p*6P domains from two different batches. a) 1 kV SE2 SEM image of the 60° corner of the flake in fig. 5.10a. The six different morphological orientations are indicated with numbered bars. b) 1 kV SE2 SEM image of the nanofiber-like aggregates formed on subsequent batches, here on bi-layer graphene. The left part of b) illustrate the disordered structure of *p*6P on SiO_2 (also observed by Koch et al.[63]). The dashed white line indicate the average morphological orientation. c) Close-up of the sample in a), with the same scale used in b) for direct comparison of the different surface structures. A step edge with disordered molecules intersect the upper part of c). The white line indicate the average morphological orientation. d) Optical microscope image of the sample in b) before *p*6P deposition (substrate is 90 nm SiO_2 on Si support). Parts of the flake is single-layer graphene while the larger part is bi-layer. In all images horizontal and vertical are characteristic graphite lattice orientations (either zigzag or armchair). The nominal *p*6P thickness in a)+c) is 78 nm and 58 nm in b). The sample in a)+c) had been through the lithography process described in app. F, whereas that in b)+d) had no processing before *p*6P deposition. Substrate temperatures during deposition was ∼30°C, but may have differed slightly due to different substrate clamping on the sample holder.

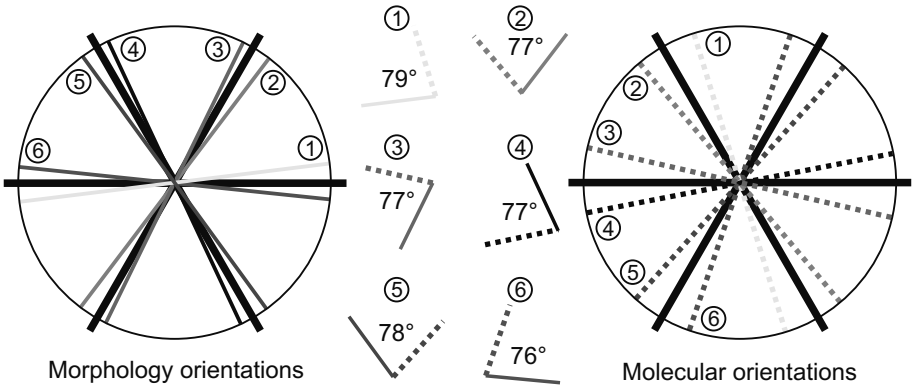

Figure 5.13: Morphological and molecular orientations relative to the graphite lattice in the first sample batch, determined from fig. 5.10 and 5.12a. The average angle between morphological and molecular orientations is 77°. Morphological orientations are on average 6° relative to a specific type of lattice direction, whereas molecular orientations on average are 12° off.

throughout the graphite crystal. Thus domain orientations at different terraces of a graphite flake can be compared directly, as is the case for the flake in fig. 5.11. This is different from muscovite mica substrates, where an odd number of steps in cleavage planes cause a change of orientation by 120°[111].

As pointed out in fig. 5.12 morphologically different domains can form on the graphitic substrates. In the following the two different kinds of samples are analyzed starting with that of fig. 5.12a+c.

In the first batch of samples where domains were observed, they all look as illustrated in fig. 5.10, 5.11 and 5.12a+c. Some graphite flakes, like the one in fig. 5.10, have edges that presumably follow characteristic graphite lattice orientations. This is a useful reference to relate the molecular and morphological orientations to the graphite lattice. When this is done for the sample in fig. 5.10 the symmetry shown in fig. 5.13 emerges. From the experiments made so far it cannot be determined if the graphite lattice orientation is the zigzag or armchair. Distinction of these should be possible through low energy electron diffraction (LEED) which can detect crystallographic details of thin layers, also in very small areas.

The general relation of ∼12° between the molecular and lattice orientations suggests the domains are all of the same kind. When the characteristic lines of the domain morphology is compared to the molecular orientations it is seen that all six domain orientations are alike. The average angle between the molecular and morphological orientations on this batch is 77° (based on two different graphite flakes both showing 77° as the average of their respective domains). This is quite close to the angle of 76° observed in organic nanofibers grown on muscovite mica[15] and within the few degrees uncertainty estimated for the measurements. This correspondence suggests the observed domains also are β-phases of the p6P molecular crystal.

In the following batches, aiming at growing molecular crystals on single- and few-layer graphene flakes, the p6P molecules had only aligned on a smaller number of samples. However, on several samples nanofiber-like aggregates as

shown in fig. 5.12b were found. Analysis of molecular, morphological and lattice orientations was performed on these samples to compare with the first batch. The morphology orientation is somewhat ambiguous in this case, where the general orientation of the longest aggregates has been used. On six domains in three different samples (two bi-layer graphene and one thin graphite), the molecular orientations relative to substrate lattice orientations were on average 4° (ranging from 1° to 6°). In three of these domains (one on bi-layer graphene and two on thin graphite) morphological orientations of the nanofiber-like aggregates could be determined to $86 \pm 1°$ relative to the molecular orientations. The morphological orientations were only $1 \pm 1°$ off a characteristic graphitic lattice orientation. Morphology appeared the same in the subsequent batch (but quite different from that of the first batch). The close lineup with the graphitic lattice orientations suggests a growth according to that of a monolayer of *p*6P on highly oriented pyrolytic graphite (HOPG) reported by Wang et al.[112]. In an STM study they find that *p*6P molecules at $T = 105$ K align their long molecular axis approximately 2° off the armchair lattice direction and columns of parallel molecules to be approximately 4° off the zigzag orientation (and ∼88° between the two). Nanofiber-like aggregates with *p*6P molecules perpendicular to the long fiber axis have previously been reported on TiO_2[113, 19] and KCl[114] substrates. Furthermore crystalline *p*6P structures on metallic surfaces form at a nominal coverage only slightly larger than a monolayer[19]. So it is plausible that the crystalline domains observed here correlate with the findings of Wang et al.[112], however, a more thorough study would be necessary to confirm this[11].

The first batch of samples, where the *p*6P domain formation was discovered, had been through the lithography process described in app. F. This is the most significant difference between the first and subsequent batches, which had not been through any processing before *p*6P deposition. It is possible that a thin layer of resist residue from the processing remained and influenced the epitaxial growth. Evidently the process can be extremely surface sensitive; a single layer of graphene on a SiO_2 surface can make pronounced alignment of flat-lying molecules instead of standing molecules. A future study of the growth properties could for example include investigation of thin overlayers on the graphite substrate, as it has been done with e.g. Au on mica[17].

5.2.3 Evaluation of graphene as growth substrate

Within the experimental work made to grow and characterize the *p*6P molecular crystals formed on graphite and graphene substrates, some key elements have been discovered. First of all it was found that the *p*6P molecular orientation can be probed by measuring the polarized reflectance of blue light. Secondly two different *p*6P crystal phases were found and described in terms of molecular and morphological orientations in relation to the graphitic lattice. To better understand and eventually control the mechanisms behind the formation of the different crystal phases, a thorough mapping of the growth

[11] There are software tools made for calculating commensurability of crystalline interfaces which would be sensible to use. An example of such is the "GRACE" tool, available through the New York University homepage http://www.nyu.edu/fas/dept/chemistry/wardgroup/Software.html.

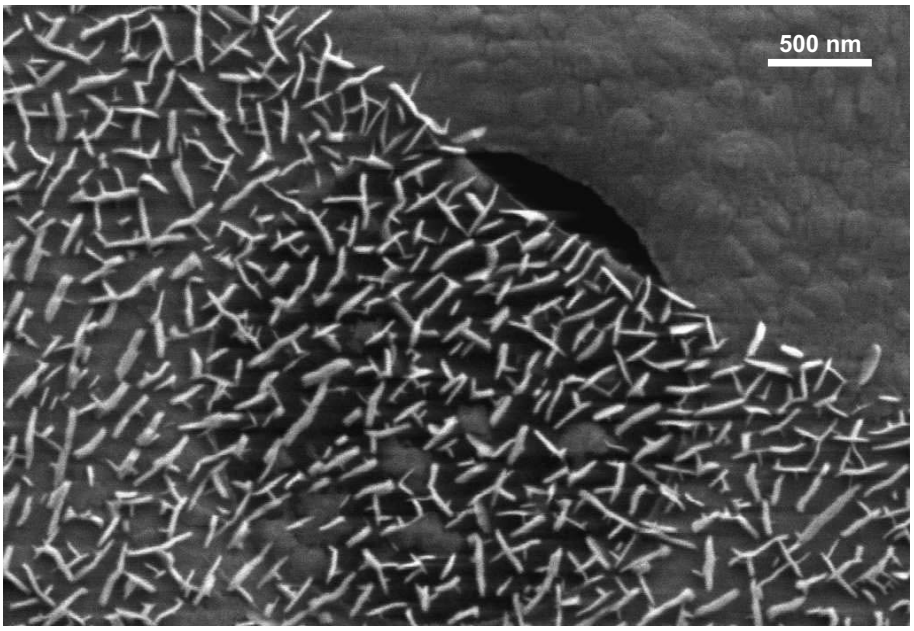

Figure 5.14: 1 kV SE2 SEM image of a graphene flake suspended on a Quantifoil holey carbon grid[43]. Multiple nanoaggregates have grown, although the ordering is less obvious compared to previous samples. Notice the aggregates in the upper part of the image extending up to 100 nm from the edge of the graphene flake. The *p*6P was deposited with 0.02 nm/s up to 10 nm at 2.1E-8 mbar and sample temperature ∼80°C. Sample preparation was done in collaboration with Timothy J. Booth and Jakob Kjelstrup-Hansen.

parameters would be necessary. However, some exciting perspectives of possible uses have already been elucidated. Graphene can be used as an electrode material and possibly crystalline organic nanofibers can be grown to span small gaps. This could either serve as a device directly or be a platform to investigate the electrical properties of the molecular crystal. Based on section 5.1 another oligomer than *p*6P may however be preferred to adjust the energy levels to that of graphene. The most promising perspective is considered to be the use of suspended graphene[42, 43] as a scaffold for molecular crystal studies. The perspectives of growing molecular crystals directly on a highly electron transparent film, enabling direct TEM studies are indeed very intriguing. Initial steps to test this concept was done by depositing *p*6P on suspended graphene, see fig. 5.14.

5.3 Graphene as dielectrophoresis electrodes

Graphitic electrodes for DEP assembly are interesting alternatives to metallic ones for example because they can be made as thin as single layers. This section describes experiments carried out to test the feasibility and shed light on the challenges of using thin graphite and graphene electrodes for DEP. Assembly of CNTs by DEP was chosen due to the numerous literature available

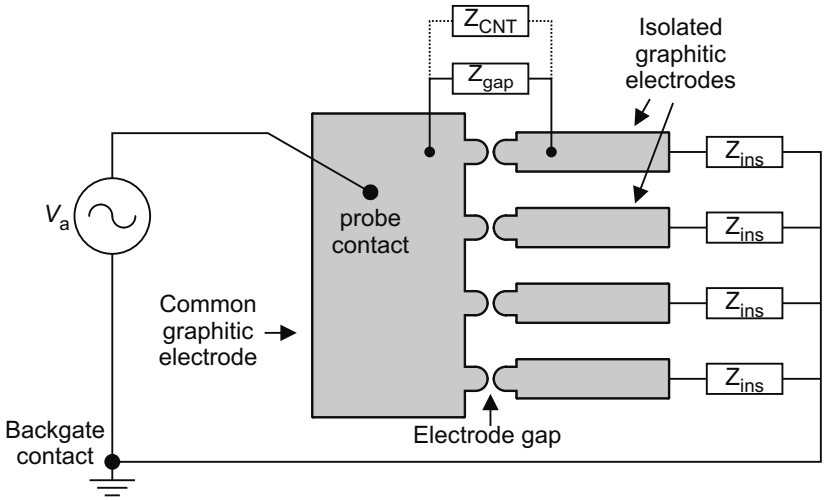

Figure 5.15: Schematic illustration of a DEP experiment where one common and several capacitively coupled electrodes are used. The common electrode is contacted with a physical probe (in this project of the type shown in fig. C.2d pp. 87). Four electrodes capacitively coupled to the backgate are shown, but in principle the number is only limited by the size of the graphite flake. The self-limiting principle allow parallel assembly of CNTs in all gaps in the same DEP experiment.

for comparison, e.g. [115, 116], and because my supervisor Peter Bøggild and collaborator Maria Dimaki are experienced with DEP of CNTs using metal electrodes.

The DEP electrode layout was designed to utilize as much of the graphitic flakes as possible due to their relatively small size and cumbersome fabrication process. A regular DEP electrode array feature opposing electrodes that can be contacted either with probes or via a common connector to an external circuit. An electrode having either of these connections during the DEP assembly process must be large enough to ensure that the probe or metal connector is not disturbing the electric field in the gap. This put a lower limit on the size of the DEP electrode. However, if one of the electrodes is contacted through capacitive coupling to a backgate electrode, as demonstrated by Krupke et al.[115], that electrode can be made smaller. The principle can be understood as the following (see fig. 5.15): In an AC-supplied circuit resistors, capacitors and coils are commonly described as impedances. In this case three impedances are of importance to the self-limiting DEP process: The backgate's capacitive coupling to the isolated electrode(s) and the impedances of the gap with and without a CNT present (when covered by an aqueous CNT dispersion). At the beginning of the experiment, when no CNT reside in the gap, the AC-signal across the gap, $V_{\mathrm{gap,open}}$, is given by

$$V_{\mathrm{gap,open}} = V_{\mathrm{a}} \frac{Z_{\mathrm{gap}}}{Z_{\mathrm{gap}} + Z_{\mathrm{ins}}} \tag{5.1}$$

where V_{a} is the applied voltage, Z_{gap} the open gap impedance and Z_{ins} the

impedance of the isolated electrode's coupling to the backgate. When a CNT is attracted by the DEP forces and sticks to the electrodes, spanning the gap, the impedance of the CNT and its contacts to the electrodes, Z_{CNT}, is connected in parallel with the gap impedance. The AC-signal across the gap, $V_{\mathrm{gap,CNT}}$, is then given by

$$V_{\mathrm{gap,CNT}} = V_{\mathrm{a}} \frac{Z_{\mathrm{gap}} \parallel Z_{\mathrm{CNT}}}{Z_{\mathrm{gap}} \parallel Z_{\mathrm{CNT}} + Z_{\mathrm{ins}}} \tag{5.2}$$

The self-limiting effect relies on the capture of a CNT causing the gap voltage (and thereby the DEP force) to drop below the threshold of attracting additional CNTs[12].

The relative change from $V_{\mathrm{gap,open}}$ to $V_{\mathrm{gap,CNT}}$ is determined by the impedances, while V_{a} can be used to tune the amplitude close to the threshold. The design parameters of the DEP system are thus mainly the choice of AC frequency, ω, and the impedance Z_{ins}. The latter can be approximated by

$$Z_{\mathrm{ins}} \simeq \frac{1}{\omega C_{\mathrm{ins}}} = \frac{d_{\mathrm{ins}}}{\omega \epsilon_{\mathrm{ins}} A_{\mathrm{elec}}} \tag{5.3}$$

where the influence of the dispersion is not accounted for. C_{ins} is the parallel plate capacitance of the isolated electrode to the backgate, ϵ_{ins} is the permittivity of the insulator (in this case SiO_2) and A_{elec} is the electrode area. For the initial testing Z_{CNT} is assumed much smaller than Z_{gap}. Z_{ins} is then designed to be somewhat larger than Z_{CNT} to ensure that the change from $V_{\mathrm{gap,open}}$ to $V_{\mathrm{gap,CNT}}$ is significant. As a reference we used the resistance of 2-5 MΩ of CNTs assembled by DEP on metal electrodes, reported by Vijayaraghavan et al.[116]. We chose to use 1 MHz and make the electrodes approximately 40 μm^2, to get $Z_{\mathrm{ins}} \approx 10$ MΩ (using $d_{\mathrm{ins}} = 90$ nm, $\epsilon = 3.9\epsilon_0$).

5.3.1 Fabrication and test

The same processing as used to fabricate OFET templates was employed to make arrays of DEP electrodes, see app. F. Graphene as well as thin graphite flakes where used to enable direct comparison at different stages of the process: in fabrication and for future studies of the DEP performance as well as the electrical characteristics of finished devices. To increase the chance of getting a successful design from the start, several different layouts were realized in the first batch. Some of these are shown in fig. 5.16. The pitch of the capacitively coupled electrodes have been designed to match a micro four point probe of either 8 or 16 μm pitch. This enable multiple contacts if the capacitive coupling did not work, or if live monitoring and control of the DEP process (see app. C.4) would be necessary in future studies. A variation of the gap size was also introduced to differentiate devices in these arrays, since the optimum device length for the process was not known from the start. Thus we designed the gaps to be 1, 1.5, 2.5 and 4.0 μm. To make the electrode tips robust to process variations a semi-circular shape was chosen. If e.g. the resist is overexposed the gap would become longer, but the semi-circular shape maintained. Indeed this was the case; the realized gap sizes were 1.5, 2.0, 3.0 and 4.5 μm but the electrode shape remained the same (the E-beam dose was not fully optimized).

[12] It should be noted that Vijayaraghavan et al.[116] propose a different explanation of the self-limiting mechanism.

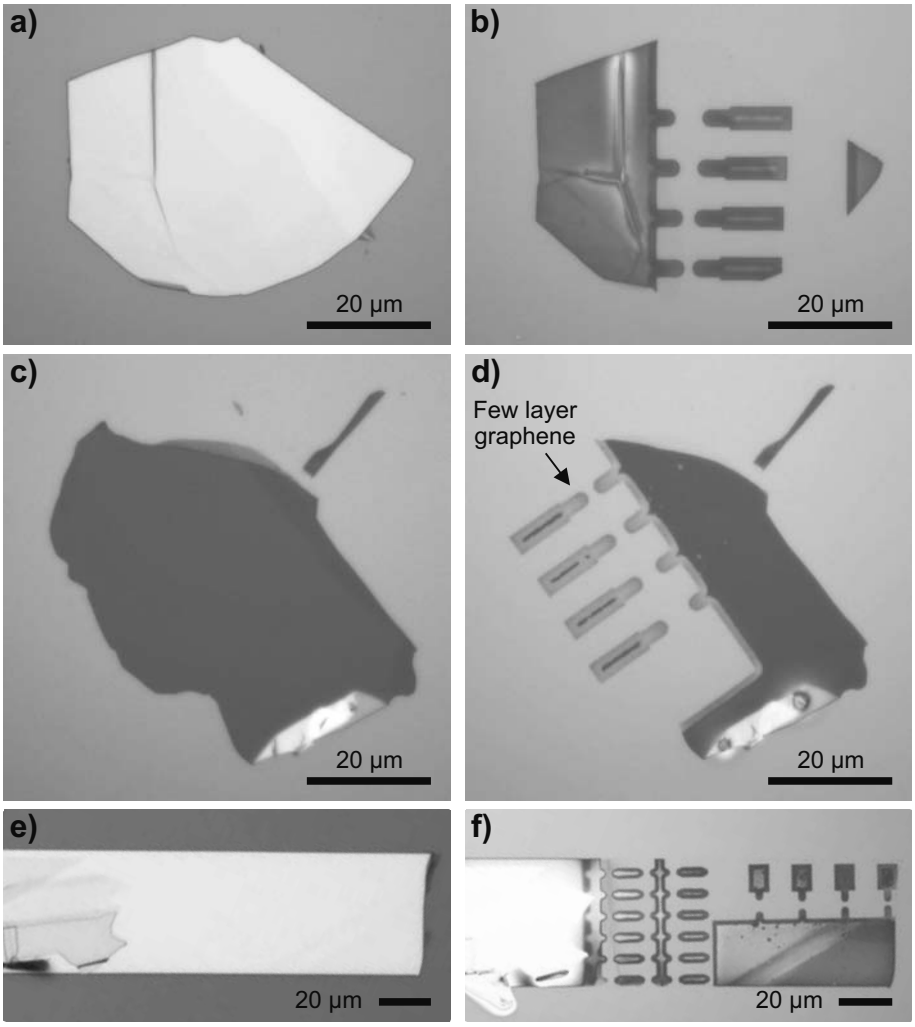

Figure 5.16: Optical microscope images of thin graphite flakes patterned into DEP template arrays. a) The thin graphite flake of b) before lithography. b) The finished DEP template after RIE processing. c) Thin graphite flake of d) before lithography. d) Notice how the edges are significantly thinner than the major part of the electrode (lower contrast). From this image the edge thickness is estimated to only a few layers of graphene. e) Relatively thick graphite of f) before lithography. f) Examples of larger 16 µm pitched electrode pads (right side) and an array of numerous 8 µm pitched electrodes with uniform device gaps.

An unexpected feature of the E-beam lithography process turned out to be useful for the fabricated templates, when patterning multi-layer graphene or graphite flakes. Notice how the edges of the electrodes in fig. 5.16 have significantly lower contrast to the substrate compared to the major part of the common electrodes. The ZEP resist layer was thinner at the edges, thus the RIE processing etched through the ZEP mask faster at the edges. Short RIE cycles could then be repeated until the electrode tips were thinned down to the desired thickness. Maintaining a somewhat thicker graphite electrode in the areas where microprobes contact the flakes gives higher robustness against probing damages and harder engages can be used. In this way it was possible to make few-layer thin graphene electrode edges as shown in fig. 5.16d.

Dielectrophoresis experiments were carried out using a dispersion of multi-walled CNTs (MWCNTs) in an aqueous sodium dodecyl sulfate (SDS) solution. Initially a 1 % SDS solution with high MWCNT concentration was used[13]. A typical DEP experiment using the principle of capacitively coupled counter-electrodes, as shown in fig. 5.15, would be conducted the following way: first the sample chip was placed in a setup similar to that described in app. C.2, fig. C.2a. The ground electrode would be connected to the backgate, while the signal probe was engaged on the common electrode of the sample. An approximately 1 µL drop of the MWCNT dispersion was added. An AC-signal of 1 MHz was applied for a preset period, typically 10 to 60 s, initially using 1 V_p. When the preset time had elapsed the signal was turned off. At this point the dispersion had to be removed to enable sample inspection. To avoid the MWCNTs and SDS to precipitate on the sample a simple trick was employed: the signal probe was disengaged some tenths of µm from the surface and then moved a few mm sideways. Capillary forces made the drop stick to the signal probe chip so it was dragged away from the electrodes, leaving almost no residues behind. The sample was further cleaned by a gentle rinse with Milli-Q water. Subsequent inspection of the sample, either in a powerful optical microscope or using an SEM, would reveal if any MWCNTs had been assembled. If not, the experiment was repeated at a higher voltage. In initial experiments most of the graphitic electrodes were washed off the substrate when using the 1 wt% SDS dispersion. To prevent this, the dispersion was further diluted 1:100 with Milli-Q water (i.e. down to 0.01 wt% SDS), which effectively diminished the risk of the graphitic electrodes washing off.

Within this project several tests were carried out to find the useable parameter space of AC-frequency, voltage, how long it should be applied and how dilute the dispersion should be. The state of the experiments upon finishing this project was a proof-of-concept, that MWCNTs could be assembled by DEP on graphitic electrodes with the capacitively coupled counter-electrodes. The last result is shown in fig. 5.17, where multiple MWCNTs are assembled at the thin graphite electrodes.

Notice that the electrodes in the SEM images appear to have a somewhat rough surface structure. In preliminary experiments random graphite flakes separated by a few microns were used for testing. SEM images of these showed the same surface texture so it can be excluded to be an effect of the lithographic

[13]The parent mixture was kindly supplied by colleague Kristian Mølhave who had prepared it with a ratio of 48.7 mg Fe catalyzed MWCNTs to 50 mL 1 wt% SDS solution with subsequent ultrasonic treatment. A few mL of this parent dispersion was centrifuged to filter out the heavier non-CNT carbon residues, in order to obtain a dispersion suitable for DEP.

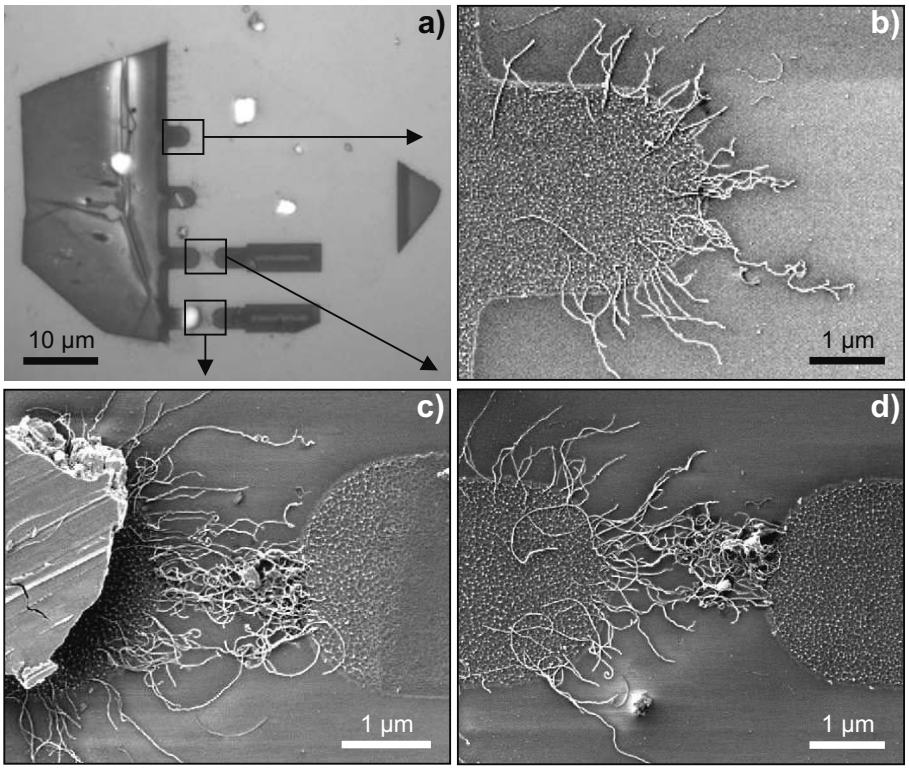

Figure 5.17: MWCNTs assembled by DEP at thin graphite electrodes. a) Optical microscope image of the thin graphite electrode array shown in fig. 5.16b. After several DEP experiments, two electrodes had been washed off. b)-c) 0.5 keV SE1 (inlens detector) SEM images of MWCNTs, zooms of the areas indicated in a). b) MWCNTs have assembled at the common electrode edges even where the capacitively coupled counter electrodes had been washed away. c) 1.5 µm gap between thin graphite electrodes. The particle on the left electrode is presumably a piece of Si. d) 2.0 µm gap between thin graphite electrodes. The experiment parameters were 10 V_p at 1 MHz for 61 s using the 0.01 wt% SDS dispersion.

processing. It could possibly be a layer of SDS that is not washed off by the sample rinsing. SDS is specifically chosen for its ability to bind on CNTs and keep them from agglomerating in the dispersion. Therefore it should also be anticipated that it sticks well on the graphitic electrodes.

It is observed that that MWCNTs have assembled almost at the entire perimeter of the common electrode, upon which the AC-signal was applied. The density of MWCNTs was higher in the electrode gaps, compare fig. 5.17b with 5.17c+d. From this it can be concluded that the template is working. To exclusively assemble MWCNTs in the intended device gaps, possibly down to a single entity, the experiment parameters should be tuned towards lower supply voltage, applying the signal for shorter time, or to further dilute the MWCNT dispersion.

The remaining tuning of the DEP parameters and electrical characterization of the devices could not be conducted within the time frame of this project.

5.3.2 Evaluation of graphitic DEP electrodes

Mechanical exfoliation of natural graphite on SiO_2 wafer surfaces, produces a limited number of few-layer graphene flakes large enough to hold a useable DEP electrode layout. Therefore multi-layer graphene and thin graphite flakes were mainly used and thinned down to few layers in the final RIE processing step. There are three major advantages with this approach compared to only using flakes already few-layers thin. First of all a higher yield of devices from each batch can be obtained. Secondly, the developed process causes the edges to be etched more than the probe contact area thus resulting in more stable electrodes, even when the edges are thinned down to few-layer thicknesses. The third advantage is in the removal of ZEP resist. If single or few-layer graphene is used, remaining resist must be removed in a final process step. Complete removal of ZEP resist is however difficult to obtain, why residues may remain on the sample. This is not an issue when multi-layer graphene is patterned, because all resist can be completely removed in the RIE processing, which thereby produce very clean electrodes. On the downside, graphite thinned down to few-layer graphene by RIE processing may have more defects in the crystal lattice. Generally it is not considered a problem, but may be an issue for some applications, e.g. if the high-mobility properties of graphene is needed.

For DEP experiments the graphitic electrodes performed relatively well. The same templates could be used several times to test DEP parameters; until (MW)CNTs were assembled on the devices, the sample could be rinsed and reused. Once (MW)CNTs reside on the devices they do not come off easily, which is very convenient in the experimental work. Electrodes being washed off is not a major issue for the use of this system, as long as only dilute SDS solutions are applied.

It is common to perform an annealing of the devices after DEP assembly to reduce the contact resistance between electrode and CNT. Typically this is done by baking the sample at a few hundred Celsius[116]. Such treatments are equally applicable to graphitic electrode devices due to the high temperature stability of graphene.

5.4 Chapter summary

Three new and very different uses of graphene has been developed and described in this chapter. The graphene and graphite electrode platform for OFETs offers effective production of relatively many devices compared to the size of the graphene flakes. Furthermore a direct comparison of electrodes with different thicknesses is possible, enabling studies of the influence from graphene's lower work function and higher field enhancement factor. SiO_2 was found to be a very poor gate insulator, causing the OFET characteristics to be dominated by hysteresis and memory effects. Possible solutions such as using top gates and a trap-free insulator are good candidates to solve the challenges.

Two different growth modes of crystalline *p*6P, one of them nanofiber-like, have been observed on graphite and graphene substrates. Molecular and preferred morphological orientations were probed and found to resemble *p*6P crystal phases previously reported on substrates such as mica[15], TiO_2[113], KCl[114] and HOPG[112]. Probing of molecular orientations by the commonly applied detection of polarized fluorescence was applied. However, it was discovered that the reflectance of blue light from the samples equally well can be used instead. This is a very useful development of the probing technique, since UV-excitation, and thereby bleaching of the sample, can be completely avoided.

Future applications for devices based on molecular crystals grown directly on a graphite or transparent graphene electrode can be envisaged. However, a more straight forward application would be to use suspended graphene as a template in the research of molecular crystals e.g. by TEM studies. Such a sample has already been produced in this project, which demonstrates the immediate applicability of the principle (see fig. 5.14).

The third novel application of thin graphite and graphene electrodes was for DEP purposes. A way of using robust graphite electrodes, with edges thinned down to few-layer graphene, has been developed. The issue of electrodes being washed off by the commonly used SDS solution was solved, and templates could be used several times simply by rinsing with Milli-Q water between experiments. Finally DEP assembly of MWCNTs at the edges and in the gaps between thin graphite electrodes was demonstrated.

An E-beam lithography process was developed for patterning both graphene and thin graphite flakes exfoliated from natural graphite on a SiO_2 wafer surface. Additional process steps were implemented to avoid contamination of the E-beam writer. Although the untraditional use of an optical microscope to open small holes in the protective photo-resist layer is working well, I anticipate that a change of systems would promote the fabrication and furthermore open new possibilities of patterning graphene transferred to arbitrary substrates (as discussed in app. F. Avoiding the time-consuming process steps necessary to use the Danchip E-beam facility could significantly decrease the turn-around time of experiments. This is in particular an important parameter in graphene research where many groups compete to publish results first.

Chapter 6

Conclusions

Research in crystalline organic semiconductors is focussed on fundamental material characterization such as crystalline phases, growth mechanisms and optical properties. *Para*-hexaphenylene (*p*6P) nanofibers represent a special class of crystalline organic semiconductors with well documented growth parameters and optical properties. This project has focussed on the development of electrically stimulated light emission, i.e. a crystalline *p*6P nanofiber organic light emitting diode (OLED). The standard approach used for thin film OLEDs is not directly applicable to nanofibers. Three different methods of applying Al and indium-tin-oxide top contacts in a layered design were compared. Anodic oxidation of a layer separating the electrodes created good electrical insulation, but caused the Al cathodes to detach from the *p*6P nanofibers. Separator layers of reactively deposited Al_2O_3 and physical vapor depositioned SiO_x were unsuccessful due to insufficient control of the insulating quality. During the project collaboration partners succeeded in fabricating a *p*6P nanofiber light emitting device based on a field-effect transistor structure. This is considered a promising approach as an alternative to the OLED design.

The crystalline domain size in *p*6P nanofibers were investigated by theoretical modeling of electrical measurements on arrays of as-grown nanofibers. Based on a hopping-like transport model of electron charge carriers the periodic distance between hopping sites could be estimated. A value of 23 ± 5 nm was extracted in relatively good agreement with transmission electron microscopy (TEM) studies. This result suggests that the electrical conductivity is dominated by large barriers at domain boundaries instead of intrinsic crystalline properties. This is clearly an issue that should be addressed if applications where current is passed along the nanofiber axis are desired.

Graphene was first reported in its isolated form in 2004 and several promising applications of the novel material have already been demonstrated. Among these is the use of graphene as a transparent electrode material, where large scale fabrication methods have been reported[34, 35]. This project has aimed at investigating the possible field-enhanced injection barrier lowering in organic field-effect transistors (OFETs). To do this a fabrication method was developed compatible with contamination sensitive cleanroom equipment. Several arrays of OFET devices were fabricated on the same batch and mobile electrical micro-probes were used to test selected samples. However, the electrical

characteristics were dominated by contact effects and conventional OFET operation could not be obtained. This was mainly attributed to a significant contact barrier between graphitic electrodes and *p*6P in the bottom gate bottom electrode design. Furthermore significant hysteresis effects were observed, which previous reports suggest is caused by charge trapping in the SiO_2 gate dielectric.

Another application of graphene electrodes was for dielectrophoretic assembly. Arrays of electrode pairs with opposing tips were prepared using the same fabrication technique developed for OFET templates. The use of thin graphite flakes proved to be a suitable way of making robust electrodes. The fabrication process yielded thin electrode edges, down to few graphene layers, while the main part of the electrodes could be kept multiple layers thick. After improving the dispersion used for dielectrophoresis experiments, substrates could be used several times without destroying the electrode pattern, and assembly of multi-walled carbon nanotube bundles was demonstrated.

Growth of crystalline *p*6P domains on graphitic substrates was demonstrated. These were investigated by probing the morphological and molecular orientations of the domains and correlate these with the graphitic lattice. In these investigations it was discovered that blue reflected light from the domains carry the same polarization as the fluorescence from UV-excitation. This result makes it possible to probe the molecular orientation on these samples, while completely avoiding the bleaching effect of UV-excitation. Two different crystal phases were observed at different growth conditions one of them resembling the common β-phase of *p*6P crystals grown on mica. Domains of a different kind were observed on substrates with thicknesses down to single-layer graphene on a SiO_2 surface. The non-β-phase crystalline domains showed growth of nanofiber-like aggregates on the surface, with typical dimensions of up to 500×20 nm^2.

6.1 Outlook

The design of organic nanofiber OLEDs by layered top contacts has useful design features, such as large scale applicability and the possibility to apply transport layers to the anode. If this technique is to become successful, however, significant improvements of the Al cathode adhesion to the *p*6P nanofibers (in case of anodic oxidation) or improvement of the separator insulation (in case of physical vapor deposition) are necessary next steps. While there may be ways to achieve this, electrically stimulated light emission may be more easily obtained through AC-gated OFET designs which has already been demonstrated[52].

The crystalline domain size in *p*6P nanofibers is very dependent on growth conditions and domains larger than the typical device size are necessary if investigation of grain-boundary free crystals is to be obtained. The developed conduction model applied to simple $I(V)$ measurements can be used to estimate the average crystalline domain sizes of as-grown *p*6P nanofibers on insulating substrates. This could be used as an alternative to transferring the fragile nanofibers to alternative supports for TEM investigation.

To assess the applicability of graphene as electron injecting electrodes in OFETs significant improvements of the design must be implemented. Turn-

ing to a "bottom contact top gate" design is anticipated to greatly reduce the contact barriers and using a trap-free gate dielectric should reduce the charge carrier trapping and thereby hysteresis effects. Furthermore an organic semiconductor with a smaller bandgap could be used to reduce both hole and electron barriers[117].

The use of graphene as electrodes for dielectrophoresis or in electrochemical experiments seems more readily applicable. The properties of electrical contacts between carbon nanotubes and graphene edges of different thicknesses can be investigated with the template system developed.

Graphene as a growth substrate has some intriguing perspectives in applications. Being a transparent and well conducting material it could serve as the transparent electrode in crystalline organic light emitting devices. More readily applicable, and in part demonstrated in this project, is the use of suspended graphene as a TEM compatible growth template for organic crystals. This enables TEM investigation of as-grown organic molecular crystals which could advance the research in this class of materials.

Appendices

Appendix A

List of publications

The list of publications is chronologically ordered by the date of submission or presentation. Only publications on work conducted and submitted within the thesis project are included.

- Henrik H. Henrichsen and Peter Bøggild. Graphene electrodes for n-type organic field-effect transistors. *Microelectronic Engineering*, 87, pp. 1120-1122, 2010 (conference proceeding).
- Jakob Kjelstrup-Hansen, Xuhai Liu, Henrik H. Henrichsen, Kasper Thilsing-Hansen and Horst-Günter Rubahn. Conduction and electroluminescence from organic continuous and nanofiber thin films. *Physica status solidi*, in press (2010), (conference proceeding).
- Henrik Henrichsen, Heinz Sturm, Peter Bøggild and Ole Hansen. Submicron organic nanofiber devices with different anode-cathode materials: a simple approach. *Accepted, Journal of Vacuum Science and Technology B, (2010).*

A.1 Other publications

(Co-authored posters are not included in the list).

- Henrik H. Henrichsen, Jakob Kjelstrup-Hansen, Horst-Günter Rubahn and Peter Bøggild. Novel electrode fabrication method for organic nanofiber light emitting devices. *Poster presentation at the Danish Physical Society annual meeting*, 2008.
- Henrik H. Henrichsen and Peter Bøggild. Electrical properties of *para*-hexaphenylene nanofibers: length dependence measured with non-lithographic electrode gaps. *Poster presentation at the Micro Nano Engineering conference*, 2008.
- Henrik H. Henrichsen and Peter Bøggild. Graphene electrodes for n-type organic field-effect transistors. *Poster presentation at the Micro Nano Engineering conference*, 2009.

- Henrik H. Henrichsen, Frank Balzer, Kasper Thilsing-Hansen and Peter Bøggild. Crystalline Organic Nanofiber Growth along Crystallographic Directions of Graphene. *Oral presentation at the Materials Research Society spring meeting*, 2010.

Appendix B

List of Figures

Appendix C

Experimental equipments

This appendix contains relevant details about the non-standard equipments and programs used during the course of this project. Copies of the programs created during the project are properties of the Nanointegration group and are stored in the groups data repository along with user guides to equipment and programs.

The LabVIEW programming environment has been widely used in different experiments due to its easy and comprehensible programming language and good peripheral driver support.

C.1 Custom made evaporation chamber

In 2006 I was contracted as a research assistant to construct this physical vapor deposition system for the Nanointegration group.

During this Ph.D. project the evaporation chamber was used to deposit Sm and Au electrodes on the sample described in chapter 3, and to make reactive deposition of Al as described in section 4.2.

The chamber enables experiments with electrode materials, also organic compounds, which are difficult or impossible to use in the evaporation systems of DTU Danchip. In addition the chamber has a simple and quite precise option of tilting the sample in arbitrary angles without breaking the vacuum. The system is illustrated in fig. C.1. At the bottom of the chamber three thermal evaporation sources are mounted on a baseplate. They are made of a Tungsten basked in which a small crucible can be loaded with various source materials. Film thickness is monitored with a μ-balance sensor. Vacuum is obtained with a turbomolecular pump and a rough backing pump. Deposition is manually controlled with a power supply.

C.2 Electrical device testing

The setup for electrical testing of devices has existed in several different versions developed throughout the project. For OLED testing inverted microscopes were used, such as the one shown in fig. C.2b. This has a very sensitive monochrome EMCCD camera which allow detection of very low light intensities. This was e.g. used for the device shown in fig. 4.10 pp. 42. The OLED shown in fig. 4.1 pp. 32 was tested on an inverted microscope at SDU in Sønderborg with a

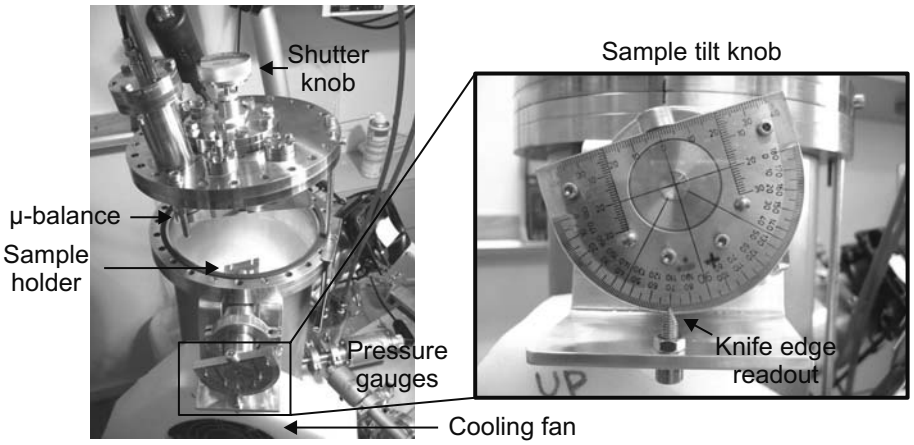

Figure C.1: Pictures of the vacuum chamber used for thermal physical vapor deposition of electrode materials. The halogen lamp used for baking is illuminating the chamber interior. An angle ruler mounted on the sample tilt knob enables precise angle readout at the indicated knife edge.

color camera attached (not illustrated). The OFETs described in section 5.1 were tested in the optical microscope shown in fig. C.2a.

For OFET testing microprobes such as the one shown in fig. C.2d were used (in some cases some of the probes had to be broken off in order not to damage neighbor devices). The probes were placed on devices as shown in fig. 5.3. In principle it should have been possible to use the 4 pins on a single probe, however this was not possible in these measurement situations. The leakage current between the pins was too high and the breakdown voltage too low compared to the voltages applied and current levels measured during the device testing.

The devices described in chapter 3 were tested in a similar setup as that of fig. C.2a, but using sharp metal probes instead of the microprobes due to the more rugged electrodes.

C.2.1 LabVIEW program - Transistor characterization

To acquire series of $I(V)$ measurements a LabVIEW program was developed throughout the project. This was updated several times in order to suit the needs of additional test variables such as well defined pauses in between measurements and a feature to sweep the voltage up and down in one measurement. The program is based on a basic program made by Jakob Kjelstrup-Hansen during his employment in the Nanointegration group. A screenshot of the program's graphical user interface is shown in fig. C.3. The program executes the list of arbitrarily defined voltage sweeps (marked "Voltage sweep intervals") between steps of voltages on a second channel (marked "Constant voltage steps"), while pausing for the preset time between each execution. Proper FET testing involves series of gate voltage sweeps with different constant source-drain voltages and vice versa. The user toggles to the "Vds sweeps with constant Vg"-mode by simply pressing the button marked "Vg sweeps with constant Vds" in

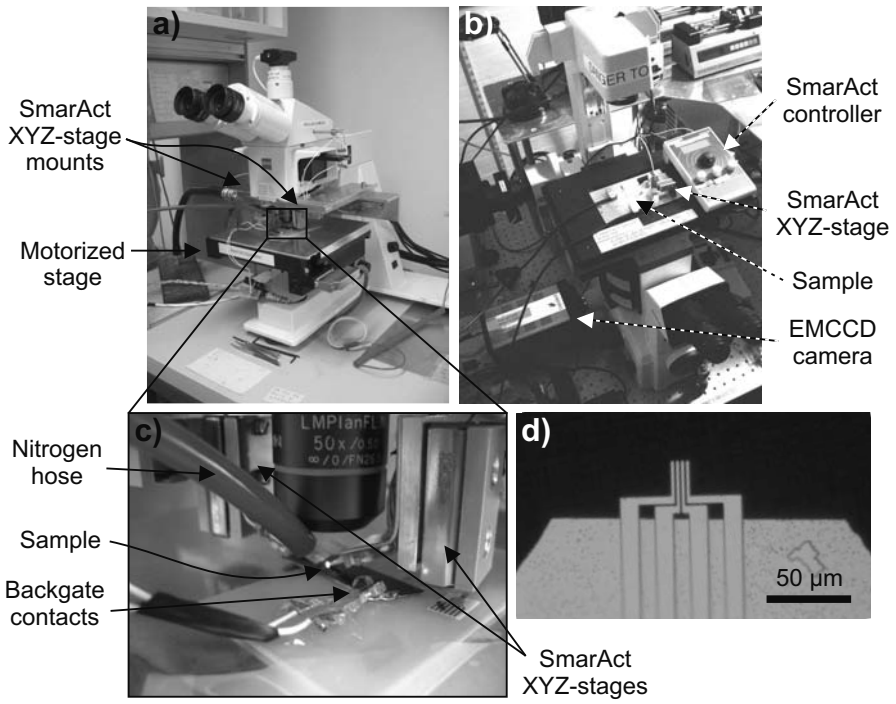

Figure C.2: Setups for electrical testing of devices on optical microscopes. a) Zeiss microscope with sub-micrometer precise motorized stage and a stable mount for two SmarAct XYZ-stages used to place the measurement probes. b) Inverted optical microscope with monochrome EMCCD camera. A SmarAct XYZ-stage is mounted on the sample holder to place the measurement probe from above. c) Close-up of the center of a). The sample chip is placed on an insulating PCB plate, pinned down by two knives serving as backgate contacts. The two SmarAct XYZ-stages are approaching the sample from left and right, each with a measurement probe mounted. d) Micromachined 4 point probe with a 3 µm probe pitch. This is mounted on a small PCB chip compatible with the ZIF-socket standard for easy probe exchange.

the figure. The device characteristics are plotted live during measurements series and vector format preview images of the plots are saved on completion. All relevant measurement parameters and comments are automatically saved in the header of a standard ASCII text file containing the measurement data.

The program communicates directly with a National Instruments data acquisition card (DAQ) (either model 6036E PCMCIA in a laptop or model PCI-6229 in a desktop PC). This only supplies ±10 V so different external amplifiers have been used when larger voltages were necessary. To measure current with sub-picoampere resolution a Standford Research Systems current amplifier model SR570 has been used, which directly interfaces with the DAQ. To monitor the noise in the current signal an oscilloscope was often connected to the output of the current amplifier.

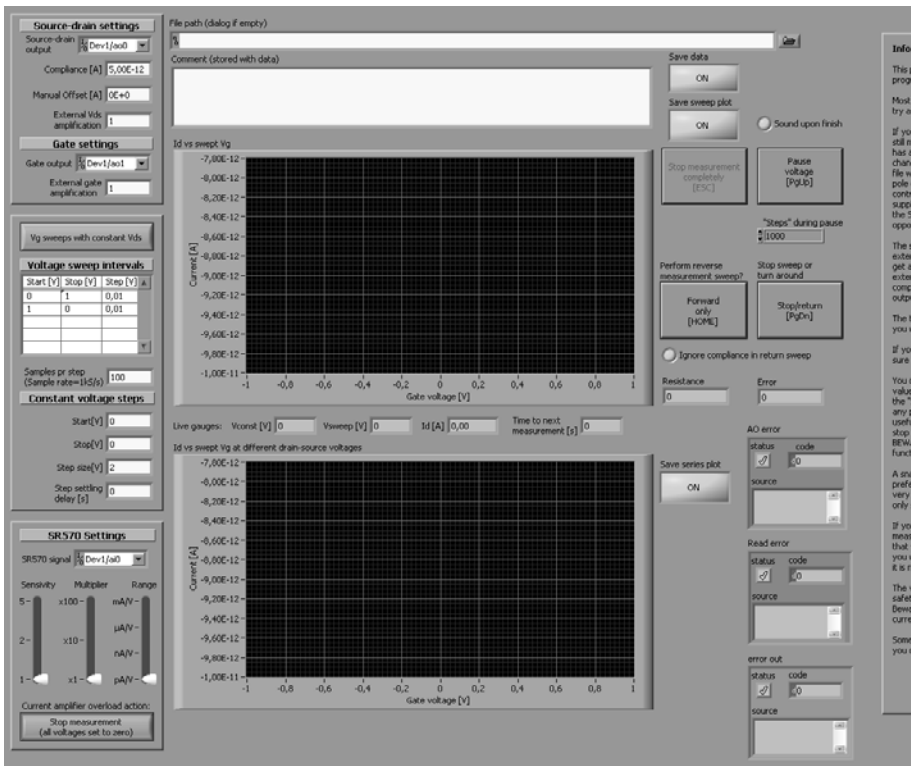

Figure C.3: Graphical user interface of the LabVIEW program used for $I(V)$ and transistor characterization in the version at end of the project.

C.3 Anodic oxidation of Al electrodes

The anodic oxidation experiments conducted in this project were carried out with a Keithley 2400 sourcemeter unit interfaced with LabVIEW. The oxidation rate was controlled by the current density supplied to the electrode. Therefore the sourcemeter was setup as a current supply with a compliance voltage of at least the desired breakdown voltage of the oxide layer. The oxidation process is running until a preset lower current limit is reached or a preset time has elapsed, typically 40 min. All relevant experimental details and comments are automatically saved in the header of an ASCII text file where time, current and voltage are saved on the run.

In a typical experiment the set current density is supplied to the circuit while the voltage steadily increases from a low initial value, due to the very thin initial oxide layer. When the voltage increases to the preset compliance value the current density decreases until the experiment stops, see fig. 4.4 pp. 35.

The electrolyte mixture is a buffered tartaric acid, mainly based on the solution reported by Hasegawa et al.[118]. The ingredients are: propylene glycol, de-ionized water, tartaric acid (pellets) and 33% concentrated NH_4OH in water. The mixing procedure started by putting 194 mL de-ionized water in a bottle and add 6 g of tartaric acid pellets to form a 3% solution. A few mL

of NH_4OH was added until the pH value was approximately 6. The 200 mL lasted for several experiments, since only about 50 mL was used and diluted 1:4 with propylene glycol to form the electrolyte solution.

On each sample 40 individual electrodes were formed by e-beam PVD of Al through a mechanical shadow mask as illustrated in fig. 4.3 pp. 34. Most of the electrodes were connected together by shadowing 2/3 of the electrodes length with a piece of metal tape and deposit a second metal layer on the sample. This was used to connect all devices to the anode during oxidation. To ensure correct current density throughout the experiment approximately 1 cm^2 of Al covered sample area was submerged, and from that the compliance current was set. Typically 0.4 mA/cm^2 was used.

On some of the samples a NaOH based solution was used to remove the thin "skirt" on the nanofibers next to the Al electrodes after oxidation. This was done by diluting standard "Developer 351"[119], 1:5 with de-ionized water. The sample was submerged in this for 30 s and then immediately put in a beaker with pure de-ionized water to wash away the etchant. On the first sample this worked quite well, but on subsequent electrodes detached from the samples. In all cases most of the *p*6P nanofibers not partly covered by the Al electrodes were washed off which, however, would not affect the performance of the devices.

C.4 Dielectrophoresis control

In this project dielectrophoresis experiments were conducted with two different device configurations. In both cases electrodes with a small gap is fabricated on an insulating SiO_2 surface of a highly doped Si chip. The most common way of doing dielectrophoresis would be to ground one electrode while supplying an AC signal to the opposing electrode. Alternatively the Si chip bulk can be grounded and the AC signal applied to one electrode as demonstrated by Krupke et al.[115]. When a proper frequency is used the electrically floating opposing electrode will be capacitively coupled to the grounded substrate with a lower impedance than the electrode gap. An electric field will be in the electrode gap until the dielectrophoretic force has attracted a CNT which decreases the gap impedance. This will diminish the electric field and thereby bring the dielectrophoresis process below its threshold value for effective CNT attraction[1]. When one electrode is held floating in the self-terminating configuration it is of course not necessary nor possible to monitor the impedance of the electrode gap during the experiment. But in the traditional experimental setup where both electrodes are contacted with a probe it is possible, and indeed very useful, to monitor the gap impedance and stop the experiment when the impedance drops to a desired value. For this purpose I developed a LabVIEW program for easy, optimum and consistent experiment control and data logging. The program interfaces a Tabor Electronics 8550 function generator and an Agilent 54621A oscilloscope used to sample the high frequency signals. To measure impedance a shunt resistor was inserted in series with the electrode gap, and signals acquired as illustrated in fig. C.4. The voltage across the shunt gives a signal proportional to the current and thus enable calculation

[1]It should be mentioned that Vijayaraghavan et al.[116] propose a different explanation of the self-limiting mechanism.

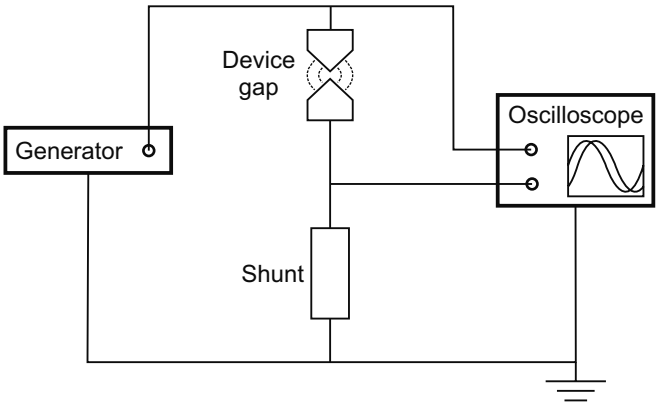

Figure C.4: Electrical wiring diagram when the labVIEW program is used to control dielectrophoresis in a traditionally connected electrode gap.

of device impedance modulus and the current-voltage phase. Feedback features were incorporated into the program to maintain constant electric field strength across the electrode gap throughout the experiments. The program automatically stops the experiment when gap impedance has reduced to a preset value. All relevant experimental data and comments are automatically saved in the header of an ASCII text file along with the evolution of the gap impedance (modulus and phase). For convenient overview of experiments a vector format image of the impedance plot vs. time is also saved automatically.

C.4.1 LabVIEW program - Impedance spectrum analyzer

Once the dielectrophoresis control program was made an impedance spectrum analyzer using the same setup and pin connections could easily be developed. This was used to investigate the frequency response of the system and the CNT dispersions used for the dielectrophoresis experiments. This was important to test the system's influence on the experiments.

C.5 LabVIEW program - "Get the big picture"

I made this program in order to enable easy high resolution imaging of large sample areas, but also with several other spin-off projects in mind. One of them is automatic device inspection on full wafers which could be developed further into automated device testing e.g. by using the SmarAct XYZ-stage mount shown in fig. C.2. In this project I also used it to acquire images for the automated graphene tracker program described in app. C.6.

The program acquires images from a µEye UI-1465LE-C USB camera mounted on a Zeiss Axiotech microscope. The sample position is controlled with a motorized ASI MS-2000 XYZ stage. The stage moves the sample with pixel size precision in a user defined array pattern. The images can simply be put together to form one big downsampled image of the sample. For subsequent analysis programs (see app. C.6) the individual images can be saved as well. Thus a whole 4" wafer can be imaged; using 10× magnification this requires

more than 10,000 images. Autofocus routines have also been implemented to ensure focused images of the whole sample.

When many small images are concatenated into one big image the uneven illumination of the microscope becomes clearly visible as a periodic overlay on the image. This can be avoided by flattening the source images with an illumination reference of the microscope. A few hundred images of the sample at different positions averaged together usually constitutes a very good illumination reference. Automatic image flattening was implemented in the program so concatenated images have true seamless stitching.

C.6 LabVIEW program - Graphene scanner

In the Nanointegration group we have mainly produced graphene flakes by the mechanical exfoliation technique brought to the group by Timothy John Booth. Usually a part of the process is an hours-long manual scanning across the wafer with an optical microscope to identify flakes of graphene useable for experiments. Since this trivial task must be conducted relatively often in our research it makes good sense to automate it. I made a program that automatically categorizes graphene flakes with respect to area and global wafer coordinate if it was given an ensemble of images covering a whole wafer - such as the 10,000 images acquired with the "get the big picture"-program described in app. C.5. The identification criteria was based on the distinct color single and few layer graphene flakes have on a 90 or 300 nm SiO_2 layer. The color is highly dependent on the intensity of the microscope light so the first graphene flake must be found manually in order to adjust the red, green and blue color filter intervals so they only pass the color of the desired graphene flakes. Once this is done the rest of the images are automatically processed and additional particle filters are applied in order exclude non-graphene samples that pass the color filtering.

Although the contrast of a single-layer graphene flake is relatively large for a single atomic layer, it is still in the order of the intensity variation across a microscope image due to uneven illumination. The image illumination must be flattened before the program effectively can identify graphene flakes in all parts of the images. A reference image of the illumination distribution is easily created by averaging a few hundred images from the ensemble to be scanned. This is then used to flatten the images before analysis.

Although the program works it has not been used extensively to track useable graphene flakes. The main reason is that imaging a whole wafer with the program described in app. C.5 takes a few hours and the following categorization also takes up to an hour. The processes are automated but the operator still has to set up and start the processes. Instead of the automated tracking a manual approach has been used. Using a good microscope a wafer can be scanned with down to 5× magnification, and the operator can immediately determine if a graphene or graphite flake is useable for the experiment in mind. This typically takes four hours, so the time consumption for the two methods are comparable. For higher volume production of e.g. only single-layer graphene a proper implementation of the automated tracking would be beneficial.

Appendix D

Deposition angle calculation

This appendix describes the geometric calculations used to determine the expected result of angled metal deposition through a mechanical shadow mask with perfect circular cross section. Figure D.1 illustrates relevant segments, lines and angles used in the following calculations of electrode gap length and edge blur. For ease of use the scheme was put into an Excel sheet. First the pieces l_1, l_2 and l_3 are calculated:

$$\begin{aligned} l_1 &= l_\mathrm{r}(1-\cos\theta) \\ l_2 &= l_\mathrm{r}(1-\sin\theta)+l_\mathrm{sm} \\ l_3 &= l_2\tan\theta \end{aligned} \tag{D.1}$$

Where θ is the angle of deposition measured as the sample surface normal relative to the line of sight from the source. When the same deposition angle

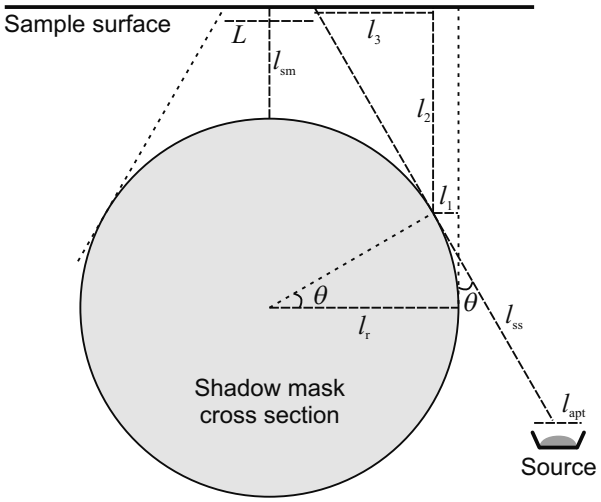

Figure D.1: Relevant lines, angles and segments used to calculate the expected result of an angled deposition through a shadow mask with circular cross section. l_ss is the sample to source distance, l_sm is the sample to mask distance and l_apt is the evaporation source aperture. In the experiment l_ss would normally be vertical and the sample surface sloped.

but with opposite sign is used in the deposition of the two electrode materials, the device length, L, is then given by:

$$L = 2(l_{\mathrm{r}} - l_1 - l_3) \tag{D.2}$$

The electrode edge blur is given by:

$$l_{\mathrm{blur}} = l_{\mathrm{apt}} \frac{\frac{l_2}{\cos\theta}}{l_{\mathrm{ss}}} \tag{D.3}$$

Relevant parameters for the experiment discussed in chapter 3 are $\theta = 18°$, $l_{\mathrm{ss}} = 26$ cm, $l_{\mathrm{r}} = 2.8$ µm, $l_{\mathrm{apt}} = 8$ mm.
Relevant parameters for the experiment discussed in section 4.3 are $\theta = 0°$, $l_{\mathrm{ss}} = 14.6$ cm, $l_{\mathrm{apt,Al}} = \sim 3$ mm, $l_{\mathrm{apt,SiO_x}} = \sim 10$ mm, $l_{\mathrm{r}} = \sim 10$ µm and $l_{\mathrm{sm}} = 15$ µm.

Appendix E

Conduction model adaption details

As stated in chapter 3 referring to this appendix, the adaption of the transport model described by Grove[62] was mainly done by Ole Hansen.

The model is based on the transport physics of ionic impurities moving through a biased periodic potential, see fig. E.1. Originally the model was made to describe positive ions moving through a crystal lattice, but in this application it will describe electrons moving through the periodic energy potential of an organic *p*6P nanofiber. It is applicable for particles with Boltzmann distribution in energy i.e. at energies far from the Fermi level.

In the following version of the model diffusion is assumed much smaller than the drift current, which is justified by the high electric field strength applied. The flux of particles (electrons) in either direction through the biased periodic

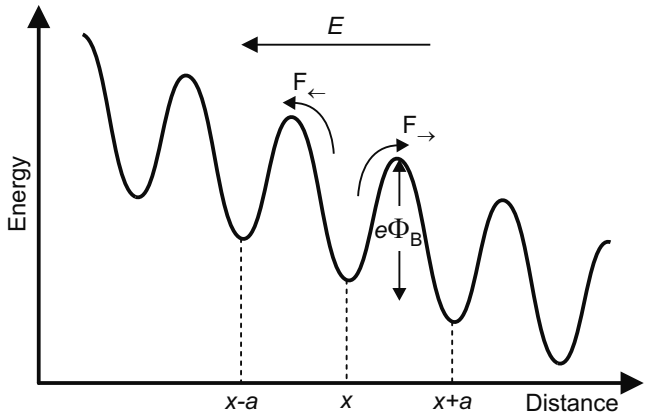

Figure E.1: Conduction scheme of particles governed by Boltzmann statistics. $e\Phi_B$ is the zero-field barrier and a the distance between barriers. $F_{\rightarrow}$ and $F_{\leftarrow}$ describe the particle flux in either direction of the electric field. Particle concentration is assumed the same in all domains. Adapted from [62].

potential of fig. E.1 is described by classical physics[62, pp. 37]:

$$F_{\rightarrow} = \nu a n \exp\left[-\frac{e}{k_{\mathrm{B}}T}\left(\Phi_{\mathrm{B}} - \frac{1}{2}aE\right)\right] \tag{E.1}$$

$$F_{\leftarrow} = \nu a n \exp\left[-\frac{e}{k_{\mathrm{B}}T}\left(\Phi_{\mathrm{B}} + \frac{1}{2}aE\right)\right] \tag{E.2}$$

The concentration of particles within each domain of length a is described by the product an, n being the spacial concentration. The exponential function describes the chance of a particle jumping over the barrier. The $\mp\frac{1}{2}aE$ part of the argument is the contribution of the electric field to barrier de- and increase respectively. ν is the frequency of jump attempts. The total flux of particles from left to right is then

$$F_{\mathrm{tot}} = F_{\rightarrow} - F_{\leftarrow} = 2na\nu \exp\left(-\frac{e\Phi_{\mathrm{B}}}{k_{\mathrm{B}}T}\right)\sinh\left(\frac{eaE}{2k_{\mathrm{B}}T}\right) \tag{E.3}$$

where the complex definition of hyperbolic sine has been used[1]. The current density is defined as the flux of charges, so multiplying with the elemental charge results in the current density through the device:

$$J = eF_{tot} = en\nu_0 \sinh\left(\frac{E}{E_0}\right) \tag{E.4}$$

For clarity the characteristic drift velocity parameter of the material, $\nu_0 = 2a\nu\exp\left(-\frac{e\Phi_{\mathrm{B}}}{k_{\mathrm{B}}T}\right)$, and characteristic field parameter, $E_0 = \frac{2k_{\mathrm{B}}T}{ea}$, have been introduced. The charge density, ρ, is given by en which can be isolated from eq. (E.4) and by dividing with permittivity Poissons equation, $\frac{dE}{dx} = \frac{\rho}{\epsilon}$, results:

$$\frac{J}{\nu_0 \sinh\frac{E}{E_0}} = en = \rho \Leftrightarrow \frac{\rho}{\epsilon} = \frac{J}{\epsilon\nu_0 \sinh\frac{E}{E_0}} = \frac{\mathrm{d}E}{\mathrm{d}x} \tag{E.5}$$

This equation must be solved to reach a form that express the measured current as a function of the applied voltage so the model can be fitted with measurements. First the variables are separated and a current density dependent characteristic length parameter is introduced:

$$\sinh\left(\frac{E}{E_0}\right)\frac{\mathrm{d}\frac{E}{E_0}}{\mathrm{d}x} = \frac{J}{\epsilon\nu_0 E_0} = \frac{1}{\Lambda} \tag{E.6}$$

The integration is performed with the lower boundaries being at the top of the barrier at the cathode in fig. 3.5, i.e. $E = 0$ and $x = \Delta$:

$$\int_0^{\frac{E}{E_0}} \sinh\left(\frac{E'}{E_0}\right)\mathrm{d}\frac{E'}{E_0} = \int_{\Delta}^{x}\frac{1}{\Lambda}\,\mathrm{d}x' \tag{E.7}$$

$$\cosh\frac{E}{E_0} - 1 = \frac{x-\Delta}{\Lambda} \tag{E.8}$$

$$\frac{E}{E_0} = \operatorname{arccosh}\frac{x-\Delta+\Lambda}{\Lambda} \tag{E.9}$$

[1] $\sinh x = \frac{1}{2}\left[\exp(x) - \exp(-x)\right]$

This must be integrated once more to get to the potential instead of the field:

$$\frac{1}{E_0}\frac{\mathrm{d}\Phi}{\mathrm{d}x} = \operatorname{arccosh}\frac{x-\Delta+\Lambda}{\Lambda} \tag{E.10}$$

$$\int_0^{\Phi}\frac{1}{E_0}\,\mathrm{d}\Phi' = \int_{\Delta}^{x}\operatorname{arccosh}\frac{x'-\Delta+\Lambda}{\Lambda}\,\mathrm{d}x' \tag{E.11}$$

The right hand side integration variable is substituted:

$$u = \frac{x\prime-\Delta+\Lambda}{\Lambda} \Rightarrow \mathrm{d}u = \frac{1}{\Lambda}\mathrm{d}x'$$

$$\left[\frac{\Phi'}{E_0}\right]_0^{\Phi} = \Lambda\int_1^{\frac{x-\Delta+\Lambda}{\Lambda}}\operatorname{arccosh} u\;\mathrm{d}u \tag{E.12}$$

$$\frac{\Phi}{E_0\Lambda} = \left[u\operatorname{arccosh}(u)-\sqrt{u^2-1}\right]_1^{\frac{x-\Delta+\Lambda}{\Lambda}} \tag{E.13}$$

$$\frac{\Phi}{E_0\Lambda} = \frac{x-\Delta+\Lambda}{\Lambda}\operatorname{arccosh}\left(\frac{x-\Delta+\Lambda}{\Lambda}\right)-\sqrt{\left(\frac{x-\Delta+\Lambda}{\Lambda}\right)^2-1} \tag{E.14}$$

From the measurements the potential drop over the full length of the device is known, so we are interested in the solution for $x = L$. The Δ and Λ parameters are unknowns so these must be eliminated from the equation. This is done by assuming $L \gg \Delta$ and $L \gg \Lambda$ which is justified in section 3.2.1. Equation (E.14) can then be approximated with:

$$\frac{\Phi}{E_0 L} \cong \operatorname{arccosh}\left(1+\frac{L}{\Lambda}\right)-1 \tag{E.15}$$

$$\frac{L}{\Lambda} = \cosh\left(1+\frac{\Phi}{E_0 L}\right)-1 \tag{E.16}$$

The Λ is substituted into the equation and the device cross sectional area, A, is introduced:

$$J = \frac{\epsilon\nu_0 E_0}{L}\left[\cosh\left(1+\frac{\Phi}{E_0 L}\right)-1\right] \tag{E.17}$$

$$I = A\frac{\epsilon\nu_0 E_0}{L}\left[\cosh\left(1+\frac{\Phi}{V_{\mathrm{C}}}\right)-1\right] \tag{E.18}$$

Equation (E.18) is the final result, where $V_{\mathrm{C}} = E_0 L$ is a characteristic voltage. The scaling parameter in front of the hyperbolic cosine contains both ν and Φ_{B} which are unknown parameters. They are both combined in the ν_0 parameter, which can be estimated if the effective device cross section, A, is known (ϵ_{rel} along the $p6$P nanofibers can be estimated to 1.9[72], and a can be extracted from the data fit). To fit experimental data with eq. (E.18) it is assumed that $\Phi = V_{\mathrm{a}} + \Phi_0 - \Phi_{\mathrm{Bn,A}}$ reduces to $\Phi \simeq V_{\mathrm{a}}$, which is valid at high voltages.

Appendix F

Graphene patterning process

This appendix describes the process used to pattern graphene and thin graphite flakes. To include all possible sources of contamination the complete process is described however only with emphasis on non-standard processing steps.

It should be mentioned that the choice of DTU Danchip's E-beam system in retrospect seems less than optimum. The alternative of using an SEM based lithography system, such as the FEI HELIOS EBS3 available at DTU CEN, has certain advantages. A single layer of PMMA[1] resist could be used which greatly reduces the processing and is easier to remove than ZEP resist. Furthermore the system features gas assisted etching with the E-beam, a resist-less process which is an interesting alternative. This could enable patterning of graphene transferred to arbitrary systems, such as suspended graphene on TEM grids.

Following is the complete process at the level to which it was developed by the end of the project. The parts on applying graphene to the wafers is mainly the process brought to DTU by Timothy John Booth. Special steps are explained in the following notes.

Step 1: Highly antimony doped wafers (n-type, resistivity <0.025Ωcm) are used. A 90 nm dry thermal oxide is grown at 1050°C in 70 min.

Step 2: Indexed alignments marks (pitch 500 µm) are made on the wafers with a standard photolithography lift-off process (using NaOH based developer). The index marks are 5 nm Ti + 45 nm Au applied by PVD.

Step 3: The process of applying graphene to the SiO_2 surface is based on the work of Novoselov et al.[37]. To apply graphene flakes start by cleaving a piece of natural graphite and stamp it repeatedly onto a piece of cleanroom compatible tape to distribute graphite on it. Apply a similar piece of tape to sandwich the graphite flakes. Bake the wafers on a 120°C hotplate for 5 min. Immediately after give the wafers an oxygen plasma treatment e.g. 200 mL O_2 + 50 mL N_2 at 1000 W for 10 min. When the wafers are extracted from the plasma immediately pull the two pieces of tape apart to create freshly cleaved graphite faces and apply them to the wafers. When the tape is pulled off some parts of the graphite flakes will adhere to the SiO_2 surface; some of which will be single and few layers. [TIP: Alternatively use a furnace to bake the wafers

[1]Poly(methyl methacrylate) also known as "acrylic" or commercially as PLEXIGLAS. A widely used resist for E-beam and imprint lithography.

at 500°C instead of the plasma process, to avoid damaging the SiO_2 electrical properties. To ensure no HMDS remain from the photolithography initially rinse the wafers in a TMAH based developer followed by a water rinse].

Step 4: Remove readily visible graphite flakes from the wafer surface to avoid contamination in following processing. The loose parts are blown away with compressed nitrogen the stuck parts can be removed with a small piece of tape.

Step 5: Find suitable graphene and thin graphite flakes for the device fabrication. This is done by scanning the wafer with an optical microscope and identify flakes by their contrast[33]. Flakes are conveniently logged simply by acquiring an image of the flake where two index marks are visible (this is used to align the subsequent lithography layout). (This process has been automated using LabVIEW, see app. C.6).

Step 6: Apply E-beam resist: Prebake the wafer at 160-200°C for 5 min. Generously apply ZEP520A 3.6% and spin the wafer 30 s at 3500 rpm (400 rpm/s acc.) to obtain a ∼90 nm thin layer. There may be small "flares" in the resist due to some of the thicker graphite flakes but these are usually not disturbing the lithography. Postbake the wafer at 100°C for 5 min.

Step 7: (See note 1) Apply a 10 µm layer of AZ4562 photo resist[119]. To avoid the resist from cracking in the following process the photo resist is either postbaked an additional 15 min at 90°C or stored a few days. (Presumably the last step drives more solvent out of the photo resist).

Step 8: (See note 2) At the sites where E-beam lithography is intended the thick photo resist must be removed. To expose the resist in spots 340 µm in diameter a Nikon Eclipse L200 optical microscope is used. First fully open the "A.S." aperture to allow maximum intensity. Insert the green filter. Bring the first graphene/graphite flake of interest in focus with the 100X objective. Turn the lamp power to maximum and pull out the green filter for two seconds to expose the resist. Use the previously saved images to find and expose all areas of interest.

Step 9: Alignment marks for the E-beam process should be ∼10 mm from the wafer edges at the same Y-coordinate, one in each side close to the center line. Wafer index marks are used for this and the thick photo resist is exposed as described in the previous step. [TIP: The index marks chosen for alignment should be free of graphite contamination. This can be ensured by peeling the area with tape in step 4].

Step 10: Clear the exposed holes in the thick photo resist by developing it in MF-322 or MF-319 (TMAH based). Typically 2-3 min are necessary, rinse with water. The profilometer can be used to check that holes are cleared; if the bottom of the holes have a parabola-like shape it has not been fully cleared.

Step 11: A decharging layer of 15-20 nm Al is thermally deposited on the wafer. (E-beam PVD cannot be used for this since it would completely expose the E-beam resist). The layer will ensure high resolution lithography by preventing surface charging.

Step 12: Inspect the wafer by going through all the areas of interest using the optical microscope with the green filter inserted. Acquire a bright- and dark-field image of each site. Bright spots in the dark-field image will reveal if something protrudes the ZEP resist layer.

Step 13: (See note 3) Design the E-beam layout.

Step 14: Perform the E-beam exposure using DTU Danchip's JEOL JBX-9300FS electron beam lithography writer system. A dose of 160 μC/cm^2 at 1.38 nA suffice to make micron-sized features.

Step 15: Remove the Al decharging layer in MF-322 or MF-319. It can take up to 2 min. Rinse with water.

Step 16: Develop the ZEP resist in a bath of ZED-N50 for 30 s where the wafer is gently moved to generate circulation (this will also dissolve some of the AZ4562 resist layer). Immediately after rinse the wafer in two baths of IPA for 30 s in each, again moving the wafer for circulation. If necessary do further rinsing with IPA and finally blow dry the wafer. [TIP: The AZ4562 resist may leave some residues on the wafer. This could be avoided if the layer is completely removed prior to developing the ZEP e.g. by flood exposure. Experiments on this however have not been successful due to severe cracking of the resist].

Step 17: Etch graphite in the open holes of the ZEP resist layer with a low power oxygen plasma. Preferably use the reactive ion etching system (DTU Danchip's RIE2, model STS C010) with 30 W, 20 sccm O_2, 99 sccm N_2 at 100 mTorr. 20 s effective etching will clear single layer graphene patterns. Additional etching of thicker flakes may be necessary. When the ZEP resist is almost gone, processing on the whole wafer must be stopped to avoid damage of few-layer devices. It is possible to differentiate the etching on sample sites by scribing the wafer and brake it into smaller pieces. [TIP: Thicker graphite flakes can also be patterned even though the ZEP resist is etched away before the pattern is cleared. Continued etching will thin the whole flake down evenly and the open parts of the pattern will etch through first]. When etching is complete remaining resist can be removed with anisol (1165 remover will effectively remove the graphite flakes as well). It may be difficult to completely remove all residues. Additional baking on a hotplate at 300° can also remove some residues.

Note 1: Encapsulate larger graphite flakes. DTU Danchip's E-beam system is highly sensitive to contamination so the E-beam lithography is only allowed when larger graphite flakes are encapsulated. This is done by applying a 10 μm layer of AZ4562 photo resist.

Note 2: The thick photo resist layer will significantly scatter electrons in the E-beam lithography step (according to Monte Carlo simulations) and thus it must be removed at sites where lithography is wanted. This is done by a method suggested by Torben Mikael Hansen. The AZ4562 resist is sensitive up to 440 nm light and can thereby be exposed with the standard white light from an optical microscope. A process for this was developed finding that the resist is fully exposed in 2 s when using the 100X magnification objective on a Nikon Eclipse L200 microscope. A spot 340 μm in diameter is exposed. Overexposure typically cause the resist to detach and crack which can be avoided by baking the wafer at 90°C or simply storing the wafer for a few days. This presumably removes residual solvents.

Note 3: The JEOL JBX-9300FS electron beam lithography writer system use a mask file which can be designed using L-Edit. For convenient alignment to the graphene and graphite flakes the images acquired with the alignment

marks can be used as background. The L-edit program can be made semi-transparent with freeware software and the index marks on the microscope image are then easily aligned to the mask in L-Edit. The lithography design can then easily be drawn on the flake.

TIP: It is convenient to use a few generic designs which are then used many times on different flakes.

TIP: By convention of DTU Danchip's E-beam writer the wafer must have the major flat pointing up in the image. Thus it is convenient if the wafer index marks are made with the major flat pointing up.

TIP: The E-beam system mask conversion places the center of your mask at the center of the system coordinate system. Design displacement can be avoided if e.g. a 100x100 nm square is placed in the four outer most coordinates, i.e. $(\pm 5, \pm 5)$cm. These are not within the perimeter of a 4" wafer and thus does not influence the sample.

Bibliography

[1] M. Dimaki and P. Bøggild. Dielectrophoresis of carbon nanotubes using microelectrodes: a numerical study. *Nanotechnology*, 15(8):1095–1102, 2004.

[2] E. Fred Schubert. *Light-emitting diodes*. Cambridge University Press, 2006. ISBN 0521865387, 9780521865388. 433 pp.

[3] N. Zheludev. The life and times of the LED - a 100-year history. *Nature Photonics*, 1(4):189–192, 2007.

[4] Winners' circle: Nick holonyak, jr. http://web.mit.edu/invent/a-winners/a-holonyak.html, 2004.

[5] M. Pope, H. P. Kallmann, and P. Magnante. Electroluminescence in organic crystals. *Journal of Chemical Physics*, 38(8):2042, 1962.

[6] C. W. Tang and S. A. VanSlyke. Organic electroluminescent diodes. *Applied Physics Letters*, 51(12):913, 1987.

[7] S. Reineke, F. Lindner, G. Schwartz, N. Seidler, K. Walzer, B. Lüssem, and K. Leo. White organic light-emitting diodes with fluorescent tube efficiency. *Nature*, 459(7244):234–238, 2009.

[8] D. Fyfe. LED technology: Organic displays come of age. *Nat Photon*, 3 (8):453–455, 2009.

[9] R. Waser. *Nanoelectronics and information technology*. Wiley-VCH, 2003. ISBN 3527403639, 9783527403639. 1001 pp.

[10] X. Zhou, D. S. Qin, M. Pfeiffer, J. Blochwitz-Nimoth, A. Werner, J. Drechsel, B. Maennig, K. Leo, M. Bold, P. Erk, and H. Hartmann. High-efficiency electrophosphorescent organic light-emitting diodes with double light-emitting layers. *Applied Physics Letters*, 81(21):4070, 2002.

[11] M. Pfeiffer, K. Leo, X. Zhou, J. S. Huang, M. Hofmann, A. Werner, and J. Blochwitz-Nimoth. Doped organic semiconductors: Physics and application in light emitting diodes. *Organic Electronics*, 4(2-3):89–103, 2003.

[12] H. Wang, F. Li, B. Gao, Z. Xie, S. Liu, C. Wang, D. Hu, F. Shen, Y. Xu, H. Shang, Q. Chen, Y. Ma, and H. Sun. Doped organic crystals with high efficiency, Color-Tunable emission toward laser application. *Crystal Growth & Design*, 9(11):4945–4950, 2009.

[13] R. Yan, D. Gargas, and P. Yang. Nanowire photonics. *Nature Photonics*, 3(10):569–576, 2009.

[14] D. H. Reneker and I. Chun. Nanometre diameter fibres of polymer, produced by electrospinning. *Nanotechnology*, 7:216–223, 1996.

[15] F. Balzer and H.-G. Rubahn. Dipole-assisted self-assembly of light-emitting p-nP needles on mica. *Applied Physics Letters*, 79(23):3860, 2001.

[16] M. Schiek, A. Lützen, R. Koch, K. Al-Shamery, F. Balzer, R. Frese, and H.-G. Rubahn. Nanofibers from functionalized para-phenylene molecules. *Applied Physics Letters*, 86(15):153107, 2005.

[17] F. Balzer, L. Kankate, H. Niehus, R. Frese, C. Maibohm, and H. Rubahn. Tailoring the growth of p-6P nanofibres using ultrathin au layers: an organic-metal-dielectric model system. *Nanotechnology*, 17(4):984, 2006.

[18] H. Plank, R. Resel, H. Sitter, A. Andreev, N. S. Sariciftci, G. Hlawacek, C. Teichert, A. Thierry, and B. Lotz. Molecular alignments in sexiphenyl thin films epitaxially grown on muscovite. *Thin Solid Films*, 443(1-2): 108–114, 2003.

[19] R. Resel. Surface induced crystallographic order in sexiphenyl thin films. *Journal of Physics: Condensed Matter*, 20:184009, 2008.

[20] S. Guha, W. Graupner, R. Resel, M. Chandrasekhar, H. R. Chandrasekhar, R. Glaser, and G. Leising. Planarity of para hexaphenyl. *Physical review letters*, 82(18):3625–3628, 1999.

[21] F. Balzer and H.-G. Rubahn. Growth control and optics of organic nanoaggregates. *Advanced Functional Materials*, 15(1):17–24, 2005.

[22] R. Resel. Crystallographic studies on hexaphenyl thin films - a review. *Thin Solid Films*, 433(1-2):1–11, 2003.

[23] H. Yanagi and S. Okamoto. Orientation-controlled organic electroluminescence of p-sexiphenyl films. *Applied Physics Letters*, 71:2563, 1997.

[24] J. Kjelstrup-Hansen, H. H. Henrichsen, P. Bøggild, and H.-G. Rubahn. Electrical properties of a single p-hexaphenylene nanofiber. *Thin Solid Films*, pages 827–830, 2006.

[25] P. Puschnig and C. Ambrosch-Draxl. Density-functional study for the oligomers of poly (para-phenylene): Band structures and dielectric tensors. *Physical Review B*, 60(11):7891–7898, 1999.

[26] K. S. Novoselov. Electric field effect in atomically thin carbon films. *Science*, 306(5696):666–669, 2004.

[27] S. Morozov, K. Novoselov, M. Katsnelson, F. Schedin, D. Elias, J. Jaszczak, and A. Geim. Giant intrinsic carrier mobilities in graphene and its bilayer. *Physical Review Letters*, 100(1), 2008.

[28] K. S. Novoselov, Z. Jiang, Y. Zhang, S. V. Morozov, H. L. Stormer, U. Zeitler, J. C. Maan, G. S. Boebinger, P. Kim, and A. K. Geim. Room-temperature quantum hall effect in graphene. *Science*, 315(5817):1379, 2007.

[29] X. Wang, L. Zhi, and K. Müllen. Transparent, conductive graphene electrodes for Dye-Sensitized solar cells. *Nano Letters*, 8(1):323–327, 2008.

[30] S. Pang, H. N. Tsao, X. Feng, and K. Müllen. Patterned graphene electrodes from Solution-Processed graphite oxide films for organic Field-Effect transistors. *Advanced Materials*, 21(34):3488–3491, 2009.

[31] J. Wu, M. Agrawal, H. A Becerril, Z. Bao, Z. Liu, Y. Chen, and P. Peumans. Organic Light-Emitting diodes on Solution-Processed graphene transparent electrodes. *ACS nano*, 4(1):43–48, 2010.

[32] R. R. Nair, P. Blake, A. N. Grigorenko, K. S. Novoselov, T. J. Booth, T. Stauber, N. M. R. Peres, and A. K. Geim. Fine structure constant defines visual transparency of graphene. *Science*, 320(5881):1308–1308, 2008.

[33] P. Blake, E. W. Hill, A. H. Castro Neto, K. S. Novoselov, D. Jiang, R. Yang, T. J. Booth, and A. K. Geim. Making graphene visible. *Applied Physics Letters*, 91(6):063124, 2007.

[34] G. Eda, Y.-Y. Lin, S. Miller, C.-W. Chen, W.-F. Su, and M. Chhowalla. Transparent and conducting electrodes for organic electronics from reduced graphene oxide. *Applied Physics Letters*, 92(23):233305, 2008.

[35] K. S. Kim, Y. Zhao, H. Jang, S. Y. Lee, J. M. Kim, K. S. Kim, J.-H. Ahn, P. Kim, J.-Y. Choi, and B. H. Hong. Large-scale pattern growth of graphene films for stretchable transparent electrodes. *Nature*, 457(7230): 706–710, 2009.

[36] G. Eda, H. E. Unalan, N. Rupesinghe, G. A. J. Amaratunga, and M. Chhowalla. Field emission from graphene based composite thin films. *Applied Physics Letters*, 93(23):233502, 2008.

[37] K. S. Novoselov, D. Jiang, F. Schedin, T. J. Booth, V. V. Khotkevich, S. V. Morozov, and A. K. Geim. Two-dimensional atomic crystals. *Proceedings of the National Academy of Sciences*, 102(30):10451, 2005.

[38] S. Y. Park, H. C. Floresca, Y. J. Suh, and M. J. Kim. Electron microscopy analyses of natural and highly oriented pyrolytic graphites and the mechanically exfoliated graphenes produced from them. *Carbon*, 48 (3):797–804, 2010.

[39] X. Li, X. Wang, L. Zhang, S. Lee, and H. Dai. Chemically derived, ultrasmooth graphene nanoribbon semiconductors. *Science*, 319(5867): 1229–1232, 2008.

[40] X. Li, W. Cai, J. An, S. Kim, J. Nah, D. Yang, R. Piner, A. Velamakanni, I. Jung, E. Tutuc, S. K. Banerjee, L. Colombo, and R. S. Ruoff. Large-Area synthesis of High-Quality and uniform graphene films on copper foils. *Science*, 324(5932):1312–1314, 2009.

[41] A. K. Geim. Graphene: Status and prospects. *Science*, 324(5934):1530–1534, 2009.

[42] J. C. Meyer, A. K. Geim, M. I. Katsnelson, K. S. Novoselov, T. J. Booth, and S. Roth. The structure of suspended graphene sheets. *Nature*, 446 (7131):60–63, 2007.

[43] J. C. Meyer, C. O. Girit, M. F. Crommie, and A. Zettl. Hydrocarbon lithography on graphene membranes. *Applied Physics Letters*, 92(12): 123110, 2008.

[44] R. Renneberg and F. Lisdat, editors. *Biosensing for the 21st Century*, volume 109. Springer Berlin Heidelberg, Berlin, Heidelberg, 2008. ISBN 978-3-540-75200-4.

[45] H. Morgan and N. G. Green. *AC Electrokinetic: Colloids and Nanoparticles*. Research Studies Press Ltd, 1st edition, 2003. ISBN 0863802559.

[46] M. Dimaki and P. Bøggild. Frequency dependence of the structure and electrical behaviour of carbon nanotube networks assembled by dielectrophoresis. *Nanotechnology*, 16(6):759–763, 2005.

[47] S. B. Asokan, L. Jawerth, R. L. Carroll, R. E. Cheney, S. Washburn, and R. Superfine. Two-Dimensional manipulation and orientation of Actin-Myosin systems with dielectrophoresis. *Nano Letters*, 3(4):431–437, 2003.

[48] J. Voldman. Electrical forces for microscale cell manipulation. *Annu. Rev. Biomed. Eng.*, (8):425–54, 2006.

[49] J. Zaumseil and H. Sirringhaus. Electron and ambipolar transport in organic Field-Effect transistors. *Chemical Reviews*, 107(4):1296–1323, 2007.

[50] S. Z. Bisri, T. Takenobu, Y. Yomogida, H. Shimotani, T. Yamao, S. Hotta, and Y. Iwasa. High mobility and luminescent efficiency in organic Single-Crystal Light-Emitting transistors. *Advanced Functional Materials*, 19(11):1728–1735, 2009.

[51] T. Yamao, Y. Shimizu, K. Terasaki, and S. Hotta. Organic Light-Emitting Field-Effect transistors operated by Alternating-Current gate voltages. *Advanced Materials*, 20(21):4109–4112, 2008.

[52] J. Kjelstrup-Hansen, X. Liu, H. H. Henrichsen, K. Thilsing-Hansen, and H.-G. Rubahn. Conduction and electroluminescence from organic continuous and nanofiber thin films. *Physica status solidi*, 2010.

[53] C. Maibohm, J. R. Brewer, H. Sturm, F. Balzer, and H.-G. Rubahn. Bleaching and coating of organic nanofibers. *Journal of Applied Physics*, 100(5):054304, 2006.

[54] N. Koch, A. Pogantsch, E. J. W. List, G. Leising, R. I. R. Blyth, M. G. Ramsey, and F. P. Netzer. Low-onset organic blue light emitting devices obtained by better interface control. *Applied Physics Letters*, 74(20): 2909–2911, 1999.

[55] D. Vaufrey, M. B. Khalifa, J. Tardy, C. Ghica, M. G. Blanchin, C. Sandu, and J. A. Roger. ITO-on-top organic light-emitting devices: a correlated study of opto-electronic and structural characteristics. *Semiconductor Science and Technology*, 18(4):253–260, 2003.

[56] H. H. Henrichsen, J. Kjelstrup-Hansen, D. Engstrøm, C. H. Clausen, P. Bøggild, and H.-G. Rubahn. Electrical conductivity of organic single-nanofiber devices with different contact materials. *Organic Electronics*, 8(5):540–544, 2007.

[57] E. P. De Poortere, H. L. Stormer, L. M. Huang, S. J. Wind, S. O'Brien, M. Huang, and J. Hone. 1- to 2-nm-wide nanogaps fabricated with single-walled carbon nanotube shadow masks. *Journal of Vacuum Science & Technology B: Microelectronics and Nanometer Structures*, 24(6):3213, 2006.

[58] L. X. Zheng, M. J. O'Connell, S. K. Doorn, X. Z. Liao, Y. H. Zhao, E. A. Akhadov, M. A. Hoffbauer, B. J. Roop, Q. X. Jia, R. C. Dye, D. E. Peterson, S. M. Huang, J. Liu, and Y. T. Zhu. Ultralong single-wall carbon nanotubes. *Nat Mater*, 3(10):673–676, 2004.

[59] H. W. Zhu, C. L. Xu, D. H. Wu, B. Q. Wei, R. Vajtai, and P. M. Ajayan. Direct synthesis of long Single-Walled carbon nanotube strands. *Science*, 296(5569):884–886, 2002.

[60] Parallel bar grids - 400P mesh - SPI supplies. http://www.2spi.com/catalog/grids/parallel-bar-mesh_400p.php, 2010. The specifications indicate a hole width of 22 microns, however in grids used in the refering study holes were more like 33 microns.

[61] P. Bøggild, T. M. Hansen, C. Tanasa, and F. Grey. Fabrication and actuation of customized nanotweezers with a 25 nm gap. *Nanotechnology*, 12:331–335, 2001.

[62] A. S. Grove. *Physics and technology of semiconductor devices*. John Wiley & Sons, New York, 1967. ISBN 0-471-32999-1. 404 pp.

[63] N. Koch, E. Zojer, A. Rajagopal, J. Ghjisen, R. L. Johnson, G. Leising, and J.-J. Pireaux. Electronic properties of the interfaces between the wide bandgap organic semiconductor para-Sexiphenyl and samarium. *Advanced Functional Materials*, 11(1):51–58, 2001.

[64] N. Koch, A. Kahn, J. Ghijsen, J.-J. Pireaux, J. Schwartz, R. L. Johnson, and A. Elschner. Conjugated organic molecules on metal versus polymer electrodes: Demonstration of a key energy level alignment mechanism. *Applied Physics Letters*, 82(1):70, 2003.

[65] H. B. Michaelson. The work function of the elements and its periodicity. *Journal of Applied Physics*, 48(11):4729–4733, 1977.

[66] Y. Shen, A. R. Hosseini, M. H. Wong, and G. G. Malliaras. How to make ohmic contacts to organic semiconductors. *ChemPhysChem*, 5(1):16–25, 2004.

[67] H. H. Henrichsen, H. Sturm, P. Bøggild, and O. Hansen. Sub-micron organic nanofiber devices with different anode-cathode materials: a simple approach. *Journal of Vacuum Science & Technology B*, 2010.

[68] R. W. I. de Boer. Space charge limited transport and time of flight measurements in tetracene single crystals: A comparative study. *Journal of Applied Physics*, 95(3):1196, 2004.

[69] B. K. Crone, P. S. Davids, I. H. Campbell, and D. L. Smith. Device model investigation of single layer organic light emitting diodes. *Journal of Applied Physics*, 84:833, 1998.

[70] B. A. Gregg, S. E. Gledhill, and B. Scott. Can true space-charge-limited currents be observed in pi-conjugated polymers? *Journal of Applied Physics*, 99(11):116104, 2006.

[71] S. Tkaczyk, I. V. Kityk, J. Ebothé, and R. Viennois. The role of grain boundaries in the DC conductivity of p-sexiphenyl films. *Journal of Physics: Condensed Matter*, 16:2231–2244, 2004.

[72] F. Balzer, V. Bordo, A. Simonsen, and H.-G. Rubahn. Optical waveguiding in individual nanometer-scale organic fibers. *Physical Review B*, 67(11), 2003.

[73] J. H. Davies. *The physics of low-dimensional semiconductors*. Cambridge University Press, 1998. ISBN 052148491X, 9780521484916. 458 pp.

[74] D. J. Griffiths. *Introduction to quantum mechanics*. Prentice Hall, 1995. ISBN 0131244051, 9780131244054. 394 pp.

[75] V. Guidi, M.C. Carotta, C. Malagù, and G. Martinelli. Modeling of the inter-granular energy-barrier height in very-fine nanograins through a semi-classical approach. *Sensors and Actuators B: Chemical*, 137(2): 521–523, 2009.

[76] F. Balzer and H.-G. Rubahn. Growth of optically active p-phenylene needles on mica. *Surface Science*, 507(510):588–592, 2002.

[77] M. Era, T. Tsutsui, and S. Saito. Polarized electroluminescence from oriented p-sexiphenyl vacuum-deposited film. *Applied Physics Letters*, 67:2436, 1995.

[78] M. Klemenc, F. Meghdadi, S. Voss, and G. Leising. Electroluminescence in thin hexaphenyl-layers. *Synthetic Metals*, 85:1243–1244, 1997.

[79] F. Meghdadi, S. Tasch, B. Winkler, W. Fischer, F. Stelzer, and G. Leising. Blue electroluminescence devices based on parahexaphenyl. *Synthetic Metals*, 85:1441–1442, 1997.

[80] Y. Ohmori, T. Tsukagawa, and H. Kajii. Enhanced blue light electroluminescence utilizing heterostructure of p-sexiphenyl and TPD. *Displays*, 22(2):61–64, 2001.

[81] C. Winder, A. Andreev, H. Sitter, G. Matt, N. S. Sariciftci, and D. Meissner. Optoelectronic devices based on para-sexiphenyl films grown by hot wall epitaxy. *Synthetic Metals*, 139(3):573–576, 2003.

[82] J. George and C. S. Menon. Electrical and optical properties of electron beam evaporated ITO thin films. *Surface and Coatings Technology*, 132 (1):45–48, 2000.

[83] R. S. Alwitt. Electrochemistry encyclopedia – anodizing. http://electrochem.cwru.edu/encycl/art-a02-anodizing.htm.

[84] D. Hoffman and D. Leibowit. Effect of substrate potential on Al2O3 films prepared by electron-beam evaporation. *Journal of Vacuum Science & Technology*, 9(1):326, 1972.

[85] L. P. H. Jeurgens, W. G. Sloof, F. D. Tichelaar, and E. J. Mittemeijer. Growth kinetics and mechanisms of aluminum-oxide films formed by thermal oxidation of aluminum. *Journal of Applied Physics*, 92(3):1649, 2002.

[86] Y.-M. Lin, J. Appenzeller, J. Knoch, and P. Avouris. High-Performance carbon nanotube Field-Effect transistor with tunable polarities. *IEEE Transactions On Nanotechnology*, 4(5):481–489, 2005.

[87] P. M. Fishbane, S. Gasiorowicz, and S. T. Thornton. *Physics for scientists and engineers*. Prentice Hall, second edition edition, 1996. ISBN 0132311763, 9780132311762. 1280 pp.

[88] J. B. Hansen. Unpublished results disclosed in private conversations. 2008.

[89] C. R. Helms and B. E. Deal. Mechanisms of the HF/H20 vapor phase etching of si02. *Journal of Vacuum Science & Technology A*, 10(4):806, 1992.

[90] R. S. Alwitt and L. C. Archibal. Observations on hydrous oxide film on aluminum immersed in warm water. *Corrosion Science*, 13(9):687–688, 1973.

[91] C. C. Chang, D. B. Fraser, M. J. Grieco, T. T. Sheng, S. E. Haszko, R. E. Kerwin, R. B. Marcus, and A. K. Sinha. Aluminium oxidation in water. *Journal of the Electrochemical Society*, 125(5):787–792, 1978.

[92] C. M. Aguirre, C. Ternon, M. Paillet, P. Desjardins, and R. Martel. Carbon nanotubes as injection electrodes for organic thin film transistors. *Nano Letters*, 9(4):1457–1461, 2009.

[93] J. Appenzeller, M. Radosavljevic, J. Knoch, and P. Avouris. Tunneling versus thermionic emission in One-Dimensional semiconductors. *Physical Review Letters*, 92(4), 2004.

[94] S. Wang, J. Wang, P. Miraldo, M. Zhu, R. Outlaw, K. Hou, X. Zhao, B. C. Holloway, D. Manos, T. Tyler, O. Shenderova, M. Ray, J. Dalton, and G. McGuire. High field emission reproducibility and stability of carbon nanosheets and nanosheet-based backgated triode emission devices. *Applied Physics Letters*, 89(18):183103, 2006.

[95] T. Takahashi, H. Tokailin, and T. Sagawa. Angle-resolved ultraviolet photoelectron spectroscopy of the unoccupied band structure of graphite. *Physical Review B*, 32(12):8317–8324, 1985.

[96] H. Hibino, H. Kageshima, M. Kotsugi, F. Maeda, F.-Z. Guo, and Y. Watanabe. Dependence of electronic properties of epitaxial few-layer graphene on the number of layers investigated by photoelectron emission microscopy. *Physical Review B*, 79(12), 2009.

[97] Z. Rácz and A. Seabaugh. Characterization and control of unconfined lateral diffusion under stencil masks. *Journal of Vacuum Science & Technology B: Microelectronics and Nanometer Structures*, 25(3):857, 2007.

[98] S. T. Lee, Z. Q. Gao, and L. S. Hung. Metal diffusion from electrodes in organic light-emitting diodes. *Applied Physics Letters*, 75:1404, 1999.

[99] 1620-2008 IEEE standard for test methods for the characterization of organic transistors and materials, December 2008.

[100] C. R. Viswanathan. Plasma-induced damage. *Microelectronic Engineering*, 49(1-2):65–81, 1999.

[101] M. Egginger, S. Bauer, R. Schwödiauer, H. Neugebauer, and N. S. Sariciftci. Current versus gate voltage hysteresis in organic field effect transistors. *Monatshefte für Chemie - Chemical Monthly*, 140(7):735–750, 2009.

[102] J. Appenzeller, J. Knoch, V. Derycke, R. Martel, S. Wind, and Ph. Avouris. Field-Modulated carrier transport in carbon nanotube transistors. *Physical Review Letters*, 89(12), 2002.

[103] C. Santato, R. Capelli, M. A. Loi, M. Murgia, F. Cicoira, V. A. L. Roy, P. Stallinga, R. Zamboni, C. Rost, S. F. Karg, et al. Tetracene-based organic light-emitting transistors: optoelectronic properties and electron injection mechanism. *Synthetic Metals*, 146(3):329–334, 2004.

[104] L.-L. Chua, J. Zaumseil, J.-F. Chang, E. C.-W. Ou, P. K.-H. Ho, H. Sirringhaus, and R. H. Friend. General observation of n-type field-effect behaviour in organic semiconductors. *Nature*, 434(7030):194–199, 2005.

[105] G. Gu, M. G. Kane, J. E. Doty, and A. H. Firester. Electron traps and hysteresis in pentacene-based organic thin-film transistors. *Applied Physics Letters*, 87(24):243512, 2005.

[106] C. Petit, D. Zander, K. Lmimouni, M. Ternisien, D. Tondelier, S. Lenfant, and D. Vuillaume. Gate pulse electrical method to characterize hysteresis phenomena in organic field effect transistor. *Organic Electronics*, 9(6): 979–984, 2008.

[107] P. V. Necliudov, M. S. Shur, D. J. Gundlach, and T. N. Jackson. Modeling of organic thin film transistors of different designs. *Journal of applied Physics*, 88:6594, 2000.

[108] Y. Cao, S. Liu, Q. Shen, K. Yan, P. Li, J. Xu, D. Yu, M. L. Steigerwald, C. Nuckolls, Z. Liu, and X. Guo. High-Performance photoresponsive organic nanotransistors with Single-Layer graphenes as Two-Dimensional electrodes. *Advanced Functional Materials*, 19(17):2743–2748, 2009.

[109] U. Bernchou, J. Brewer, H. S. Midtiby, J. H. Ipsen, L. A. Bagatolli, and A. C. Simonsen. Texture of lipid bilayer domains. *J. Am. Chem. Soc*, 131(40):14130–14131, 2009.

[110] J. D. Bernal. The structure og graphite. *Proceedings of the royal society of London series A*, 106(740):749–773, 1924.

[111] L. Kankate, F. Balzer, H. Niehus, and H.-G. Rubahn. From clusters to fibers: Parameters for discontinuous para-hexaphenylene thin film growth. *The Journal of Chemical Physics*, 128(8):084709, 2008.

[112] Z. Wang, K. Kanai, K. Iketaki, Y. Ouchi, and K. Seki. Epitaxial growth of p-sexiphenyl film on highly oriented pyrolytic graphite surface studied by scanning tunneling microscopy. *Thin Solid Films*, 516(9):2711–2715, 2008.

[113] G. Koller, S. Berkebile, J. R. Krenn, G. Tzvetkov, G. Hlawacek, O. Lengyel, F. P. Netzer, C. Teichert, R. Resel, and M. G. Ramsey. Oriented sexiphenyl single crystal nanoneedles on TiO2 (110). *Advanced Materials*, 16(23-24):2159–2162, 2004.

[114] T. Haber, R. Resel, A. Andreev, M. Oehzelt, D.-M. Smilgies, and H. Sitter. Evolution of epitaxial order in para-sexiphenyl on KCl(100). *Journal of Crystal Growth*, 312(2):333–339, 2010.

[115] R. Krupke, F. Hennrich, H. B. Weber, M. M. Kappes, and H. v. Löhneysen. Simultaneous deposition of metallic bundles of single-walled carbon nanotubes using ac-dielectrophoresis. *Nano Letters*, 3(8):1019–1023, 2003.

[116] A. Vijayaraghavan, S. Blatt, D. Weissenberger, M. Oron-Carl, F. Hennrich, D. Gerthsen, H. Hahn, and R. Krupke. Ultra-Large-Scale directed assembly of Single-Walled carbon nanotube devices. *Nano Letters*, 7(6): 1556–1560, 2007.

[117] E. J. Meijer, D. M. de Leeuw, S. Setayesh, E. van Veenendaal, B. - H. Huisman, P. W. M. Blom, J. C. Hummelen, U. Scherf, and T. M. Klapwijk. Solution-processed ambipolar organic field-effect transistors and inverters. *Nat Mater*, 2(10):678–682, 2003.

[118] H. Hasegawa and H. L. Hartnagel. Anodic oxidation of GaAs in mixed solutions of glycol and water. *Journal of the Electrochemical Society*, 123 (5):713–723, 1976.

[119] AZ electronic materials. http://www.az-em.com/index.html.

Back cover image captions:

First image: Polarized optical microscope image of a graphite flake with out-of-plane facets, upon which an approximately 50 nm *para*-hexaphenylene thin film was deposited. Crystalline domains cause a pronounced polarization of the reflected light.

Second image: 1 keV SE2 scanning electron microscope zoom-in on the first image. Crystalline nanofiber-like aggregates have formed on the surface with characteristic alignment to the graphite lattice.

Third image: 200 keV transmission electron microscope image of organic *para*-hexaphenylene nanofibers transferred to an electron transparent support. Somehow arrays of nanofibers have aligned perpendicular to each other during the wet transfer. (Acquired with help from Timothy John Booth).

Fourth image: 1 keV SE2 scanning electron microscope image of suspended graphene, upon which a 10 nm thin film of *para*-hexaphenylene was deposited at approximately 80°C. Nanofiber-like aggregates have formed on the graphene flake only.

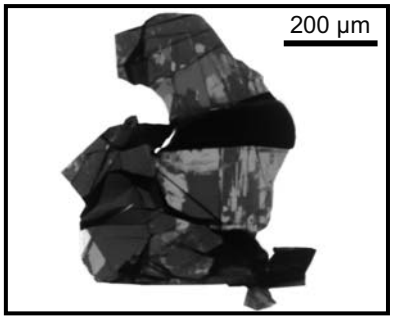

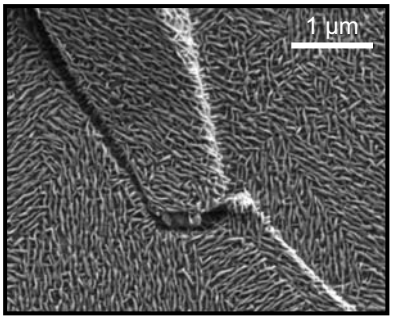

What is it all good for? Researchers sometime question their work that way, in situations where purpose and reason seem to have been left behind. But sometimes prejudiced purpose may steer you away from discoveries that later find uses impossible to predict. Therefore, when nature discloses peculiar phenomena not already described, the mere fact that it is new will in most cases be enough reason to investigate and properly describe the discovery to the scientific community. In other words, allow the things you observe to decide some of the sidetracks you follow, instead of only focusing on the purpose you had in mind from the start. Who are you alone to decide what the right purpose is anyway?

This thesis describes ways to establish electrical contact to crystalline organic nanofibers including an investigation of their electrical properties. The exciting properties of graphene as electrode material have been tested in an organic field effect transistor structure and for di-electrophoresis. And a peculiar discovery led to the investigation of crystalline organic nanofiber growth on graphitic substrates.